A Measurement of the Photon Structure Function $F_2(x)$

Mark H. Lehto

University College London

Submitted for the degree of

Doctor of Philosophy

September, 1993

To my mother,

Joan

and in memory of a dear father,

Rick.

Abstract

Measurements of the hadronic photon structure function $F_2(x)$ are presented in two Q^2 ranges (mean values 5.9 GeV^2 and 14.7 GeV^2). The results confirm that there is a significant pointlike component of the photon when the probe photon has $Q^2 > 4$ GeV^2. The measurements extend to lower values of x than any previous experiment, and no increase of $F_2(x)$ is observed in this region. In the context of a perturbative QCD + vector meson dominance (VMD) model the quark transverse momentum cutoff separating the VMD and perturbative QCD regions is found to be 0.44 ± 0.12 GeV. The data prefers a VMD component which has only peripheral scattering of the quarks in the $\gamma\gamma$ centre of mass.

The data were taken by the OPAL experiment at LEP, with $\sqrt{s}$ close to the Z^0 mass and correspond to an integrated e^+e^- luminosity of 18.43 pb^{-1}. The analysis is based on 596 events which pass the final selection cuts.

Acknowledgements

Firstly I would like to thank my supervisor, Professor David Miller, for getting me to this stage. He has been very enthusiastic on the physics front and understanding when I had problems at home.

I would like to acknowledge the hard work put in by all the OPALites, current and previous, without whom this thesis would not have been possible. Between them they have created a very reliable detector and they are, in general, very understanding when a poor graduate student tries to screw things up.

Some people have had to be more understanding than others. I would particularly like to thank Bruce Kennedy, Adriaan Buijs and Al Lee for answering many silly questions on the idiosyncracies of such computer-lovelies as FORTRAN, PATCHY, MAW and PAW among others.

Other people have had the task of trying to keep me on an even keel during this thesis. Strangely enough this often involved trying get me to fall over, either under the influence of the demon drink (Jim), by totally excessive over feeding (Jim again) or by leaving me 3000 meters up a mountain attached to a pair of skies (guess who?). Luckily there were some saner people around to carry me home again afterwards (Ronan and Steve... the men with the BMWs). Bob should fit in there somewhere (though noone knows exactly where). Many others should also be mentioned but the binder calls...

Back in England the support task was undertaken by a different group of equally dedicated people who did their best without the help of mountainous terrain. Douglas, Paul, Peter, Alun and Sue please take a bow. My family too must take its share of the credit so thanks to Joan, Clare and Lisa. There were many others who did not survive my cooking. Paul Makkar should be remembered for asking lots of stupid questions that I could not answer and for keeping the minstrel man under control.

Finally I would like to thank SERC and UCL for funding me throughout my PhD, and in particular Mary Shewry and Sue Cannon for being very helpful in a difficult time.

Contents

List of Figures

List of Tables

Chapter 1

Introduction

The photon has a rich structure which is still poorly explored. Phenomenologically photon-hadron interactions bear remarkable similarities to hadron-hadron ones [1]. This can be explained if the physical photon is a superposition of a bare photon $|\gamma_B\rangle$ and a hadronic component $|h\rangle$ [2],

$$|\gamma\rangle = \sqrt{Z_3}|\gamma_B\rangle + c\sqrt{\alpha}|h\rangle, \tag{1.1}$$

where c is of $O(1)$, $\alpha \simeq 1/137$ and $Z_3^2 = 1 - c^2\alpha$. The structure of this hadronic component can also be studied in photon-photon interactions.

Experimentally two photon collisions are achieved by using the virtual photon clouds surrounding the electron and positron in e^+e^- machines as shown in figure 1.1. The incoming electron and positron with energy E_{BEAM} each radiate a photon and these interact to produce a final state of invariant mass W.

This final state can consist of leptons, which involves a pure Quantum Electrodynamic (QED) process, or hadrons, which can be modelled by the Quark Parton Model (QPM), Quantum Chromodynamics (QCD) or the Vector Meson Dominance (VMD) model (among others). There are a variety of interesting physics analyses that can be carried out on two photon events:-

- Meson spectroscopy. The final state is in a charge conjugation C= +1 eigenstate, as opposed to annihilation events where the final state is in a

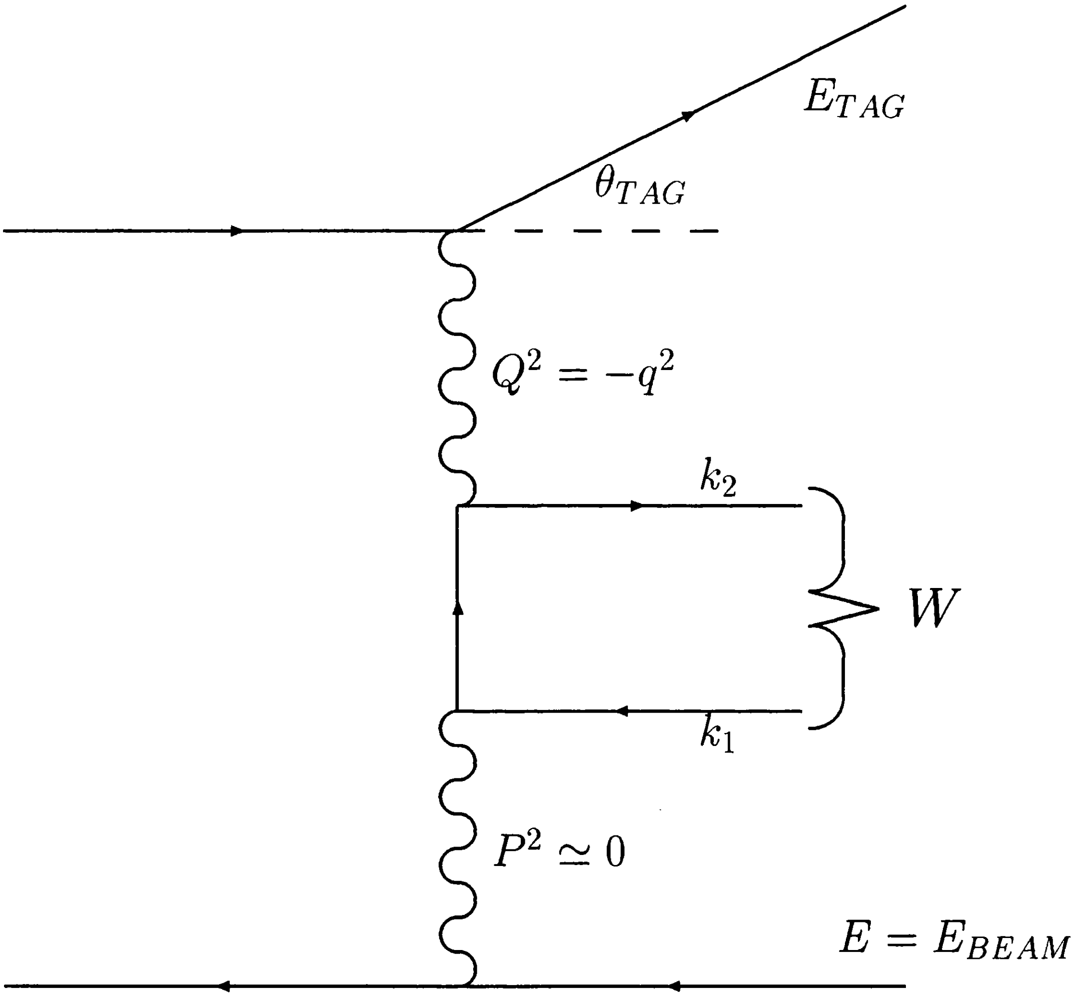

Figure 1.1: Single tagging two photon diagram. This can be regarded as deep inelastic scattering which probes the structure of the quasi-real ($P^2 \simeq 0$) photon.

C= -1 eigenstate, which means different meson states can be accessed. If a state has an unexpectedly high or low production cross section in $\gamma\gamma$ reactions then this could be an indication of an exotic component to that state.

- QED can be tested to $O(\alpha^4)$ in reaction of the type $\gamma\gamma \rightarrow l^+l^-$ where $l = e, \mu, \tau$.

- The gluon content of the photon can be probed in resolved photon processes. The background to annihilation events from such resolved processes at future e^+e^- machines has been predicted [3] to be serious. An attempt to measure the rate at current e^+e^- colliders would be a useful indicator towards possible future problems.

- The hadronic structure function $F_2(x, Q^2)$ of the photon can be measured. This tests a number of predictions of QCD.

This thesis describes the measurement of the hadronic photon structure function $F_2(x, Q^2)$ using data from the OPAL [4] detector at LEP, the Large Electron Positron collider at CERN, Geneva[62].

1.1 The Photon Structure Function

The two-photon process $e^+e^- \rightarrow e^+e^- + hadrons$ has been extensively studied [5, 6, 7, 8, 9, 10, 11, 12, 13] in the kinematic region where one of the electrons, known as the tag, is detected in the Q^2 range $0.1 < Q^2 < 500$ GeV^2 whilst the other is restricted to small angles and not observed. This is known as single tagging (double tagging is where both final state electrons are detected). In the single tagging kinematic region the reaction can be interpreted as deep inelastic scattering, with one highly virtual photon ($Q^2 \gg 0$) probing one nearly real one($P^2 \simeq 0$) (see fig. 1.1). The cross section can then be expressed in terms of the structure functions $F_1(x, Q^2)$ and $F_2(x, Q^2)$ of the quasi real or target photon as [14]:

$$\frac{d\sigma}{dxdy} = \frac{4\pi\alpha^2 s(e\gamma)}{Q^4}[(1-y)\mathrm{F}_2(x,Q^2) + xy^2\mathrm{F}_1(x,Q^2)] \tag{1.2}$$

with

$$\begin{aligned} Q^2 &= 2EE_{TAG}(1-\cos\theta_{TAG}), && (1.3)\\ x &= \frac{Q^2}{Q^2+W^2}, && (1.4)\\ y &= 1-\frac{E_{TAG}}{E}\cos^2(\frac{\theta_{TAG}}{2}) && (1.5) \end{aligned}$$

where the kinematic variables are defined with reference to Figure 1.1. $s(e\gamma)$ is the centre of mass energy of the electron-quasi real photon system, E_{BEAM} is the beam energy, E_{TAG} is the energy of the tagged $e^{\pm}$ and θ_{TAG} is the angle of the tagged $e^{\pm}$ to the beam direction. Experimentally it is usual to demand a high tag energy, and events are strongly peaked towards the beam direction, which means that y is normally small (see equation 1.5) and $y^2 \ll (1-y)$. Equation 3.2 shows that $\mathrm{F}_2(x,Q^2) > x\mathrm{F}_1(x,Q^2)$ so that

$$(1-y)\mathrm{F}_2(x,Q^2) \gg xy^2\mathrm{F}_1(x,Q^2)$$

and the analysis is normally done solely in terms of $\mathrm{F}_2(x,Q^2)$:

$$\frac{d\sigma}{dxdy} = \frac{4\pi\alpha^2 s(e\gamma)}{Q^4}(1-y)\mathrm{F}_2(x,Q^2).$$

1.2 Simple Theory

The photon structure function, $\mathrm{F}_2(x,Q^2)$, can be interpreted as the momentum weighted sum of the quark distributions $q(x,Q^2)$ within the photon,

$$\mathrm{F}_2(x,Q^2) = x\sum_i e_i^2\left[q_i(x,Q^2)+\overline{q}_i(x,Q^2)\right], \tag{1.6}$$

where $q_i(x,Q^2)$ is the probability to find a quark of type i, charge e_i and momentum fraction x within the target photon, when probed by a virtual photon with $Q^2 = -q^2$.

In 1977 Witten [15] proposed that $\mathrm{F}_2(x,Q^2)$ could be split into two parts, a pointlike part and a part where the photon behaves as if it were actually a hadron,

$$\mathrm{F}_2(x,Q^2) = \mathrm{F}_2^{PL}(x,Q^2) + \mathrm{F}_2^{HAD}(x,Q^2). \tag{1.7}$$

The pointlike part, $\mathrm{F}_2^{PL}(x,Q^2)$, is calculable in QCD and $\mathrm{F}_2^{HAD}(x,Q^2)$ is normally estimated using the Vector Meson Dominance (VMD) model, where the photon is represented as a sum of the lowest mass vector meson states, the ρ, ω and ϕ. This corresponds to the separation of the hadronic component of the photon $|h\rangle$, introduced in equation 1.1, into a phenomenological part described by the VMD model $|V\rangle$ (represented in figure 1.2(a)) and a QCD calculable $|q\bar{q}\rangle$ part (represented in figure 1.2(b)),

$$|\gamma\rangle = \sqrt{Z_3}|\gamma_B\rangle + \sum_{V=\rho^0,\omega,\phi} \frac{e}{f_V}|V\rangle + \frac{e}{f_{q\bar{q}}}|q\bar{q}\rangle. \tag{1.8}$$

$\frac{e}{f_V}$ is the probability for a photon to fluctuate into a vector meson [16], and $\frac{e}{f_{q\bar{q}}}$ is the probability to fluctuate into a $q\bar{q}$ pair (which then interact according to perturbative QCD).

By virtue of the superposition made in 1.8 we are led to distinguish two different types of singly tagged $\gamma\gamma$ events,

- the target photon fluctuates into a vector meson as shown in figure 1.2. The high Q^2 photon therefore finds momentum distributions consistent with quarks inside a vector meson. Phenomenologically these events will have a low p_T with respect to the incoming photons in the $\gamma\gamma$ center of mass system.

- the target photon fluctuates into a virtual $q\bar{q}$ pair. This is responsible for the events which have a higher p_T of the final state quarks and which has been variously described as pointlike [15] or anomalous [17]. The momentum distribution probed by the high Q^2 photon is calculable in perturbative QCD.

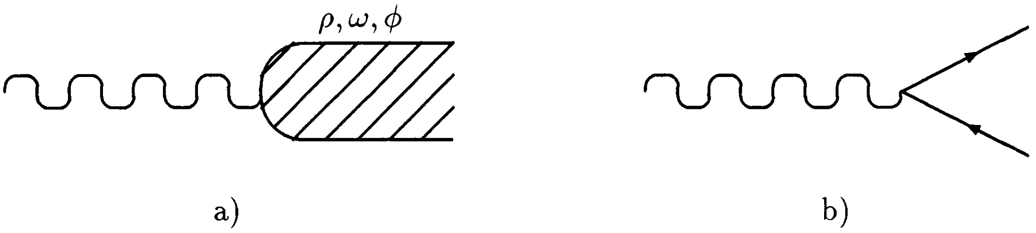

Figure 1.2: Photon coupling to quarks. a) VMD hadronic coupling. b) Pointlike photon quark coupling.

The pointlike part of $F_2(x, Q^2)$, which is calculable in QCD, exhibits logarithmic scale breaking and is sensitive to the QCD scale parameter $\Lambda_{\overline{MS}}$ [15],

$$F_2^{PL}(x, Q^2) = h(x) \ln \left(\frac{Q^2}{\Lambda^2_{\overline{MS}}} \right) + \text{higher order in } \alpha_s. \tag{1.9}$$

Equations 1.7 and 1.9 incorporate some remarkable predictions:

i) The structure function $F_2(x, Q^2)$ grows like $\ln Q^2$ for large Q^2.

ii) If there were to be a regime where only the pointlike part mattered, then a direct measurement of $\Lambda_{\overline{MS}}$ could be made.

The logarithmic scale breaking of $F_2(x, Q^2)$ has been confirmed over the range $4 < Q^2 < 500$ GeV^{2}by [8, 9, 10, 11, 12, 13] and in the past measurements of $\Lambda_{\overline{MS}}$ have been presented by [5, 8, 9, 10, 11]. The validity of these measurements has been plagued with theoretical uncertainties [18, 19, 20, 21]. It is now thought that uncertainties in the pointlike/hadronic separation and higher order QCD corrections have "washed out" much, if not all, of the sensitivity to $\Lambda_{\overline{MS}}$ at the currently experimentally available Q^2 [22].

The separation in the behaviour of the photon has been confirmed by results from experiments operating at low Q^2 (< 1.5 GeV^2) and at higher Q^2 (> 4 GeV^2). The logarithmic scale breaking discussed above confirms a significant pointlike component at high Q^2. The TPC/2γ experiment [5] demonstrated that at low

Q^2 (< 1.5 GeV^2) the data was well described by the Vector Meson Dominance (VMD) model, where the structure function $F_2(x)$ is similar to the pion structure function as measured in Drell Yan processes [23]. The ρ structure function is assumed to be similar to that of the pion as they both have two quarks in an s-wave state.

The structure of the photon is discussed further in chapter 3.

1.3 Muonic $F_2(x, Q^2)$

The pure QED process $e^+e^- \rightarrow e^+e^- + \mu^+\mu^-$ has been studied in OPAL in the single and double tag case (see [24] for details). The measured $F_2(x, Q^2)$ from OPAL, CELLO, and PEP-9 data, and the QED predictions for $F_2(x, Q^2)$ are shown in figure 1.3. The OPAL data agrees well with the theoretical prediction and the CELLO [25] data at a similar Q^2. The PEP-9 data is at a lower Q^2 and the scaling of the structure function can clearly be seen. Since we can accurately reproduce the muonic structure of the photon then we have confidence that the tag variables (which define Q^2) in particular are well understood. Assuming the factorization of figure 1.1 (see section 3.1) this means we can have confidence in our Q^2 measurement. Our confidence in the measurement of W has to come from the agreement of Monte Carlo and data (section 6.2).

1.4 Outline

The data used in this analysis were taken in 1990 and 1991 and amount to 18.43pb^{-1} integrated luminosity. The final data sample consists of approximately 600 events in the Q^2 regime where pointlike scattering, as calculated by perturbative QCD, is expected to be the major component.

An outline of the OPAL detector follows in Chapter 2, the theory involved is further discussed in Chapter 3, Chapter 4 describes details of the data selection,

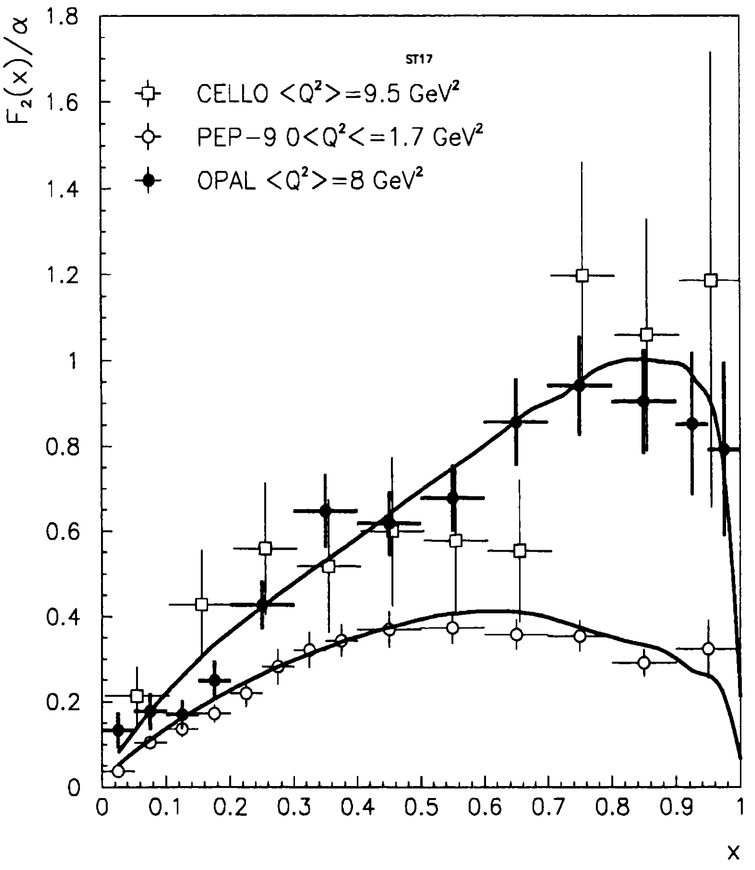

Figure 1.3: A comparison of Muonic $F_2(x, Q^2)$ from OPAL data and theory. The lines are the expectations for the PEP-9 data and for the OPAL data. The expectation for the CELLO data lies very close to that for the OPAL data.

the Monte Carlos used are discussed in Chapter 5, and Chapters 6 and 7 compare Monte Carlo and data and extract the unfolded $F_2(x, Q^2)$.

Chapter 2

The OPAL Detector

The data analysed in this thesis are taken from the OPAL [4] detector, one of four large detectors built around the e^+e^- storage ring LEP at CERN. It is a multipurpose apparatus designed to have an acceptance for Z^0 decays of nearly 4π steradians, with accurate and unambiguous event reconstruction. The main elements of the detector are:

- Tracking of charged particles in the central region of a solenoidal coil which gives measurements of their direction and momentum, as well as some particle identification using dE/dx. Vertices are also reconstructed.

- Electromagnetic calorimetry measuring primarily the energy and direction of photons and electrons.

- Hadronic calorimetry measuring the hadronic energy by total absorption in the instrumented magnetic return yoke.

- Muon Chambers measuring the position of particles which have passed through the hadron calorimeter (mostly muons).

- Forward Detectors measuring the absolute machine luminosity using Bhabha scattering events in the forward direction with respect to the beam line. These also measure the energy and angle of the tagged electrons for the events used in this analysis.

Two pictures of the detector are shown in figures 2.1 and 2.2 which indicate the location and relative size of the various components. A system of tracking chambers is contained within a solenoid which provides a uniform magnetic field of 0.435 T. This is surrounded with a time of flight counter array, a lead glass electromagnetic calorimeter with a presampler, an instrumented iron return yoke (hadron calorimeter) and four layers of outer muon chambers.

2.1 Central Tracking

There are four subdetectors used in the central tracking region namely a silicon microvertex detector (μv), a vertex detector (CV), a large volume jet chamber (CJ), and z-chambers (CZ). The main tracking is performed with the jet chamber, with the two vertex detectors providing better vertex information and the z-chambers improving the z-resolution. The gas (88.2% argon, 9.8% methane, 2.0% isobutane) used in the central tracking detectors is common to CJ,CV and CZ and is under a pressure of 4 bar.

Silicon Microvertex

This detector was added to OPAL in the winter shutdown of 1991, in order to improve the vertex resolution. Space was made for it by installing a new double beam pipe, with the detector lying between the two pipes. It has two layers of silicon ladders with an intrinsic resolution of 5 μm in r-ϕ. In the 1992 shutdown the ladders were replaced with double sided silicon to give z information. It is not used in this analysis.

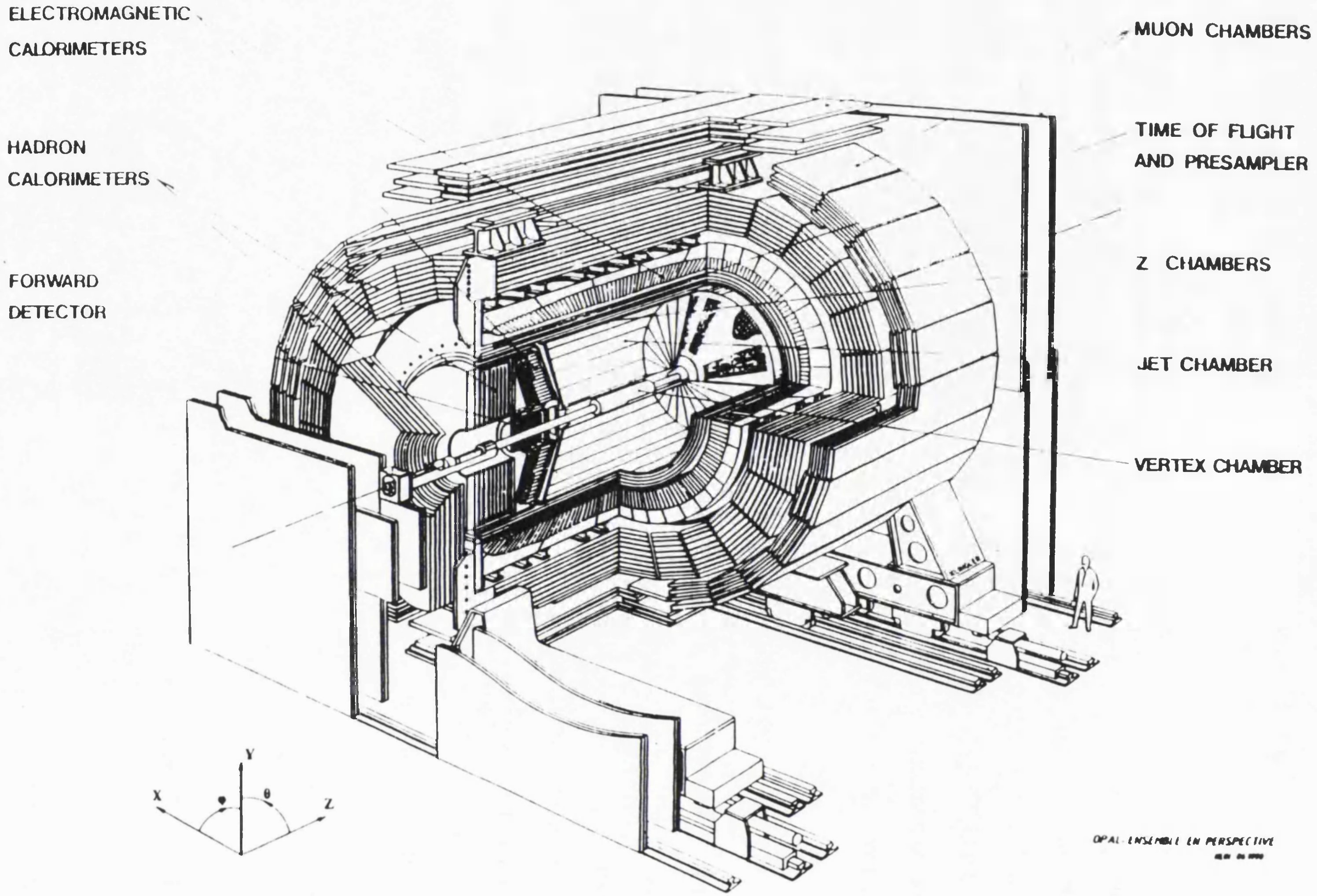

Figure 2.1: General layout of the OPAL detector.

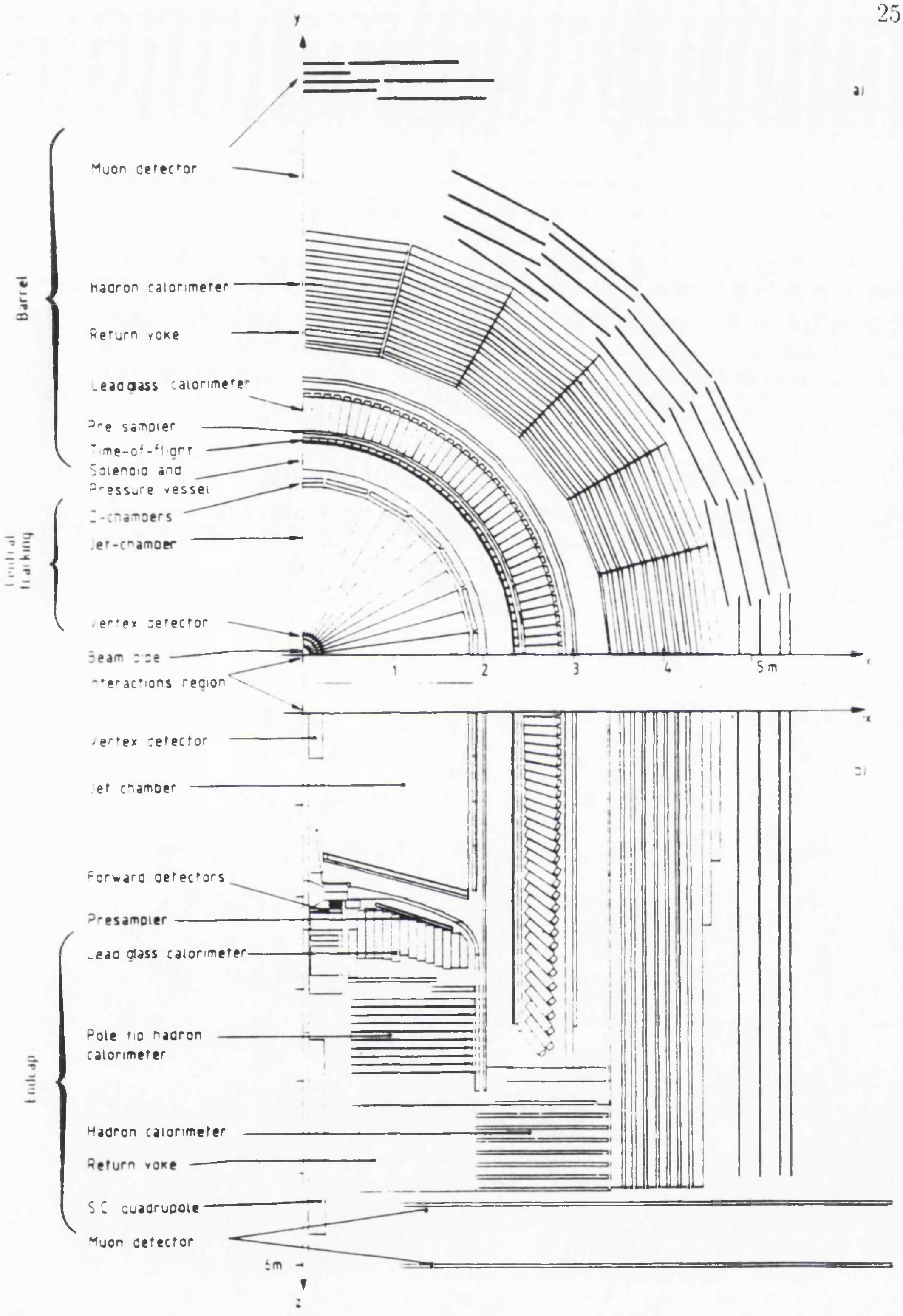

Figure 2.2: Cross section of a quadrant of the detector (a) perpendicular and (b) parallel to the LEP beam axis

Vertex Detector

The vertex detector, located between the outer beam pipe and the jet chamber, is used to locate the decay vertices of short lived particles and to improve momentum resolution. It is based on a scaled down jet chamber design, being 1 meter long and 470 mm in diameter, and has an inner layer of 36 cells with axial wires and an outer layer of 36 cells of small angle (4 deg) stereo wires. Each axial cell contains 12 anode wires with a radial spacing of 5.3 mm and the stereo cells have 6 anode wires with a 5 mm spacing. These anode wires are staggered by ±41 μm to resolve left right ambiguities.

Jet Chamber

The jet chamber was designed to combine good space and track resolution with the possibility of particle identification. The sensitive volume is a cylinder with length about 4 m, inner diameter 0.5 m and outer 3.7 m. The chamber is divided in ϕ into 24 identical sectors, each containing 159 sense wires all of which are parallel to the beam direction. In the range $43 < \theta < 137$ deg 159 points are measured along each track. Particle identification is done by multiple sampling of the energy loss in the gas. The average resolution in $r - \phi$ is 135 μm, and the average z resolution is 6 cm. The resolution can be parameterized by $\sigma_p/p^2 = 2.2 * 10^{-3}$ GeV^{-1}.

Z-Chambers

The Z- chambers (CZ) are arranged to form a barrel layer around the jet chamber covering $44 < \theta < 136$ deg. They are designed to improve the measurement of the z-coordinate of charged particles and thus improve the polar angle and invariant mass resolutions. They consist of 24 drift chambers, 4 m long, 50 cm wide and 59 mm deep. Each chamber is divided into 8 cells so the max drift distance is 25 cm in z. Each cell has 6 anode wires with 4mm spacing and a ± 250 μm to resolve the left right ambiguity. The z resolution is around 300 μm and the $r-\phi$ resolution (from charge division) is of order 1.5 cm.

Combined Performance

In the $r-\phi$ plane the r.m.s resolution is found to be 75 μm and in the $r-z$ plane it is 2 mm with and 2.7 cm without the stereo wire information from the vertex detector. The invariant mass resolution for $K^0 \rightarrow \pi^+\pi^-$ decays is 8 MeV.

2.2 Time-of-Flight

The time of flight (TOF) system covers $\cos\theta < 0.82$. It generates triggers, helps in particle identification and aids in the rejection of cosmic rays. This system consists of 160 scintillation counters, 6.84 m long with a trapezoidal cross section, forming a barrel of mean radius 2.36 m.

2.3 Electromagnetic Calorimetry

The main electromagnetic calorimetry in OPAL uses three assemblies of lead glass blocks, the barrel surrounding the solenoid, and two endcaps. These cover 98% of the solid angle and together with the gamma catcher and forward calorimeter (see section 2.6) mean that OPAL is hermetic down to the inner edge of the forward calorimeter. Lead glass was chosen for its excellent energy resolution ($\sigma_E/E \sim 5\%/\sqrt{E}$ where E is the electromagnetic energy in GeV) and linearity. It provides some π°-photon discrimination and, in conjunction with the central tracking system, electron-hadron discrimination. Since there are $\sim$2 $X_\circ$ of material in front of the lead glass, due mostly to the coil and pressure vessel, most electromagnetic showers are initiated before the lead glass itself. Presampling devices are therefore installed in both the barrel and endcap regions immediately in front of the lead glass, to measure the position and sample the energy of these electromagnetic showers, thereby improving the π°-photon and electron-hadron discrimination and the electromagnetic energy resolution.

Barrel Electromagnetic Presampler

In the barrel region the presampler consists of a cylinder of tubes, 6623 mm in length, operated in the limited streamer mode. These are located between the time-of-flight system and the barrel lead glass calorimeter at a radius of 2388 mm.

There are 16 chambers each of which has two layers of limited streamer mode tubes. The cells of the chambers are formed from PVC extrusions with 24 cells per extrusion. The cells have an internal size of 9.6 mm square, with 1 mm thick walls. Each of the two layers are made of four extrusions and the layers are offset by half a cell width at the centre of the sectors to avoid inefficiencies associated with the cell walls.

Readout is obtained from 1 cm wide cathode strips located on both sides of each layer of tubes, and oriented at 45° to the wire. The wires are read out at both ends to provide a z position.

The resolution for the position of electromagnetic showers, in the plane perpendicular to the shower direction, varies from about 6 to 4 mm as the energy changes from 6 to 50 GeV. This corresponds to an angular resolution for photon trajectories of $\sim$2 mrad. The resolution in z from current division is $\sim$10 cm for a single charged particle.

Barrel Lead Glass Calorimeter

The barrel lead glass calorimeter (EB), consists of a cylindrical array of 9,440 lead glass blocks of 24.6 $X_{\circ}$, located at a radius of 2455 mm, outside the magnet coil, covering the full azimuthal angle and $|\cos\theta|<0.82$. The longitudinal axes of the blocks are arranged such that each block points not at, but near to ($\sim$30 mm) the interaction point.

The blocks are made of heavy glass, SF57, and are instrumented with shielded phototubes stable to 1% in external fields of up to 100 G. Each lead glass block is $\sim 10 \times \sim 10$ cm^2 in cross section and 37 cm in depth. For optical isolation it is wrapped in a black sheet of vinyl fluoride the inner surface of which is coated with aluminium for efficient light reflection.

The typical energy resolution is $\sigma_E/E = 0.2\% + 6.3\%/\sqrt{E}$.

Endcap Electromagnetic Presampler

The endcap presampler (PE) is an umbrella type arrangement of thin multiwire chambers operating in a high gain mode. These are suited for the necessity of providing good position and energy resolution whilst being small enough to fit in the limited space available.

There are 32 chambers in 16 wedges located between the pressure bell of the central tracking system and the endcap electromagnetic calorimeter, covering the full azimuthal angle and $0.83<|\cos\theta|<0.95$. Each sector has one large and one small trapezoidal chamber, the large one being inclined by 18° with respect to the plane perpendicular to the beam in order to follow the shape of the pressure bell and the lead glass. The small chamber is at 90° to the beam axis. Neighbouring sectors overlap each other to ensure complete coverage of the endcap region.

The endcap presampler has an angular resolution, $\sigma_{PE} \sim 4.6$ mrad.

Endcap Electromagnetic Calorimeter

The endcap electromagnetic calorimeter (EE) consists of two dome-shaped arrays, each of 1,132 lead glass blocks, located immediately beyond the pressure bell of the central detector vessel. It covers the full azimuthal angle and $0.81<|\cos\theta|<0.98$. It differs from the barrel lead glass calorimeter in two important aspects: the lead glass blocks are mounted with their axes coaxial with the beam line, because of tight geometrical constraints, and it is instrumented with novel devices, single stage multipliers known as vacuum photo triodes (VPTs), which were developed in conjunction with industry to be able to operate in the full axial field of the magnet. The lead glass used is CEREN-25. The surfaces of the blocks are polished, and each block is housed in a brass can which acts as an electrical screen. For efficient reflection of light, each block is wrapped with aluminium foil, at ground potential, and is enclosed in a protective layer of mylar. The detector follows the curve of the pressure bell, and thus the blocks come in three lengths which give typically 22 X_o.

The spatial resolution was found to be 8–14 mm for a 6 GeV e^- beam incident at 15° to the longitudinal block axes, and the energy resolution (measured using Bhabhas) is $\sigma_E/E = 3.5\%$.

2.4 Hadron Calorimeter

The hadron calorimeter measures the energy of hadrons emerging from the electromagnetic calorimeter and assists in the identification of muons. The iron of the return yoke provides 4 or more interaction lengths of absorber over a solid angle of 97% of 4π. The yoke is segmented into layers, with planes of detectors between each layer, and forms a cylindrical sampling calorimeter about 1 metre thick. The energy resolution is limited mostly by the material of the electromagnetic calorimeter, and by the structure of the return yoke itself. It is not used in this analysis.

2.5 Muon Detector

The muon detector is constructed as a barrel and two endcaps and covers the iron yoke almost completely. Most muons penetrate to the muon detector and leave a clean track while most hadrons are absorbed in the iron yoke and fail to reach the muon detector. Of the full solid angle, 93% is covered by at least one layer of detector and over nearly all this the amount of material that a particle has to traverse exceeds 1.3 m of iron equivalent (over 7 interaction lengths for pions). This reduces the probability of a pion not interacting to less than 0.001.

Muon identification relies on extrapolating the track seen in the central tracking system through the absorber, allowing for energy loss and multiple coulomb scattering, and looking for a track in the muon detector which matches in position and angle in two views. The positional and angular accuracies required for the track measurement are determined by the multiple scattering of the highest energy muons of interest and are about 2 mm and 3 mrad respectively.

Ignoring the complexities of hadrons in jets, the efficiency for detecting isolated muons above 3 GeV and within the 93% solid angle is essentially 100%. The probability that an isolated pion of 5 GeV is misidentified as a muon is less than 1% .

2.6 Forward Detectors

The forward detectors measure the luminosity of LEP by detecting small-angle Bhabha scattering, and also tag electrons from $\gamma\gamma$ interactions. Figure 2.3 is a detailed cross-section through the forward detector between 2 and 3 m from the intersection region, showing the gamma catcher, the drift chambers, the fine luminosity monitor counters, the calorimeter and the tube chambers.

There is clean acceptance for particles from the intersection region between 47 and 120 mrad from the beam line. In this range the only obstructions are 2 mm of carbon fibre in the beam pipe (traversed obliquely, so up to 0.2 X_o thick) and 2 mm of aluminium in the thin window of the central tracking system pressure vessel, with aluminium webs in the horizontal and vertical planes to support the beam pipe. The front drift chambers and the "acceptance" counters of the fine luminosity monitor are mounted on the front of a light stiff honeycomb plate which has a thickness equivalent to 1 mm of aluminium. The inner part of the acceptance of the calorimeter, down to 39 mrad, is obstructed by a thick aluminium ring and by the bellows and flanges joining the beam pipe to the pressure window. Beyond 120 mrad there are obstructions inside the pressure vessel, including optics for the laser beams used to calibrate the jet chamber. The space which they occupy between the forward calorimeter and the endcap lead glass causes a gap in calorimetric acceptance in the polar angle region 142–

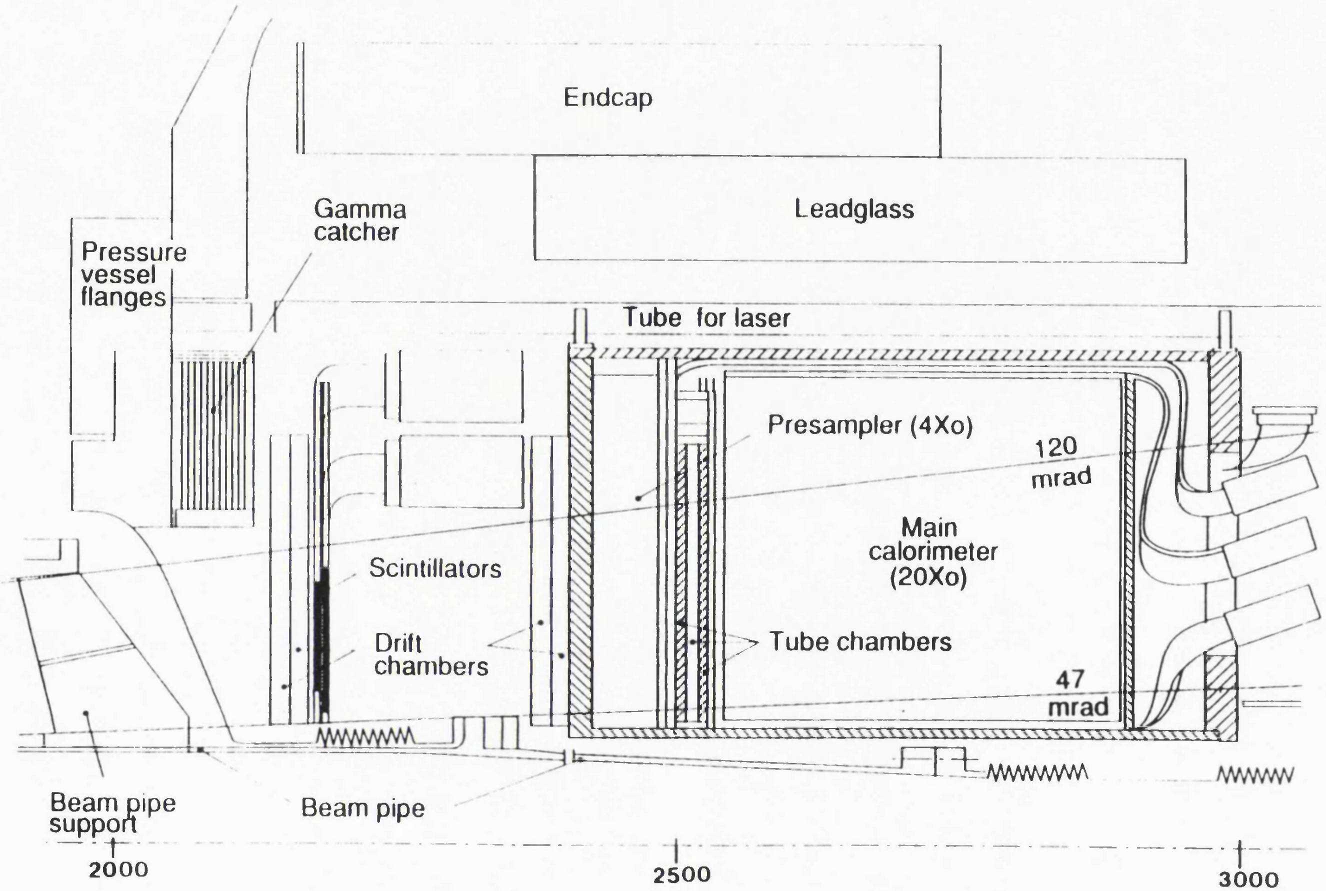

Figure 2.3: Cross section through the forward detector between 2 and 3 metres from the intersection region

200 mrad which is covered by the gamma catcher.

Calorimeter

The forward calorimeter has 35 layers of lead-scintillator sandwich (24 X_o), read out with wavelength shifter to vacuum phototetrodes. The front 4 X_o, the presampler, has wavelength shifter at the outside only, but the main calorimeter is read out on both the inner and outer edges to provide a θ measurement. There are sixteen azimuthal segments. The energy resolution has been measured as $\sigma_E/E \sim 18\%/\sqrt{E}$. The radial position resolution on electron showers is ±2 mm near the inner edge, but degrades towards the outer edge. The azimuthal resolution, from the ratios of signals in adjacent segments, is $\pm 1.5^\circ$ or less.

Tube Chambers

Between the pre-radiator and the main sections of the calorimeter are three planes of brass-walled proportional tube chambers. Individual showers can be measured to ± 3 mm. The tube chambers and the calorimeter provide a combined cluster where the θ and ϕ are taken from the tubes if the angle measured in the calorimeter is $\theta > 53$ mrad. The energy comes from the calorimeter which also provides θ and ϕ outside the tube acceptance. measurement

Drift Chambers

The drift chambers, as used in 1989-1991, each have two gas gaps with two sense wires per gap. Drift directions are approximately radial. The ambiguity between inward and outward drifts is resolved by displacing the sense wires in the first gap of each chamber outwards by 2 mm from those in the second gap. The position of a hit along a wire is measured by charge division and by a pattern of intersecting diamond pads on the faces close to the wires. These have been used to accurately survey the positions of the tubes within the calorimeter.

Fine Luminosity Monitor

The fine luminosity monitor consists of four pairs of precisely positioned 6 mm thick scintillators at each end, on the 45° diagonals to avoid showers from the beam pipe support webs. They cover the angular region 50–109 mrad from the beam axis, with an azimuthal coverage of about 36%. The front "acceptance" counters are 10 mm smaller on all sides than the rear "coincidence" counters. They provided a luminosity measurement used to check the main calorimeter/tube based measurement.

Gamma Catcher

The gamma catcher is a ring of lead-scintillator sandwich modules, 7 $X_{\circ}$ thick, with wavelength-shifter readout to silicon photodiodes. There is no θ information and there are eight segments in the ring. The energy resolution for bhabhas is $\simeq 20\%$. Although not discussed further in this thesis I have been partially responsible for the commission and running of the gamma catcher and the development of the reconstruction code.

Far Forward Monitor

The far forward luminosity monitor counters are small lead-scintillator calorimeters (50 mm × 150 mm × 20 $X_{\circ}$) mounted on either side of the beam pipe 7.85 m from the intersection region, beyond the low-beta quadrupoles. They are used for a high statistics "online" luminosity and to monitor beam backgrounds.

2.7 Trigger and Data Stream

Here details of the OPAL data stream are provided including some of the hardware elements used. The overall scheme of event triggering, readout, monitoring and data recording is shown in fig. 2.4.

Trigger

The trigger system [26] is designed to provide high efficiency for the various physics reactions, and good rejection of backgrounds arising from cosmic rays, from interactions of the beam particles with the gas inside the beam pipe or the wall of the beam pipe, and from noise. Most of the physics reactions are triggered by several independent conditions imposed on the subdetector signals.

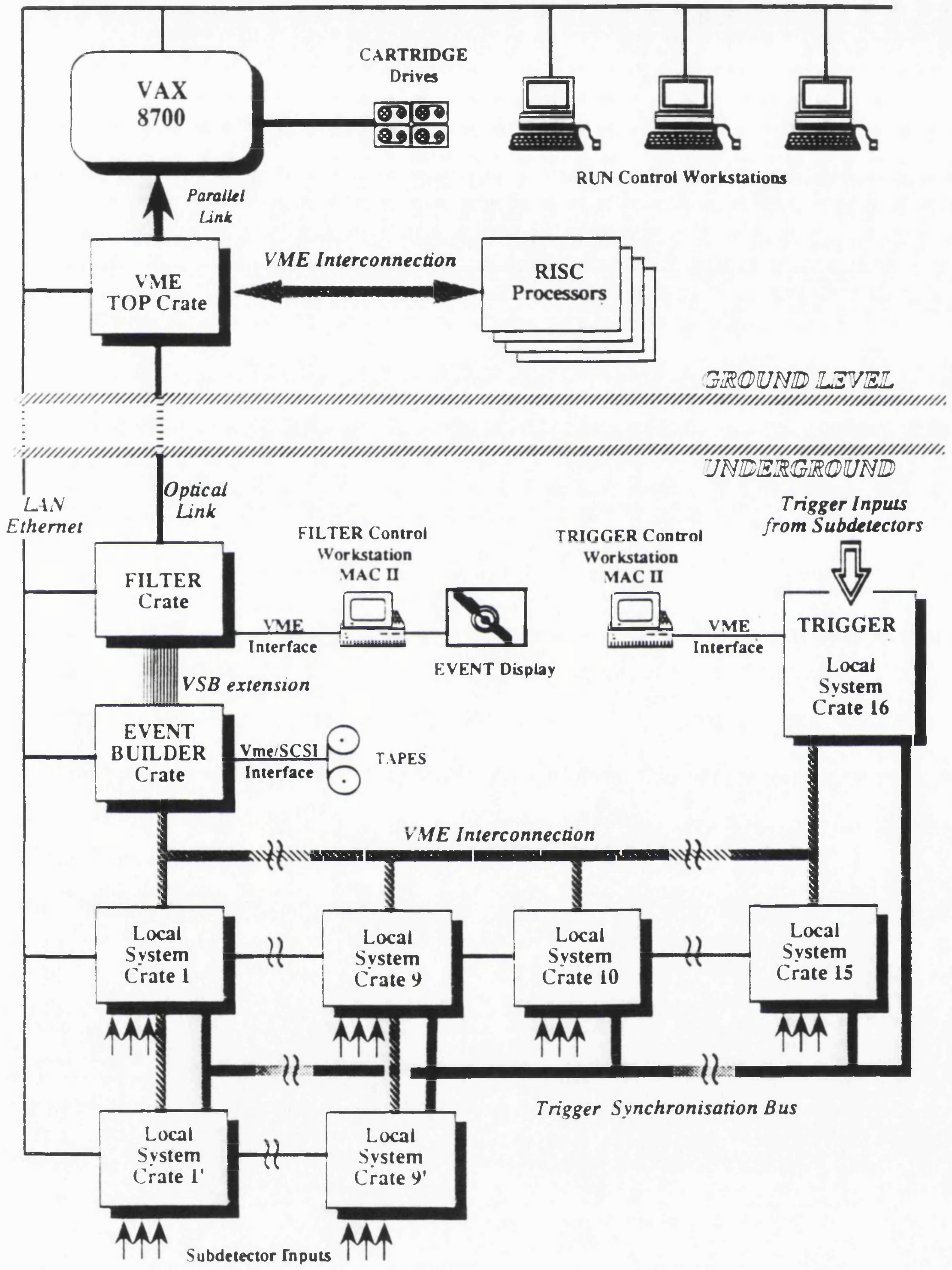

Figure 2.4: Overall scheme of event triggering, readout, monitoring and data handling.

This redundancy leads to a high detection efficiency and greatly facilitates the measurement of this efficiency.

The 4π range in solid angle covered by the detector is divided into 144 overlapping bins, 6 bins in θ and 24 bins in ϕ. The subdetectors deliver trigger signals matched as closely as possible to this binning. This fine segmentation allows low thresholds for the calorimeters, since analogue sums are made over only a small region to reduce noise. Besides the θ-ϕ signals, the subdetectors deliver "stand-alone" signals, derived from total energy sums or track counting.

The trigger signals from the various subdetectors are logically combined in the central trigger logic. θ-ϕ signals are used for hit counting, for the definition of back-to-back hits and to build detector coincidences correlated in space. Programmable conditions are imposed on the θ-ϕ matrix outputs and on the stand-alone signals to decide whether an event is accepted or rejected.

The trigger decision is broadcast to local trigger units (LTUs) in each subdetector readout crate by the global trigger unit (GTU). If the trigger decision is negative, a reset pulse is distributed 6 μs before the next bunch crossing. If an event is to be accepted, the GTU generates a trigger pulse, and transfers a central event number and the 120 PAM input bits to the LTUs. The wired OR of "busy" signals asserted by each LTU inhibits further triggers as long as the front-end readout is in progress.

Data Stream

The readout system has a distributed tree structured architecture. Microprocessors of the 68020/68030 type, running the OS9 operating system are used in a VMEbus based system for data compression and data moving as well as monitoring.

The sub-events containing the digitised information of the subdetectors are buffered in memories controlled by the subdetector processors and then collected and merged into a single data structure by an "event builder" VME system. This system also acts as an event buffer for a microprocessor matrix, where up to ten

68030 (in 1991 - later improved to an APOLLO DN10K), in parallel, perform a first analysis of the complete events, and undesired background can be rejected at this stage. From here, events are transferred from the underground experimental area via an optical link to the surface, where they are buffered in another microprocessor controlled VME system. From here it is picked up by fast APOLLO DN10K processors which run the full OPAL reconstruction code ROPE [27].

Chapter 3

The Structure of the Photon

As mentioned above the aim is to extract $F_2(x, Q^2)$ from our data. In this chapter we indicate why the data can be analysed in this way and highlight some of the theoretical problems which occur.

3.1 Helicity Structure

The transition matrix for $e^+e^- \rightarrow e^+e^-X$ in figure 1.1 can be factorized into three terms: one for the electron photon vertex, one for the positron photon vertex and one for the coupling of the photons to the hadronic system X. The $e^+e^-\gamma$ vertices determine the fluxes and helicities of the two photons, and the coupling to the hadronic system is the unknown part which we want to measure.

The total differential cross section for unpolarized electron beams is given by [28]:

$$\frac{d\sigma}{d\Gamma} = L^{TT}\sigma_{TT} + (L^{TL}\sigma_{TL} + L^{LT}\sigma_{LT}) + L^{LL}\sigma_{LL}\tilde{L}^{TT}\tau_{TT}cos(2\phi) + \tilde{L}^{TL}\tau_{TL}cos(\phi) \tag{3.1}$$

where

$$d\Gamma \equiv \frac{d^3k_1 d^3k_2}{E_1 E_2}.$$

k_i is the 3-momentum of the ith final state quark, and E_i is its energy. The luminosities $L, \tilde{L}$ for the transverse (T) and longitudinal (L) fluxes are known and calculable in QED. The σ's are the cross sections of interest (σ_{TT} is the cross section for a transverse photon colliding with a transverse photon etc.) and the τ's are interference terms, with ϕ the angle between the electron and positron scattering planes. These τ terms vanish when integrated over ϕ. In the limit where $P^2 = 0$ (single tagging) the only terms to survive are the σ_{TT} and σ_{TL} which can be studied as a function of x and Q^2. These are related to $\mathrm{F}_2(x, Q^2)$ and $\mathrm{F}_1(x, Q^2)$ by

$$\begin{aligned} \mathrm{F}_1(x, Q^2) &= \frac{Q^2}{8\pi^2 \alpha x}\sigma_{TT} \\ \mathrm{F}_2(x, Q^2) &= 2x\mathrm{F}_1(x, Q^2) + \frac{Q^2}{4\pi^2\alpha}\sigma_{LT} \end{aligned} \qquad (3.2)$$

3.2 The Hadronic Structure of the Photon

As discussed in section 1.2 the hadronic structure of the photon can be separated into two distinct types. In one, figure 1.2(a), the target photon couples directly to a hadronic vector meson state, this Vector Meson Dominance (VMD) coupling being large for $P^2 \lesssim m_v^2$, where m_v^2 is the mass squared of the vector meson. Alternatively the photon can couple in a pointlike manner as in figure 1.2(b), where the $\gamma q\bar{q}$ coupling is similar to the γe^+e^- coupling of QED. This is dominant when:

(i) $P^2 \gg m_v^2$ or

(ii) Large p_t is generated at the $\gamma q\bar{q}$ vertex.

Large p_t implies large virtuality:

$$t = -(p - k_1)^2 + m_q^2 \qquad (3.3)$$

of the exchanged quark (see figure 1.1), which is related to the p_t generated at the vertex by:

$$t = \frac{Q^2}{2x}\left[1 - \left(1 - \frac{4(p_t^2 + m_q^2)}{W^2}\right)^{\frac{1}{2}}\right] . \qquad (3.4)$$

So if one line (quark or photon) at the $\gamma q\bar{q}$ vertex is highly virtual then the coupling is pointlike and the VMD coupling is dominant only when $P^2 \leq m_v^2$ <u>and</u> p_t is small.

3.2.1 Vector Meson Dominance

In the VMD picture the target photon fluctuates into one of the lowest mass vector mesons (ρ, ω, ϕ) and the virtual probing photon sees the structure of this hadron. Ignoring gluon emission the VMD structure function should exhibit Bjorken scaling. With gluon emission the x-distributions should shift to smaller x as the Q^2 of the probing photon grows. This is because the probe can then resolve smaller distances and more momentum goes into radiated gluons. It is assumed that the quark distributions for the vector mesons are similar to those of the pion as measured in the Drell-Yan [23] process [29]

$$q_i^\pi(x) \sim (1-x)/x \tag{3.5}$$

This leads to [14]

$$F_2^{\gamma,VMD}(x) = \alpha(0.2 \pm 0.05)(1-x) \tag{3.6}$$

where the error comes from summing the contributions from the lowest vector meson states coherently $(0.16(1-x))$ or incoherently $(0.21(1-x))$.

Subsequent attempts to parameterize the pion structure function [30] modified by the same pion/photon conversion used to obtain 3.6 leads to:

$$F_2^{\gamma,VMD}(x) = \alpha 0.22 x^{0.41}(1-x)^{0.95} + (0.26 \pm 0.09)(1-x)^{8.4} \tag{3.7}$$

This equation is only valid for $x > 0.2$ so TPC/2γ [5] fitted their low Q^2 data with:

$$F_2^{\gamma,VMD}(x) = \alpha A x^{\alpha}(1-x)^{0.95} + B(1-x)^{\beta} \tag{3.8}$$

with the result given in equation 5.9

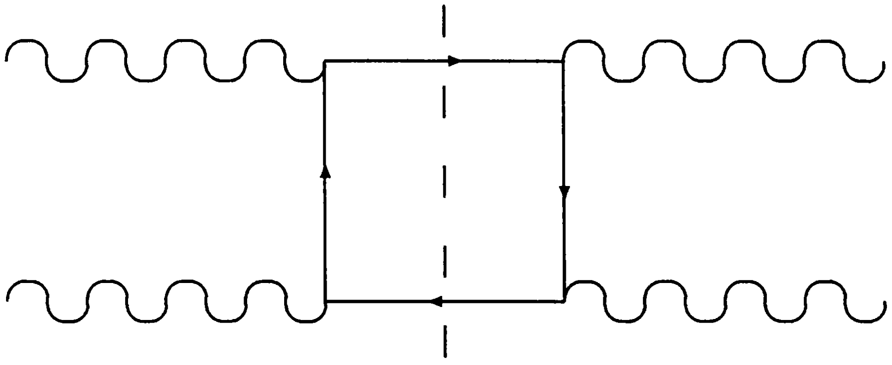

Figure 3.1: The QPM box diagram.

3.2.2 The Quark Parton Model

As mentioned above, the photon also couples to the quarks in a pointlike manner. In this section the quark parton model result is presented and the QCD calculation is sketched in the next.

The quark parton model was developed in order to explain the deep inelastic electron-nucleon data. The QPM prediction for $F_2(x, Q^2)$ is calculated by evaluating the s-channel discontinuity of the box diagram (figure 3.1). It gives [15]:

$$\frac{F_2(x,Q^2)}{\alpha} = \frac{3x \sum e_q^4}{\pi}\left[(x^2 + (1-x)^2)\ln\left(\frac{Q^2(x-1)}{m_q^2 x}\right)\right] - 1 + 8x(1-x) \quad (3.9)$$

It is immediately apparent that $F_2(x, Q^2)$ does not scale, but exhibits logarithmic scale breaking (as $F_2(x, Q^2)$ is a function of $\ln(Q^2)$). As can be seen in figure 3.2 QPM predicts x and Q^2 behaviour which is dramatically different from those of the VMD model (as parameterized in equation 3.8). However, it is known that quarks are not free objects and are subject to gluon corrections. For an improved calculation we thus turn to quantum chromodynamics.

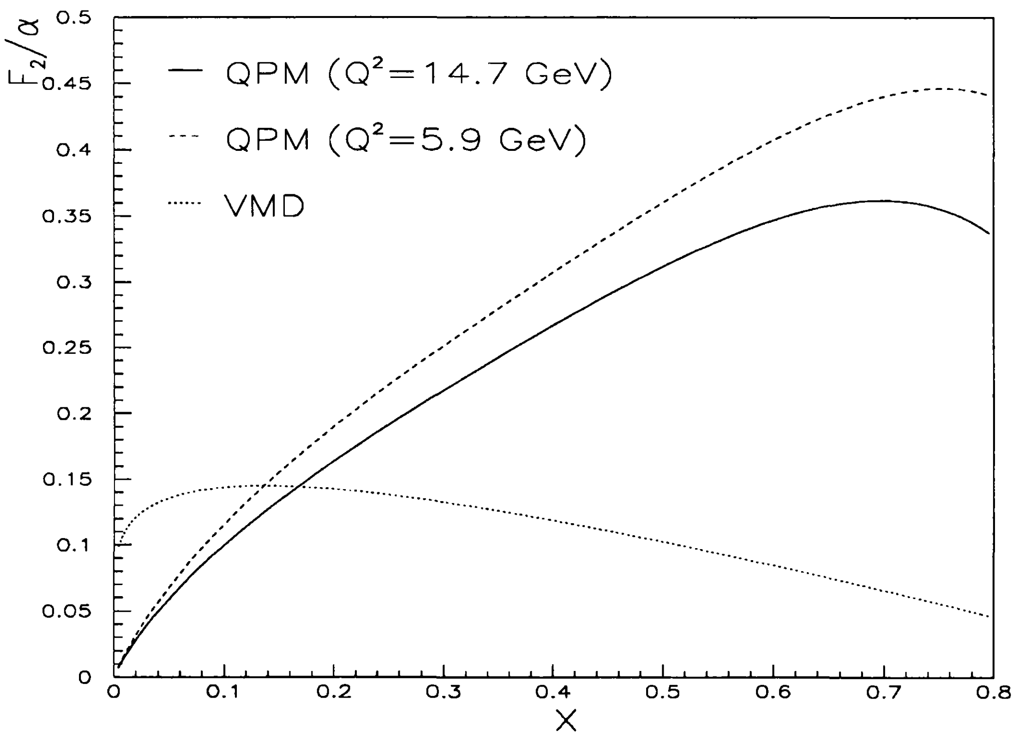

Figure 3.2: Comparison of QPM and VMD predictions for $F_2(x)$

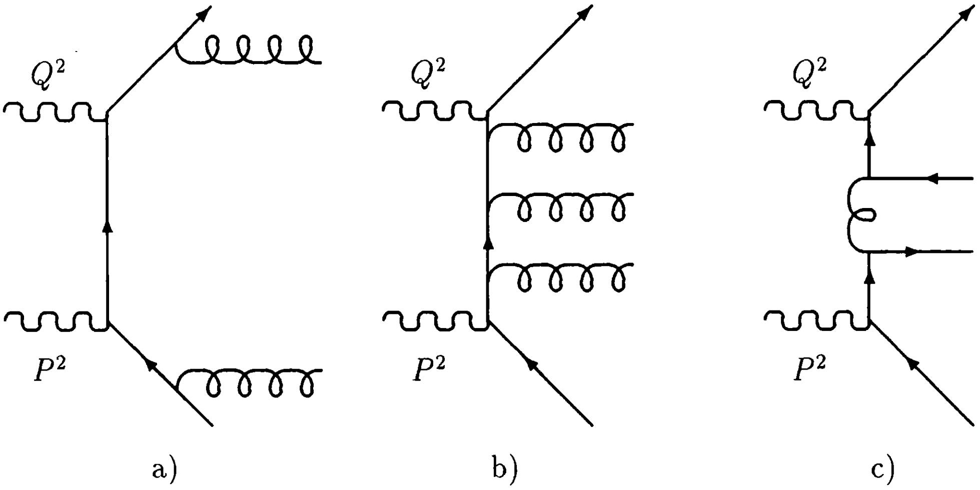

Figure 3.3: Classes of gluon radiative diagrams. - a) Enters into the fragmentation scheme. In b) the valence quark and c) the sea quark structure of the photon is probed.

3.2.3 The QCD Result

QCD calculations will modify the asymptotic QPM calculation to account for various classes of gluon radiation. If the gluons are radiated by the external quark lines, figure 3.3(a), then the kinematics of the hard scattering are not affected, and this radiation is included in the quark fragmentation model. If one or more gluons are radiated from the internal quark line, figures 3.3(b) and (c), then the hard scattering is modified. Qualitatively this causes the structure function to be shifted to smaller x values since the probing photon sees a quark with smaller momentum, though the logarithmic growth with Q^2 is preserved.

Leading log predictions for F_2^γ have been obtained by many authors using either the operator product expansion and renormalization group equations (OPE-RGE), an Altarelli-Parisi evolution or directly summed Feynman diagrams. These approaches lead to similar results, but controversy has arisen over the precise physical interpretations. In particular the identification of particular terms as "hadronic" or "pointlike" parts of F_2^γ has been argued over. Here the diagrammatic approach is followed at the one loop level.

If the same quark couples to both the target and the probing photon, figure 3.3(b), then only the valence contribution of the photon is probed, whereas the sea quark component is probed by diagrams like that in figure 3.3(c). It has been shown [31] that the sea contribution is small except for x close to zero. In the following discussion the sea contribution is ignored.

For F_2^{HAD} the coupling between the target photon and the hadron system is modelled by VMD as stated above. The quark densities $q_i^{HAD}(x, Q^2)$ defined in section 1.2 are given by the Altarelli-Parisi type equation [22]:

$$q_i^{HAD}(x, Q^2) = q_i^{HAD}(x, t_0) + \int_x^1 \frac{dz}{z} \int_{t_0}^{Q^2} \frac{dt}{t} \frac{\alpha_s(t)}{2\pi} q_i^{HAD}(z, Q^2) P_{qq}(\frac{x}{z}) \qquad (3.10)$$

where $P_{qq}(\frac{x}{z})$ is the Altarelli-Parisi splitting function [32] (which is the probability to find a quark of momentum fraction x inside a quark with momentum fraction z) and t_0 is the value of t (the virtuality of the exchanged quark - see equation 3.4) which is at the boundary between the hadronic and pointlike region of phase space. In words the above represents some incalculable hadronic piece added with a piece which predicts its Q^2 evolution. The evolution is carried out from some reference t_0 below which the quark is assumed to be in the vector meson.

If we then take Mellin moments according to:

$$q(n) = \int_0^1 x^{n-1} q(x) dx \qquad (3.11)$$

equation 3.10 is solved for $q(n, Q^2)$:

$$q_i^{HAD}(n, Q^2) = q_i^{HAD}(n, t_0) \left[\frac{\alpha_s(Q^2)}{\alpha_s(t_0)} \right]^{-d_n} \qquad (3.12)$$

with

$$d_n = d_{qq}^n = b P_{qq}(n) \quad \alpha_s(Q^2) = b / ln(Q^2/\Lambda^2) \qquad (3.13)$$

The infinite series which is summed to get this result is shown in figure 3.4(a). The pointlike part comes from summing the series given in figure 3.4(b) where the VMD coupling of the target photon is replaced by a pointlike coupling. If we now think of the above result in terms of $S_n(Q^2, t_0)$ the sum of the convolution integrals generated by integrating over the final state gluons and quarks appearing above the dotted line in figure 3.4(a) then

$$q_i^{HAD}(n, Q^2) = q_i^{HAD}(n, t_0) S_n(Q^2, t_0) \qquad (3.14)$$

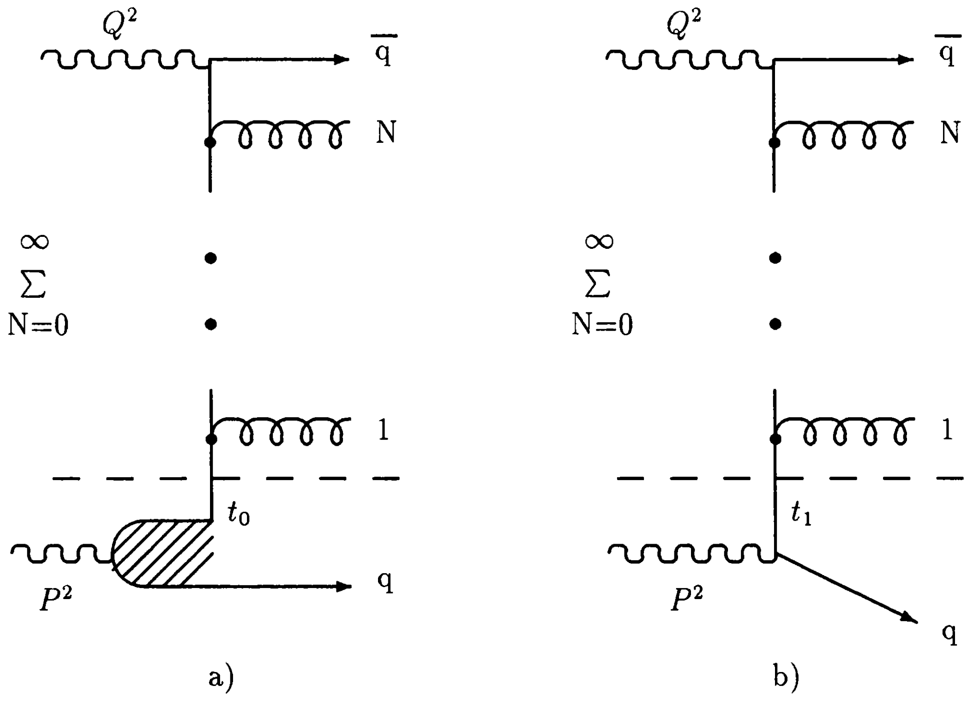

Figure 3.4: Dressed Feynman diagrams giving the valence part of a) F_2^{HAD} and b) F_2^{PL}. The structure of each diagram is the same above the dotted line.

By inspection of the pointlike part in figure 3.4(b) the moments of the pointlike part are given by:

$$q_i^{PL}(n,Q^2) = a(n)\int_{t_0}^{Q^2}\frac{dt_1}{t_1}S_n(Q^2,t_1) \tag{3.15}$$

where a is the photon-to-quark splitting function:

$$a(x) = \frac{3\alpha}{2\pi}e_i^2[x^2+(1-x)^2] \tag{3.16}$$

Comparing equations 3.12 and 3.14 $S_n(Q^2,t_1) = [\alpha_s(Q^2)/\alpha_s(t_1)]^{-d_n}$ and doing the integral over t_1 in 3.15 gives:

$$q_i^{PL}(n,Q^2) = \frac{a(n)}{(1-d_n)}ln\left(\frac{Q^2}{\Lambda^2}\right)\left\{1-\left[\frac{\alpha_s(Q^2)}{\alpha_s(t_0)}\right]^{1-d_n}\right\} \tag{3.17}$$

which is the result first obtained by Witten [15].

The two terms above in q^{PL} have different Q^2 behaviours. The first (represented by the "1" in the curly brackets) is generally referred to as the leading log (LL) term and dominates in the limit $Q^2 \rightarrow \infty$. The second term $\rightarrow 0$ as $Q^2 \rightarrow \infty$ since $d_n < 0$, and will be called non leading log (NLL).

From the outline given above it is clear that $q_i^{HAD}(n,Q^2)$ and $q_i^{PL}(n,Q^2)$ should simply be added to give the complete leading order (LO) result, since they correspond to different phase space regions of the variable t_1:

$$\begin{aligned} \text{hadronic} &: \; t_{min} < t_1 < t_0 \\ \text{pointlike} &: \; t_0 < t_1 < Q^2 \end{aligned}$$

Thus:

$$q_i^{LO}(n,Q^2) = q_i^{HAD}(n,Q^2)r^{-d_n} + \frac{a(n)}{(1-d_n)}ln\left(\frac{Q^2}{\Lambda^2}\right)\left[1-r^{1-d_n}\right] \tag{3.18}$$

where $r = \alpha_s(Q^2)/\alpha_s(t_0)$. Leading order means that only one loop effects are included in the splitting functions and α_s.

The OPE-RGE result is often written:

$$q_i^{LO}(n,Q^2) = \frac{a(n)}{(1-d_n)}ln\left(\frac{Q^2}{\Lambda^2}\right) + \tilde{A}(n,\mu^2)\left[\frac{\alpha_s(Q^2)}{\alpha_s(\mu^2)}\right]^{-d_n} \tag{3.19}$$

with μ as an arbitrary renormalization scale. The first term has usually been referred to as "pointlike" (as it is the only one which survives as $Q^2 \rightarrow \infty$) and the second, which has the usual hadronic Q^2 evolution property, has normally been identified as the VMD photon hadron coupling as shown in figure 1.2(a). The derivation above shows that this "hadronic" term contains terms originating from both VMD *and* PL couplings. Comparing equations 3.19 and 3.18 gives that the two are identical if $\mu^2 = t_0$ and

$$\tilde{A}(n,\mu^2) = q_i^{HAD}(n,Q^2) + \frac{a(n)}{(1-d_n)} ln\left(\frac{t_0}{\Lambda^2}\right) \tag{3.20}$$

3.2.4 Sensitivity to $\Lambda_{\overline{MS}}$

The sensitivity to $\Lambda_{\overline{MS}}$ is examined using the parameterization given in equation 5.2 at $Q^2 = 10$ GeV^2. This is based on an all order QCD calculation by Kapusta [33] which introduces a cut-off parameter to separate the VMD and perturbative QCD parts as discussed above. This cutoff, p_t^0, is in the p_T of the quarks at the target $\gamma q\bar{q}$ vertex.

There are four curves shown in figure 3.5. Two represent changing $\Lambda_{\overline{MS}}$, for a fixed p_t^0, over a reasonable range [34] and two varying p_t^0, for a fixed $\Lambda_{\overline{MS}}$. The values of $\Lambda_{\overline{MS}}$ and p_t^0 for each curve are given in 3.21.

$$\begin{array}{ll} \left.\begin{array}{ll} \text{(a)} & \Lambda_{\overline{MS}} = 0.1 \text{ GeV} \\ \text{(b)} & \Lambda_{\overline{MS}} = 0.5 \text{ GeV} \end{array}\right\} & p_t^0 = 0.5 \text{ GeV} \\ \left.\begin{array}{ll} \text{(c)} & p_t^0 = 0.1 \text{ GeV} \\ \text{(d)} & p_t^0 = 1.0 \text{ GeV} \end{array}\right\} & \Lambda_{\overline{MS}} = 0.2 \text{ GeV} \end{array} \tag{3.21}$$

As can be seen the difference between curves (a) and (b) (where $\Lambda_{\overline{MS}}$ is varied) is similar to that between (c) and (d) (where p_t^0 is varied). Since p_t^0 is theoretically uncertain to the extent varied, this clearly precludes any sensitive measurement of $\Lambda_{\overline{MS}}$ within this parameterization in this Q^2 range. No such measurement has been attempted in this thesis, and $\Lambda_{\overline{MS}}$ has been set to 200 MeV.

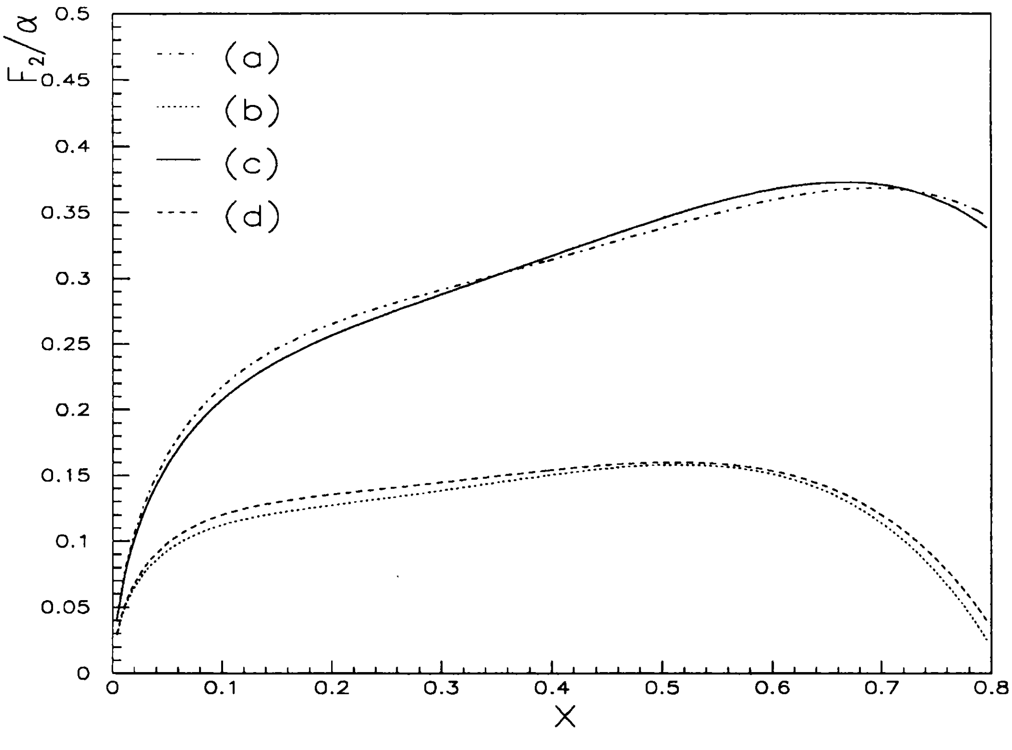

Figure 3.5: The effect of varying (a),(b) $\Lambda_{\overline{MS}}$ and (c),(d) p_t^0 on $F_2(x)$.

Chapter 4

Event Selection

This chapter describes the selection of single tagged two photon events starting from an offline software preselection. The remaining backgrounds (after applying all the cuts) are estimated. A measurement of the trigger efficiency is made using the final data sample. Finally a consistency check is presented where the data taken in the year 1991 is compared with that taken in 1990.

4.1 Event Selection.

The event selection process starts with an online preselection (called PHYS1). A series of cuts are then applied to these preselected events to assure both that the information used is of good quality and that, as far as possible, the final selected events are single tagged two photon events.

4.1.1 PHYS1 Selection

Within online ROPE there is a loose physics preselection called PHYS1 which is designed to pick out events which will be of interest to the various analysis groups in OPAL. These events are written to disk on the SHIFT [35] processor farm where they are easily accessible using the standard OPAL analysis framework

MAW [36, 37].

The physics preselection cuts used to identify potential tagged two photon candidates are:

- A tag of greater than 15 GeV in either forward calorimeter.
- Number of tracks ≥ 2. Track quality cuts are similar to those given in table 4.2.

The PHYS1 preselected events from 1990 and 1991 data are plotted in Figure 4.1 which shows the distribution of the events in the dimensionless missing momentum variables k_L and k_T, defined by

$$k_L \equiv |({p_L}^{TAG} + {p_L}^{TRACKS} - E_{BEAM})|/E_{BEAM},$$

and

$$k_T \equiv ({p_T}^{TAG} + {p_T}^{IN})/{p_T}^{TAG}.$$

Here, ${p_T}^{TAG}$ is the transverse momentum of the tagged lepton with respect to the beam, ${p_L}^{TAG}$ is the component of the tag momentum along the beam direction, ${p_L}^{TRACKS}$ is the component of the total momentum of the good quality (see section 4.1.2) charged tracks along the beam direction, and ${p_T}^{IN}$ is the component of the total transverse momentum of the charged tracks in the plane defined by the tag and the beam (called the tag plane).

The tagged two photon events are expected to be in the region $k_T \simeq 0$ because the p_T of the unseen electron is limited to $\lesssim 2$ GeV/c. They are also expected to lie close to $k_L = 0$, as the momentum of an assumed missing electron has been added to the visible p_L. The peak near the origin thus represents the tagged two-photon signal, with the peak close to $k_T = 1$ being background. One candidate for this background is that of tags caused by off momentum beam particles randomly in conjunction with ordinary hadronic events (either Z^0 decays or untagged two

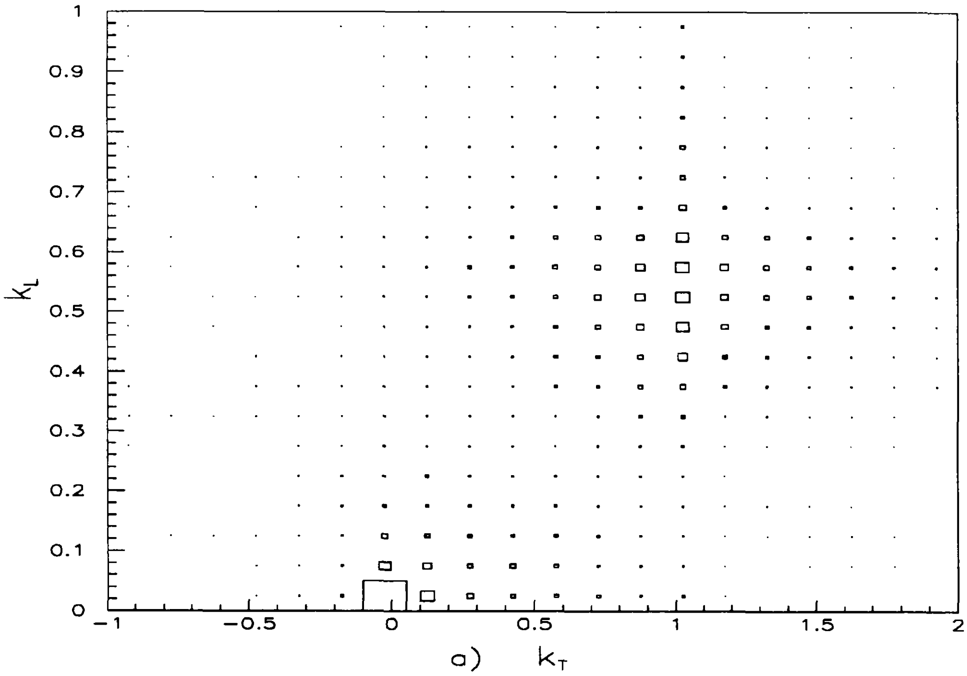

Figure 4.1: Distribution of events in scaled missing momenta k_T and k_L.

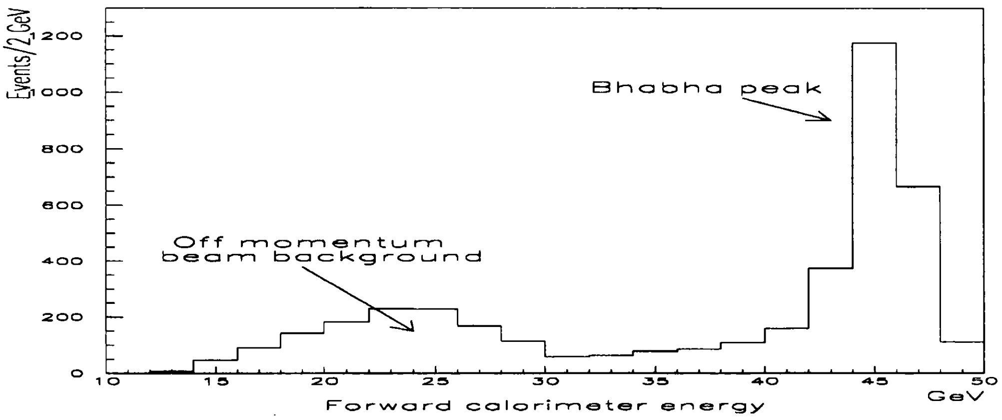

Figure 4.2: The energy distribution for the positron in potential Bhabha events.

photon events). These off momentum beam e$^{\pm}$ can also be seen in Bhabha events. In figure 4.2 the energy in the left side forward calorimeter has been plotted for all events which have been selected by OPAL forward detector luminosity triggers and which have a left side tube cluster (and are thus well contained). The effect of the luminosity triggers is to pick out events which have $\gtrsim$15 GeV clusters in both forward detectors. There are two clear peaks visible; a bhabha peak near 45 GeV and an off momentum background peak near 25 GeV.

From this we would expect our off momentum background to be in the region $k_L \simeq 0.5$, as the off momentum peak occurs at about $E_{BEAM}/2$, and $k_T \simeq 1$ if the hadronic system is balanced. The background visible in figure 4.1 should therefore be removed by a high tag energy cut. Figure 4.3(a) shows the above distribution after cutting on the tag energy such that $E_{TAG} > 0.7E_{BEAM}$ and figure 4.3(b) shows the events that fail this tag energy cut. The background behaviour is thus shown to be consistent with a random off momentum tag together with a hadronic system balanced in p_T and p_L.

The figures 4.1, 4.3(a) and 4.3(b) show that a large part of the background to the tagged two photon events can be removed by a tag energy cut of $E_{TAG} >$

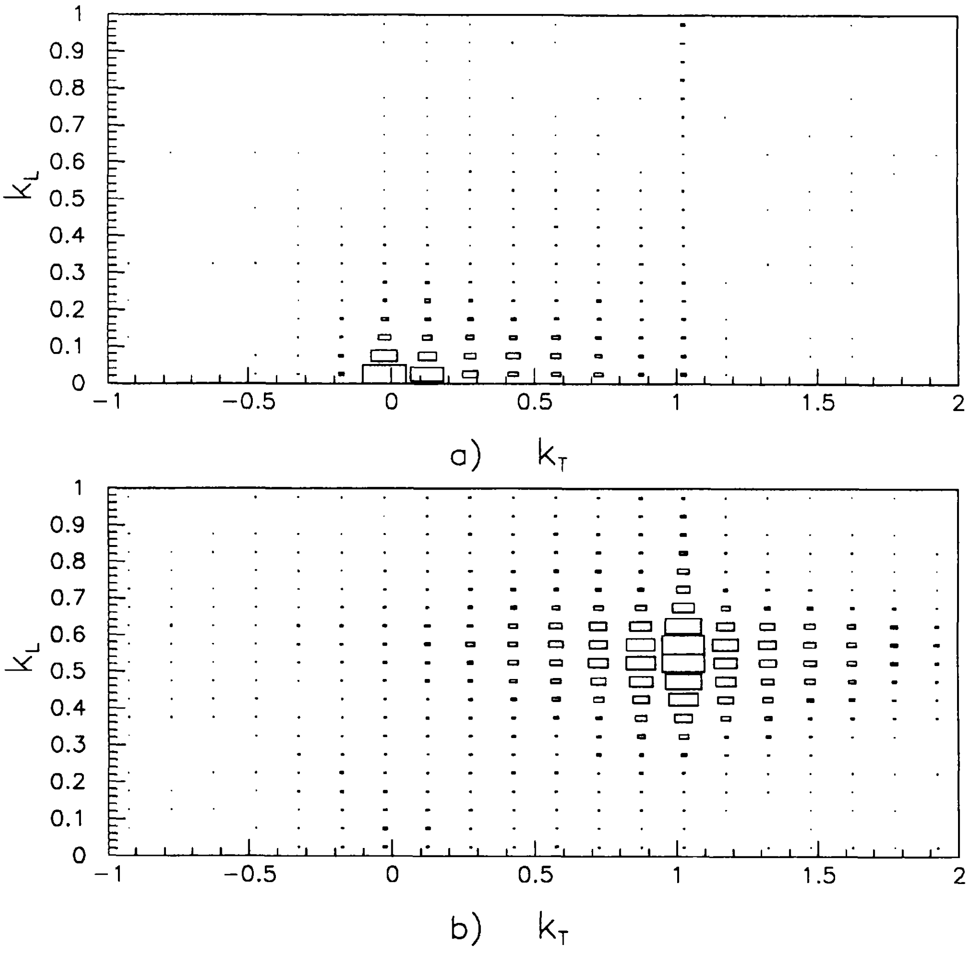

Figure 4.3: Distribution of events in scaled missing momenta k_T and $k_L$which a) pass and b) fail a high tag energy cut of $E_{TAG} > 0.7E_{BEAM}$.

$0.7E_{BEAM}$. A further cut on the polar angle θ_{TAG} is applied to the tagged electron,

$$47 < \theta_{TAG} < 120\,\mathrm{mrad}.$$

This θ_{TAG} cut ensures that the tag is restricted to the well understood region of the forward detector, and thus that Q^2 is well measured. A histogram comparing the Q^2 for 1990 data with 1991 data is shown in figure 4.7(d). Further cuts are needed to ensure both that the information we use is reliable and that the sample contains minimum amounts of other types of background. These cuts are described in the next two sections.

4.1.2 Quality Cuts.

Each subdetector provides a status word for every event which provides information on whether the detector is working properly. The values of the status word and the meanings attached are summarized in table 4.1. We require that the status of the FD, EB and CJ are all ≥ 2 and the track trigger status is 3. This defines a sample of events for which the main subdetectors used in the analysis are working well and are providing reliable information.

Status	Meaning
0	Detector is dead
1	Detector is unreliable
2	Detector has small problems
3	Detector is 100%

Table 4.1: Detector status word and meanings.

Q^2 is calculated from the measured θ_{TAG} and E_{TAG} (equation 1.3), but to calculate x we need to measure the invariant mass W (equation 1.4) of the hadronic system. In double tagging this might be done by measuring the angles and energies of both detected electrons, but in the single tagging case we must measure it from the detected hadrons. When this is done using tracking information only, the subscript *track* is added (x_{track}, W_{track}). When electromagnetic cluster information is also used the subscript *vis* is used (x_{vis},W_{vis}). Cuts are needed to ensure that the tracks and clusters that are used are of "good quality".

Tracks

Table 4.2 shows the cuts to ensure that all tracks used are of good quality. For each track we wish to ensure that it is well measured and thus,

- a minimum number of Jet chamber hits (N_{Hits}) on the track is demanded,
- a minimum angle of the track ($|\cos\theta_{Tr}|$) is demanded,
- the track must have a minimum p_T with respect to the beam.

It is also desirable to reject tracks due to jet chamber sparking, beam wall interactions, beam gas interactions and backscatter in the solenoid from the particles that have already left the chamber. It is therefore demanded that the track appears to have come from the interaction point. Cuts are made on z_0, the apparent z from which the track originated, d_0, the apparent perpendicular distance from the interaction point in the x-y plane from which the track originated, and R_{First} the radius of the first wire hit on the measured track.

Charged Tracks	$N_{Hits} > 20$
	$\cos\theta_{Tr} < 0.97$
	$p_T > 0.1$ GeV/c
	$R_{First} < 75$ cm
	$|d_0| < 2.5$ cm
	$|z_0| < 50$ cm

Table 4.2: Quality cuts applied to the tracks.

Electromagnetic Clusters in the Lead Glass

The cuts to ensure that only good quality neutral clusters are used are shown in table 4.3. We wish to ensure that any clusters used are not due to either badly calibrated blocks or noisy electronics. A list of blocks which are know to be noisy (or "hot") has been compiled, together with roughly how noisy they are, and each cluster is compared with this list. A cluster associated with a noisy block, and which is close in energy to the estimated noise, is not used in the analysis. The energy of a cluster is corrected to take account of energy deposited in the material in front of the lead glass, which leads to a large correction for clusters with small deposited energy E_{raw}, so we also make a cut on the raw cluster energy. For a cluster in the Electromagnetic Endcap (EE), which has a non pointing geometry (see section 2.3), we demand a minimum number of blocks (N_{Blocks}) in the cluster with no single block having more than Fr_{MAX}% of the (raw) cluster energy.

Track-Cluster Matching

If we use a track in our analysis it would be double counting to also use a cluster in the electromagnetic calorimeter that was produced by the impact of the same particle. Thus if a track is of good quality an attempt is made to match it to a cluster. A loop over all the good quality neutral clusters in the event is performed and if a cluster is within a cone of half-angle η radians then it is matched to the track. In the event of there being two such clusters within the cone then the cluster closest in angle to the track endpoint is chosen.

In summary:

- Only good quality tracks are used in the analysis.

- Only good quality clusters which are not associated with any tracks are used.

- One track is associated with a maximum of one cluster.

All Electromagnetic clusters	$E_{raw} > 0.17$ GeV Cluster is not "hot" Cluster is not associated with a track
EE clusters	$\mathrm{N}_{Blocks} > 2$ $Fr_{MAX} = 99\%$
Track/Cluster Matching	$\eta = 0.1$ rad

Table 4.3: Quality cuts applied to the neutral clusters and the track-cluster association cone.

4.1.3 Final Selection.

There are lots of backgrounds to the tagged multiperipheral events shown in 1.1 still remaining after the initial preselection and quality cuts. Further cuts have been applied to ensure that the remaining possible backgrounds shown in figure 4.4 are minimized . These consist of Z^0 annihilation events, radiative bhabhas or leptonic two photon events. This section discusses the various cuts to remove each type in turn. The final selection cuts are summarized in table 4.4.

Section 4.1.1 showed that the cut on E_{TAG} removes the background seen in figure 4.1. Further kinematic cuts are also made on the p_T of the events, but these cuts are not very "hard" (figures 4.8(a) and (b)). To further reduce the number of remaining Z^0 annihilation events (figures 4.4(c), 4.4(d) and 4.4(e)) a maximum W_{vis} cut is made.

As we are specifically interested in single tag events, an antitag cut is made which demands that no high energy cluster is seen in the opposite hemisphere from the tag. This removes any double tag events from the sample and also cuts down on any background from the radiative Bhabha type backgrounds shown figure 4.4(b) (these are also referred to as inelastic Compton scattering diagrams).

The backgrounds from the tagged two photon sample where two leptons are produced in place of two quarks (see figure 4.4(a)) are removed by a cut on the charged multiplicity of the event. As we are interested in hadronic events we demand that at least one track is likely to be a hadron by not positively being identified as a lepton. Muons are identified by the track being associated with hits in the muon chambers and electrons by using dE/dx information from the jet chamber. It is not possible to fully discriminate against $e^+e^- \rightarrow e^+e^- + \tau^+\tau^-$ and the amount of this background is estimated by Monte Carlo (see chapter 5).

To ensure reasonable trigger efficiencies we demand at least two tracks with a high reconstructed p_T. One track must have $p_T > 1$ GeV and another must have $p_T > 0.5$ GeV. A cut is made to ensure that W_{vis} is away from the resonance region so that the complicated structure in this region does not have to be modelled. To reduce any remaining beam-gas background it is demanded that the primary track vertex is reconstructed near to the interaction point in the z direction.

In 18.43pb^{-1} of data 596 events pass these cuts.

4.2 Estimation of Remaining Backgrounds

As well as the $e^+e^- \rightarrow e^+e^- + \tau^+\tau^-$ background, mentioned above, there is the possibility that some other background events remains in the sample. The possible sources are considered below.

4.2.1 $e^+e^- \rightarrow hadrons$

There is a small probability that a hadronic Z^0 decay could satisfy the two-photon selection criteria; however the resonant enhancement at the Z^0 peak makes this problem potentially more serious at LEP than at previous e^+e^- colliders.

Multiplicity	1 track with $p_T > 1$ GeV plus ≥ 1 track with $p_T > 0.5$ GeV ≥ 3 charged tracks
Kinematics	${p_T}^{TAG} + {p_T}^{IN} \leq 6$ GeV ${p_T}^{OUT} \leq 4$ GeV $2.5 < W_{vis} < 40$ GeV
Vertex	Within 10cm of the interaction point
Antitag	No electromagnetic cluster with $E > 0.25 \times E_{BEAM}$ in hemisphere opposite tag

Table 4.4: Cuts on global variables to remove backgrounds. ${p_T}^{IN}$ is defined in section and and ${p_T}^{OUT}$ is the total p_T of the charged tracks perpendicular to the tag plane .

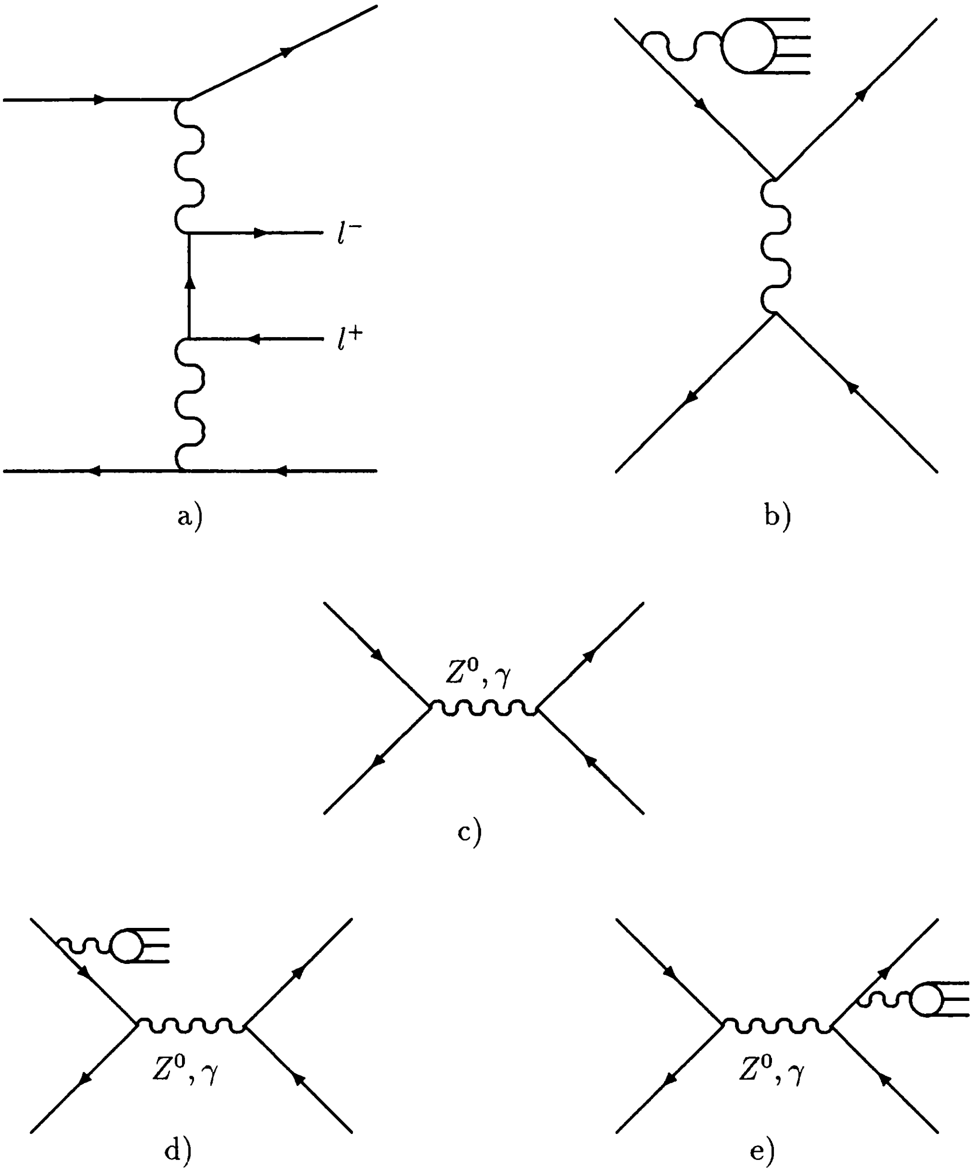

Figure 4.4: Backgrounds for the process $e^+e^- \to e^+e^- + hadrons$.

This has been investigated using a sample of approximately 560,000 Monte Carlo events simulated with the JETSET package [38]. The tag energy cut and the charged-track p_T requirements reject these events very effectively, with only eleven surviving the final two-photon selection. Scaling to the total multihadron sample of 410,000 [39] gives the following estimated background,

- Three events survive in the low-Q^2 range all in the lowest x bin, giving an estimated background of 2.2 ± 1.3 events.
- The remaining eight events all appear in the high-Q^2 region with the x distribution as shown in table 4.5.

x bin	Surviving MC events	Background events per multihadron	Estimated background
0.0-0.1	6	$(1.1 \pm 0.4) \times 10^{-5}$	4.40 ± 1.60
0.1-0.2	1	$(1.8 \pm 1.8) \times 10^{-6}$	0.72 ± 0.72
0.2-0.3	1	$(1.8 \pm 1.8) \times 10^{-6}$	0.72 ± 0.72

Table 4.5: Monte Carlo estimate of multihadronic background for $Q^2 > 8$ GeV^2.

4.2.2 $e^+e^- \rightarrow \tau^+\tau^-$

As in the hadronic case, tau pairs produced in Z^0 decay can in principle fake tagged two-photon events. An analysis of 72000 such events produced with the KORALZ generator [40] found no events satisfying our selection cuts; as the efficiency corrected total number of $\tau^+\tau^-$ events taken by OPAL is approximately 23,000 [39] in 1990 and 1991, the actual background is negligible.

4.2.3 Non-multiperipheral $e^+e^- \rightarrow e^+e^- + hadrons$

There are several processes other than the multiperipheral diagram of fig 1.1 which can give rise to the same final state. These processes have been studied using the Monte Carlo generator FERMISV [41]. The largest contribution arises from so-called "inelastic Compton scattering" [42], shown in fig 4.4(b). The resulting background is estimated as $(0.4 \pm 0.2)\%$ of the multiperipheral cross-section, or 2.4 ± 1.2 events. The Q^2 distribution of these events follows that of the multiperipheral sample; they are uniformly distributed in x between the values of 0.2 and 0.7. The effect of interference between the multiperipheral and inelastic Compton diagrams is found to be much less than the inelastic Compton cross-section, and can safely be neglected.

4.2.4 Beam-gas events

Background events arising from interactions with residual gas in the beam pipe would have their vertex position uniformly distributed along the beam axis. By moving the cut on the primary vertex out to ±50cm from the interaction point we admit four more events into the sample. Thus the estimated background under the ±10cm region is 1 ± 0.5 events.

4.3 Trigger Efficiency

Before we compare the data with the Monte Carlo (section 6.2) or indeed with itself (section 4.4) the trigger efficiency must be calculated. A list of the particularly relevant triggers for tagged two photon events and their descriptions is given in table 4.6. The triggers R(L)CALLO, TBM1, EBTOTLO and EER(L)LO do not cause the event to be read out but the coincidence (TBM1 .OR. EBTOTLO .OR. EERLO .OR. EELLO) .AND. (RCALLO .OR. LCALLO) does. All the other triggers cause OPAL to read out.

Trigger	Description
R(L)CALLO	$>$ 15 GeV deposited in right(left) forward calorimeter
FDHIOR	$>$ 35 GeV deposited in either forward calorimeter
TBM1	One track in the barrel region $\cos\theta < 0.7$
TM3	$\geq$ 3 tracks in the central detector
EBTOTLO	$\geq$ 4 GeV in the electromagnetic barrel (EB)
EER(L)LO	$\geq$ 4 GeV in the right(left) electromagnetic endcap (EE)
EBTPHI	$\geq$ 2.5 GeV in one EB $\theta - \phi$ bin
EER(L)TPH	$\geq$ 2.5 GeV in one EE $\theta - \phi$ bin
TPTTTO	coincidence between TOF hit and a track
TPTTEM	coincidence between EB or EE deposit and a track
TPTOEM	coincidence between EB or EE deposit and a TOF hit

Table 4.6: A summary of the mnemonics of the OPAL triggers involved in triggering tagged two photon events. The coincidences mentioned occur between hits/deposits in the same $\theta - \phi$ bin. A TOF hit is a hit in the Time Of Flight counter.

4.3.1 Efficiency Calculation

To estimate the efficiency of a particular trigger it is necessary either to model it with Monte Carlo or to compare it with another independent trigger. If we look at two independent triggers 1 and 2 which both are sufficient to cause readout (by independent we mean that the chance of 2 firing is unaffected by whether 1 has fired or not) then there are four classes of events; neither has fired, 1 only has fired, 2 only has fired and both have fired. The efficiency of each trigger is then calculated from events which fall into the latter three classes. If 1 only has triggered n_1 events in the final sample and 2 only has triggered n_2 events and both have triggered on n_{12} events then the efficiency of trigger 1 (ε_1) is:

$$\varepsilon_1 = \frac{n_{12}}{n_{12} + n_2} \tag{4.1}$$

The efficiency of 2 can be calculated in an analogous manner. If every event fires at least one of the two triggers (and assuming that an event that fires neither is not recorded) then the total trigger efficiency can be be estimated:

$$\varepsilon_{Total} = \left[1 - \left(1 - \frac{n_{12}}{n_{12} + n_2}\right)\left(1 - \frac{n_{12}}{n_{12} + n_1}\right)\right] \tag{4.2}$$

4.3.2 Efficiency Estimation from the Data

As said above our events can either be trigger-selected by

- The tag in the forward detector generating an FDHIOR trigger.
- The hadronic activity generating various central track and/or calorimeter triggers (such as TPTTEM, EBTPHI, EEL(R)TPH, TPTOEM, TPTTTO, TM3)
- The coincidence (TBM1 .OR. EBTOTLO .OR. EERLO .OR. EELLO) .AND. (RCALLO .OR. LCALLO)

In our final sample of analysis events, either RCALLO or LCALLO fires on every event. Thus we never pick up the presence of a tag only from the reconstructed energy in the Forward Calorimeter and our measured efficiency for this trigger is 1 (or 100%). As R(L)CALLO is measured to be 100% efficient then the triggers TBM1, EBTOTLO and EER(L)LO are each sufficient to cause OPAL to read out for tagged two photon events.

We need independent triggers to calculate our trigger efficiency so we form the logical .OR. of all the central triggers (triggering off the hadronic activity) listed in table 4.6 (ie all bar R(L)CALLO AND FDHIOR) and call this the CENTRL trigger. We then look at the subset of events which has been selected by this trigger and the subset of events which has been selected by the FDHIOR trigger. The reason that we form the logical .OR. is that even though some of the central triggers are electronically independent, they are not necessarily physically independent. For instance the trigger TPTOEM is electronically independent of TBM1. However it guarantees that a high energy charged particle has gone into the barrel region, which biases the estimate of the TBM1 trigger efficiency.

The FDHIOR trigger was only installed late in 1990, which means that a reasonably efficient stand alone trigger that is independent of the central hadronic system was not available in that year. It is therefore assumed we can measure the 1990 trigger efficiency using the 1991 data, ie that the measured 1991 CENTRL efficiency is also the total 1990 trigger efficiency. This assumption is tested as far as possible and discussed later in this section.

If we call the number of events in the 1991 data with only the CENTRL trigger fired A, the number with CENTRL and FDHIOR fired B, and the number with only FDHIOR fired C, then the respective efficiencies are calculated from the numbers in fig 4.5 and are given in table 4.7.

The variation of the 1991 total efficiency and the CENTRL(1990) efficiency is shown as a function of x_{vis} in figure 4.6. As both efficiencies are consistent with being flat, no x-dependent correction to the efficiency is made.

Checks were made to test the assumption that the 1990 CENTRL efficiency was the same as in 1991. Even though the triggers forming this logical .OR. are

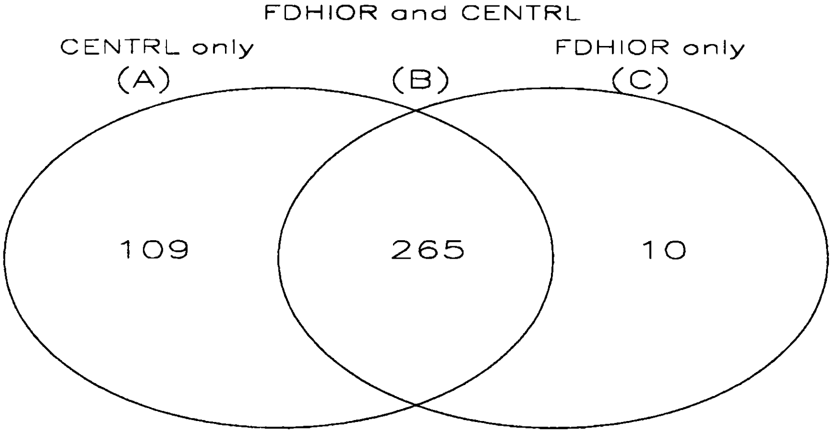

Figure 4.5: Venn diagram showing events which fall into categories A,B,C for 1991 data.

	Equation	Efficiency(%)
CENTRL (1990)	$\frac{B}{B+C}$	96.4 ± 1.1
FDHIOR	$\frac{B}{B+A}$	70.8 ± 2.1
1991 Total	$1-\left(1-\frac{B}{B+C})(1-\frac{B}{B+A}\right)$	98.9 ± 0.4
Total	$596/\left(\frac{384}{0.989}+\frac{212}{0.964}\right)$	98.0 ± 0.7

Table 4.7: Measured and estimated trigger efficiencies. There are 384 events from 1991 and 212 from 1990 data taking. The CENTRL efficiency is also the 1990 estimated efficiency.

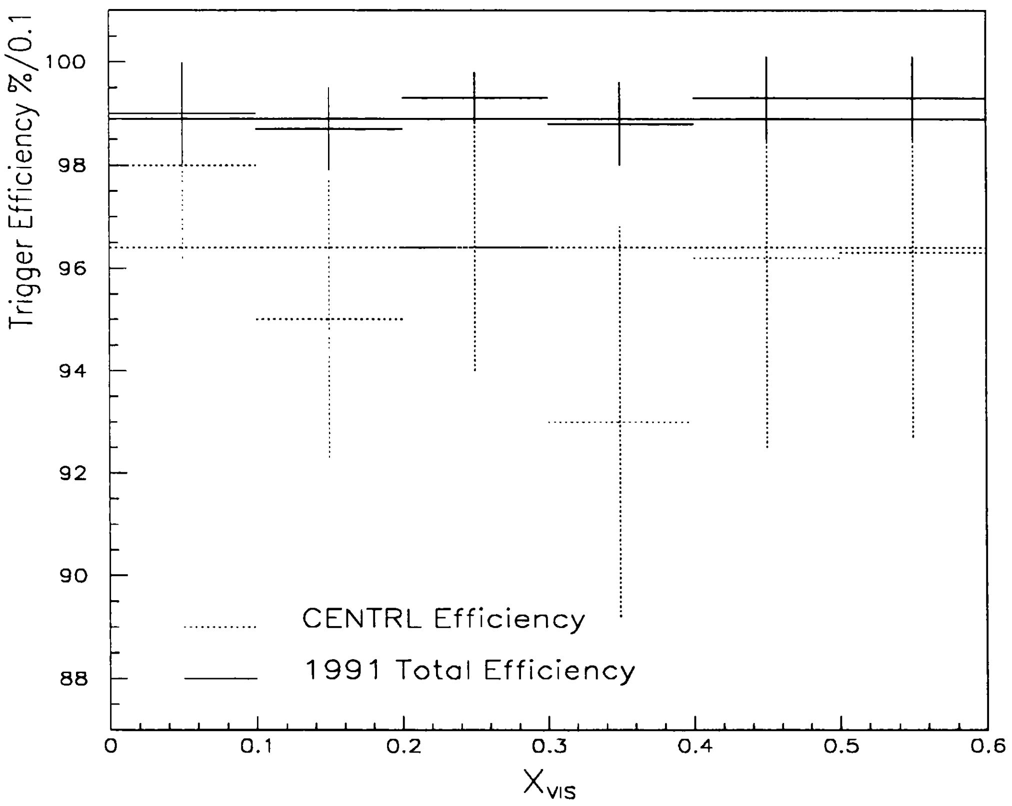

Figure 4.6: Trigger Efficiency against x_{vis}. The trigger efficiencies given in table 4.7 are drawn as lines on the plot.

not truly independent for our sample the "efficiencies" of the triggers can be measured in the same way as in equation 4.1. The results for the two samples are compared in table 4.3.2 and are in broad agreement. Thus we assume that the 1990 efficiency is indeed 96.4 ± 1.1%.

Efficiency of		"Measured by" (%)				
Trigger	year	TBM1	TPTTEM	TPTTTO	TPTOEM	EETPHI
TBM1	1991	X	85.4±2.4	94.2±1.3	95.1±1.8	66.0±6.1
	1990	X	84.9±3.5	92.7±1.8	93.5±2.7	60.0±14.4
TPTTEM	1991	49.7±2.8	X	85.4±2.4	81.3±3.0	82.0±5.0
	1990	42.2±4.0	X	92.4±2.7	84.4±3.8	80.0±11.7
TPTTTO	1991	93.9±1.3	49.8±2.8	X	97.2±1.4	58.0±6.6
	1990	95.6±1.5	44.5±3.8	X	97.4±1.8	60.0±14.4
TPTOEM	1991	41.5±3.0	60.9±3.3	42.6±3.0	X	40.0±7.9
	1990	38.9±4.2	70.7±4.3	39.3±2.7	X	50.0±15.8
EETPHI	1991	10.0±4.7	21.3±5.2	8.8±4.8	13.9±6.7	X
	1990	3.3±7.0	8.7±9.2	3.2± 6.9	6.5±10.3	X

Table 4.8: Comparison of some of the triggers which make up the CENTRL trigger in 1991 and 1990. EETPHI ≡ EERTPH.OR.EELTPH

4.3.3 Trigger Efficiency from Monte Carlo Simulation

The Monte Carlo used to simulate the OPAL detector [43], has a passive trigger simulation (ie the result is simulated, but it is not acted upon) built into it. The efficiency of the CENTRL trigger for the various Monte Carlos is shown in table 4.9. Obviously there is a discrepancy between the Monte Carlo simulation of the trigger efficiency and the data measured efficiency. This is most probably due to the real detector having faults which have not been included in the Monte Carlo.

Monte Carlo	Efficiency (%)
QCD	100
VMD Pointlike	100
VMD peripheral	99.8
$c\bar{c}$	100
$\tau^+\tau^-$	100
total	100.0

Table 4.9: Various Monte Carlo trigger efficiencies, which are calculated by comparing the number of events which pass the final selection cuts with the subset of those events which has fired the CENTRL trigger. The FDHIOR trigger has not been simulated.

As the Monte Carlo simulation is passive no error on the unfolded structure function is assigned because of the discrepancy. The systematic error due to variation of cuts is considered in section 7.2.1 and this will contain an element due to bad Monte Carlo simulation of the OPAL detector.

4.4 Data Self Consistency

In this analysis data is taken from two years - 1990 and 1991 - and compared to check that the data is self-consistent and understood. The number of events, luminosities and trigger efficiency corrected number of events for each year are given in table 4.4. The errors on the two luminosities are taken from [39, 44]. The number of 1991 events normalized to the 1990 luminosity is also given and it can be see that the two samples agree very well.

Year (A.D.)	No. of Events	Luminosity (pb^{-1})	Corrected No. of Events	Norm. to 1990 Lumi.
1990	212	6.67 ± 0.05	219.9	-
1991	384	11.76 ± 0.08	388.3	220.2
Total	596	18.43 ± 0.13	608.2	-

Table 4.10: Comparison of number of events and integrated luminosities in 1990 and 1991. The corrected number includes the trigger efficiency correction.

Various distributions from each year are shown in figures 4.7, 4.8, 4.9 and 4.10. In every plot the 1991 data is shown in the solid histogram, normalized to the 1990 luminosity, and the 1990 data is plotted as the dashed histogram. Each distribution is plotted with all the analysis cuts applied except cuts on the quantity being plotted. In that case the arrows represent the cuts on that quantity.

In figure 4.7 we can see various distributions concerned with the tag. The normalized tag energy distributions agree very well. The feature near 50 mrad in figure 4.7(b) is a known coordinate distortion which is also modelled in the Monte Carlo. This leads to the local fluctuation of events at low Q^2(figure 4.7(d)) in 1990, but the perturbation is sufficiently local that the physics should not be affected. Figure 4.7(c) shows that the calorimeter calibration is consistent between the two years.

The p_T distributions shown in figure 4.8 are reasonably compatible. ${p_T}^{IN}$ (figure 4.8(a)) is the summed p_T in the plane of the tag and the beam, with the additional K, V indicating charged tracks only or charged tracks and electromagnetic cluster information respectively being used. The p_T of the tag is defined as positive, which explains the offset from 0 seen in figure 4.8(a). The summed p_T out of the tag plane is plotted in figures 4.8(b) and (d) with the symbols

K, V having the same meaning as above. These plots indicate that the hadronic acceptance is roughly the same in both years.

In figures 4.9(a) and (d) the neutral energy (ie total electromagnetic energy not associated with tracks) and neutral multiplicity are plotted. There are some signs that there is less energy in 1990 (coupled with a smaller multiplicity) but this does not lead to a significant discrepancy in the x_{vis} distribution (figure 4.10(d)). The energy of the highest energy cluster in the hemisphere opposite the tag is plotted in figure 4.9(b).

The W and x distributions are shown in figure 4.10 and they agree well.

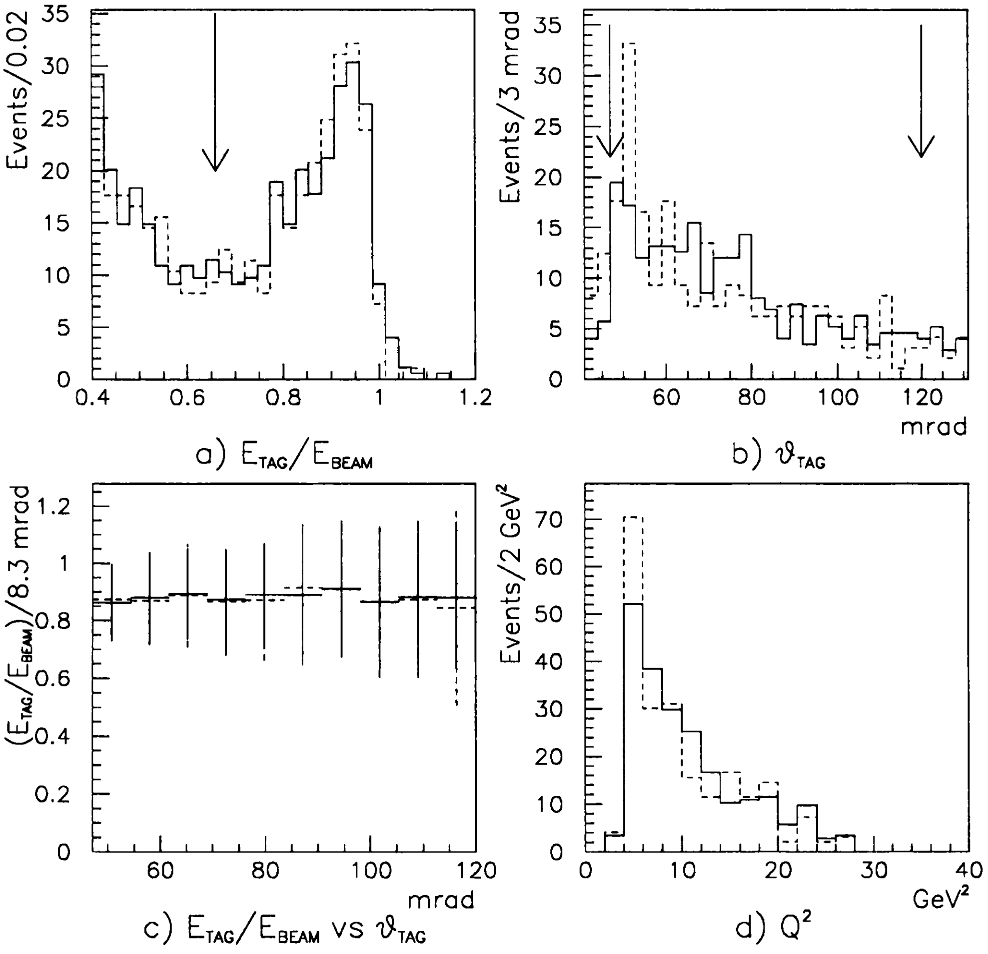

Figure 4.7: Comparison of 1990 and 1991 tag distributions.

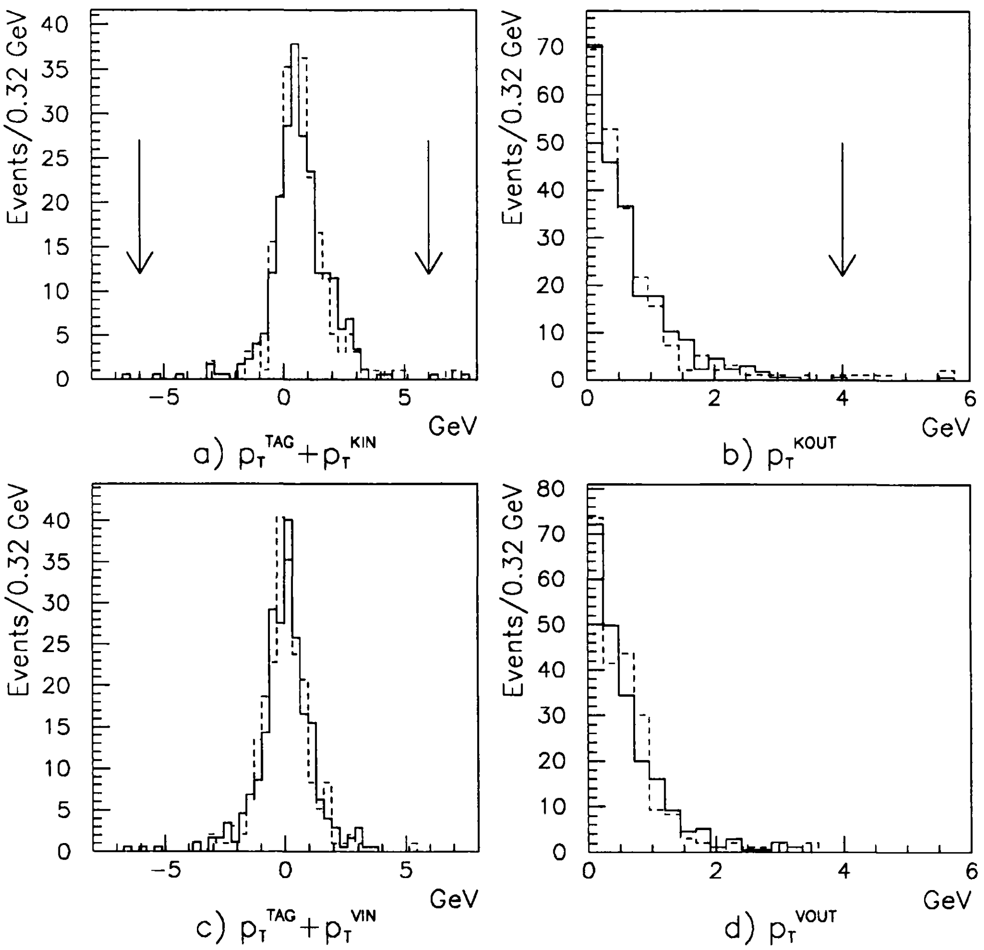

Figure 4.8: Comparison of 1990 and 1991 p_T distributions.

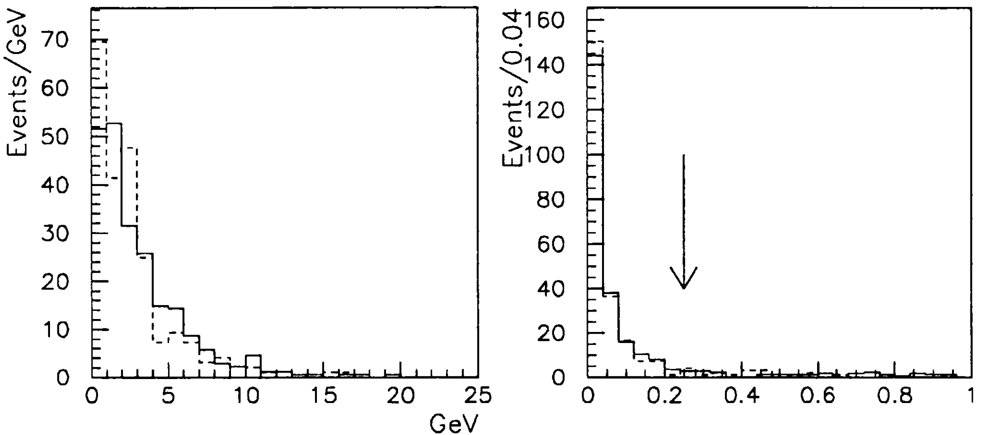

a) Neutral energy

b) $E_{Antitag}/E_{BEAM}$

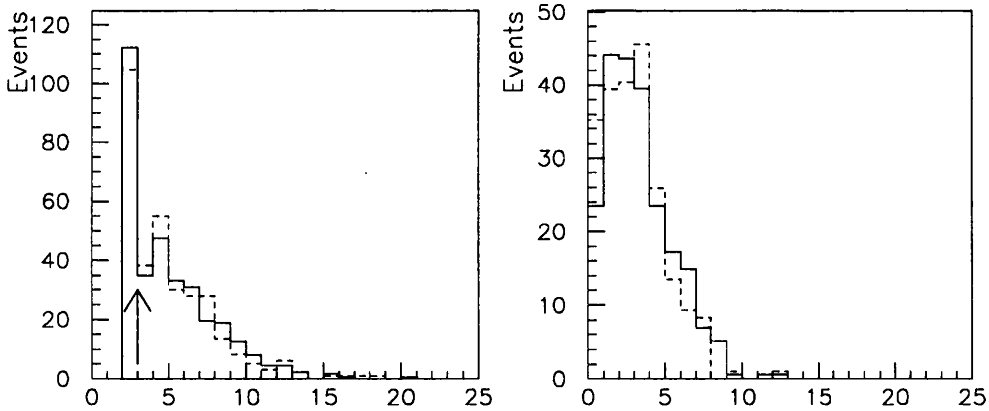

c) Charged track multiplicity

d) Neutral multiplicity

Figure 4.9: Comparison of 1990 and 1991 raw distributions

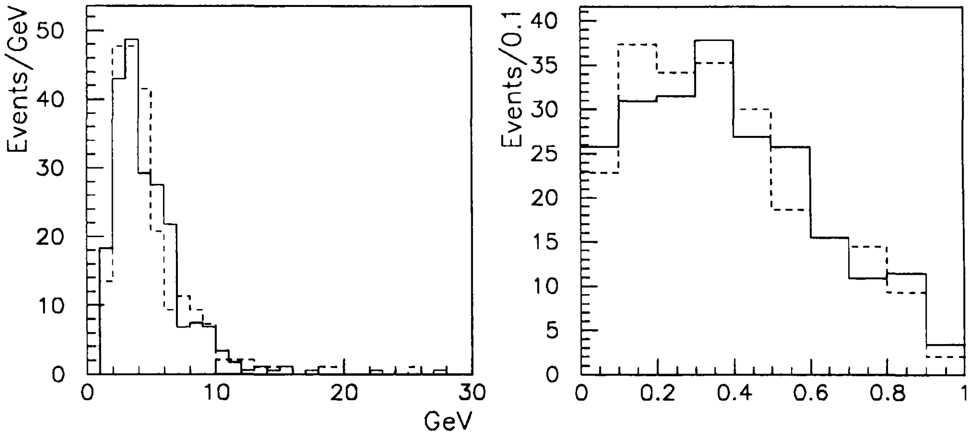

a) W_{TRACK} b) X_{TRACK}

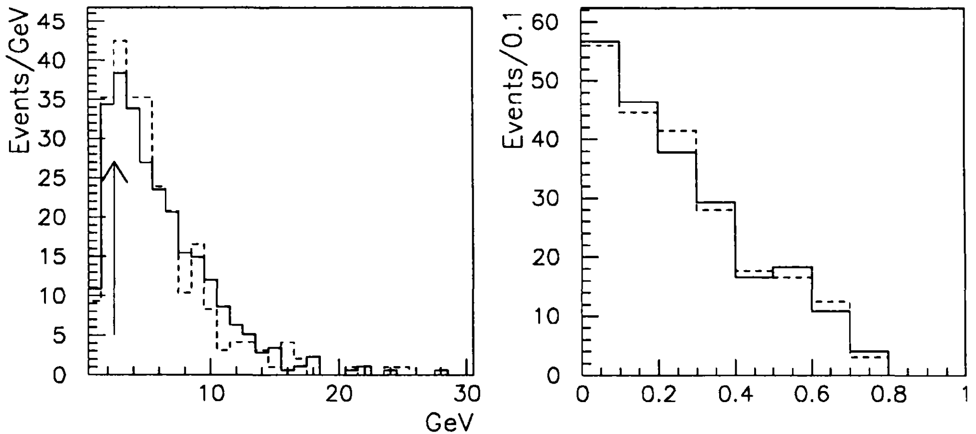

c) W_{VIS} d) X_{VIS}

Figure 4.10: Comparison of 1990 and 1991 physics distributions.

Chapter 5

Monte Carlo Simulation

Two Monte Carlo programs are used to generate events which are used both in the unfolding of our data and to compare with various measured variables from our data. These are a QED matrix-element Monte Carlo program written by Vermaseren [45, 46, 47] (which shall be referred to as the "Vermaseren" generator) and F2GEN [48], a new Monte Carlo program which generates events according to chosen formulae for $F_2(x, Q^2)$. These both generate four fermion (two electrons and a quark-antiquark (or tau-tau) fermion pair) final states which are allowed to fragment by using the LUND string model [49, 50] as implemented in the JETSET Monte Carlo(version 6.3). These fragmented events are then passed through the OPAL detector simulation Monte Carlo GOPAL [43], and then exactly the same analysis program is run on them as is run on the real data (see chapter 4). Further details of these two generators are described in the next two sections.

5.1 Vermaseren

This is a QED matrix element Monte Carlo program based on an exact calculations of figures 5.1(a) and (b). It includes suitable quark masses, charges and colours in order to run as a quark parton model (QPM) generator.

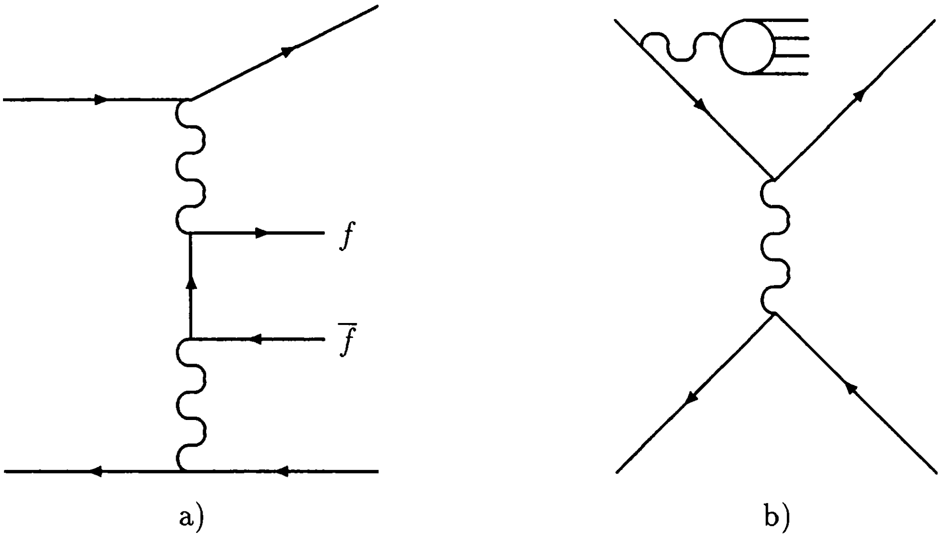

Figure 5.1: Diagrams for $e^+e^- \rightarrow e^+e^-$ + *hadrons* calculated by the Vermaseren generator.

5.2 F2GEN

A new Monte Carlo program F2GEN has been developed to generate events according to chosen formulae for $F_2(x, Q^2)$. It is adapted from TWOGEN which is based on the transverse-transverse two-photon luminosity generator developed by Langeveld [51] for analysis of two-photon data from the TPC/2γ experiment. The total cross section, given in 3.1, is approximated using only the transverse-transverse (σ_{TT}) term with σ_{TT} given in terms of $\mathrm{F}_2(x, Q^2, P^2)$ as:

$$\sigma_{TT} = \frac{4\pi^2\alpha}{Q^2}\mathrm{F}_2(x, Q^2, P^2) \tag{5.1}$$

The electron, positron and two photons are generated first using the luminosity generator. If the event passes certain cuts (minimum and maximum tag angle, minimum tag energy and minimum center-of-mass energy of the two-photon system W) a quark-antiquark state is generated, with mass W and a pointlike (QPM) angular distribution in the two-photon centre of mass. The quark flavour is chosen by a $(charge)^4$ weighting.

As a check, F2GEN has been compared with the predictions of Vermaseren.

5.3 Monte Carlo Samples

In generating samples for comparison with the data it is necessary to combine a number of contributions:

QCD

There are numerous formulae for F_2 on the market which could be used in F2GEN. The "all order QCD" approach of Kapusta [33] has been chosen, as parametrised in a recent AMY paper [12],

$$\begin{aligned} \mathrm{F}_2(x,Q^2) &= \frac{3\alpha}{\pi}\sum_q e_q^4\, x \left\{ 6x(1-x) + \frac{2m_q^2}{t_c}x - 1 \right. \\ &\quad \left. + \frac{a(x)}{x^C + C\, f(x)} Y_{max}\left[1 - \left(\frac{Y_c}{Y_{max}}\right)^{1+Cf(x)}\right]\right\}, \end{aligned} \tag{5.2}$$

where $a(x)$, $f(x)$, C, Y_{max} and Y_c are defined as,

$$a(x) = x^2 + (1-x)^2, \tag{5.3}$$

$$f(x) = 2\ln\frac{1}{1-x} - x - \frac{1}{2}x^2, \tag{5.4}$$

$$C = \frac{8}{33 - 2N_f}, \tag{5.5}$$

$$Y_{max} = \ln\left(\frac{Q^2}{x\Lambda^2_{\overline{MS}}}\right), \tag{5.6}$$

$$Y_c = \ln\left(\frac{t_c}{\Lambda^2}\right). \tag{5.7}$$

For the entire x region,

$$t_c = [m_q^2 + (p_t^0)^2]/(1-x). \tag{5.8}$$

The change in the behaviour of the structure function at Q^2 close to 1 GeV^2 [52, 53, 54, 55] is built into this model by setting a cutoff in p_t, the transverse momentum of the virtual quark at the target photon vertex. The pointlike behaviour of the QCD formula is assumed to apply to all $p_t > p_t^0$, but a separate part must be added to the cross section to allow for the hadron-like behaviour of the target photon for $p_t < p_t^0$. This extra contribution is assumed to be parametrised by the Vector Meson Dominance model (see section 3.2.1). $\Lambda_{\overline{MS}}$ was set to 200 MeV.

VMD

The Vector Meson Dominance contribution uses the F2GEN Monte Carlo with the structure function formula

$$\mathrm{F}_2(x)/\alpha = Ax^a(1-x)^{0.95} + B(1-x)^b, \tag{5.9}$$

with $A = 0.22, B = 0.06, a = 0.31, b = 2.5$, motivated by studies of the pion structure function [14]. This has been shown by the TPC/2γ experiment [6] to be a reasonable approximation to the observed distributions at low Q^2.

A quark-antiquark pair is generated in a similar way to the QCD events. In previous analyses the angular distribution of the quarks in the $\gamma\gamma$ centre of mass has been taken to be a mixture of either pointlike, with a QPM type scattering, or peripheral with limited transverse momentum in the two-photon centre of mass (average $p_T = 300$ MeV. This scale is chosen to represent the average p_T of a quark in a meson). The total amount of the VMD contribution is kept constant but the data is fitted by varying the number f_{point} where f_{point} is the weight given to the generated pointlike VMD events, and $1 - f_{point}$ is the weight given to the generated peripheral VMD events.

QPM

Charmed quark ($e^+e^- \rightarrow e^+e^- + c\bar{c}$) and tau lepton ($e^+e^- \rightarrow e^+e^- + \tau^+\tau^-$) events are generated with the Vermaseren Monte Carlo., i.e. assuming that the heavy quark behaves according to QPM at these modest Q^2 values, and that the tau lepton behaves according to QED. These contributions are referred to as $c\bar{c}$ and $\tau^+\tau^-$ throughout this thesis. QPM events are also generated in order to compare Vermaseren and F2GEN. This comparison is discussed below.

5.4 Comparison of F2GEN and Vermaseren

In order to be sure that the F2GEN generator gives the proper normalization and distributions we have compared it with the Vermaseren generator. In the comparison F2GEN has been run with both a P^2 dependent formula for F_2 in the quark parton model (QPM) [56],

$$\begin{aligned} \mathrm{F}_2(x,Q^2,P^2) &= \frac{3\alpha(\sum_i e_i^4)\,x}{\pi}\left[(x^2+(1-x)^2)\ln\left(\frac{Q^2(\frac{1-x}{x})}{(m_q^2+P^2x(1-x))}\right)\right. \\ &\left. -\,2(1-3x+3x^2)+\frac{m_q^2(1+2x-2x^2)}{(m_q^2-P^2(x^2-x))}\right] \end{aligned} \tag{5.10}$$

and with a P^2 independent QPM formula for F_2 [15],

$$\mathrm{F}_2(x,Q^2) = \frac{3\alpha(\sum_i e_i^4)\,x}{\pi}\left[(x^2+(1-x)^2)\ln\left(\frac{Q^2}{m_q^2}(\frac{1-x}{x})\right)+8x(1-x)-1\right], \tag{5.11}$$

where m_q is the relevant quark mass ($\sim$ 0.35 GeV for light (uds) quarks).

100,000 events were generated with Vermaseren (running in QPM mode producing $u\overline{u}$ events) and 200,000 with F2GEN (100,000 P^2 dependent and 100,000 P^2 independent) with some loose cuts (a tag of $E_{TAG} > 20$ GeVis demanded between $40 < \theta_{TAG} < 130$ mrad). The beam energy in both cases was 45.6 GeV. To ensure that both generators were accessing the same phase space (which is similar to that accessed in our final sample of events) tighter cuts were applied to the generated samples, namely:-

a) $E_{TAG} > 0.7 * E_{BEAM}$: E_{TAG} is the energy of the tag.

b) NTRK > 2 : NTRK is the number of final state charged particles (not including the final state electrons)

c) $W_{vis} > 2.5$: W_{vis} is the invariant mass of all the particles (charged and neutral).

d) $0.47 < \theta_{TAG} < 0.120$: θ_{TAG} is the angle of the tag.

e) Restrict F2GEN to $u\overline{u}$ events

The cross section results are presented in table 5.1. N_{Gen} is the number of events generated with a cross section σ_{Gen} to give 100,000 events satisfying loose cuts, and N_{Cuts} is the number of events that result from applying the above listed, tighter cuts. The cross section σ_{Cuts} is derived from the formula:

$$\sigma_{Cuts} = \sigma_{Gen} \times \frac{N_{Cuts}}{N_{Gen}}$$

Sample	N_{Gen}	σ_{Gen} (pb)	N_{Cuts}	σ_{Cuts} (pb)
Vermaseren	2,058,790	1805.238	41998	36.83
F2GEN $F_2(x, Q^2, P^2)$	125,466	121.79	37433	36.33

Table 5.1: Comparing F2GEN and Vermaseren outputs.

In overall cross section, the generators differ by $1.4 \pm 0.7\%$ where the error is statistical only. F2GEN was run 10 times producing 10,000 P^2 independent events each time. The resulting scatter of cross sections had $\sigma = 1.6\%$ which, if we assume it is made up of the statistical error (1%) and a systematic error added in quadrature, leads to an estimate of the systematic error of 1.3% for the F2GEN generator. Assigning this 1.3% as a systematic error due to the technical precision of the F2GEN Monte Carlo, means that Vermaseren and F2GEN agree to within the combined statistical and systematic error of 1.5%. Another correction applied is a kinematic correction to take into account the difference between a P^2 dependent F_2 and a P^2 independent F_2. A further cut must be applied to limit the events to single tagging. This is applied to the final state electron or positron which is not selected as the tag (thus the subscript *antitag*) and mimics the antitagging cut discussed in section 4.1.3.

f) $\theta_{antitag} < 0.04$ radians .OR. $E_{antitag} < 0.25 * E_{BEAM}$.

The cross sections are compared in table 5.2. The normalization difference is:

Sample	N_{Gen}	σ_{Gen} (pb)	N_{Cuts}	σ_{Cuts} (pb)
F2GEN $F_2(x, Q^2, P^2)$	125,466	121.79	37433	34.42
F2GEN $F_2(x, Q^2)$	124389	137.07	38007	36.31

Table 5.2: Comparing F2GEN P^2 dependent and P^2 independent QPM outputs.

$$\frac{F_2(x, Q^2)_{QPM}}{F_2(x, Q^2, P^2)_{QPM}} = \frac{34.42}{36.31} = 0.95$$

and this is applied as a correction to the QCD component of the Monte Carlo (see section 5.4). This is not applied to the VMD component of our Monte Carlo sample since:

- it is not clear that a QPM based correction has any validity in this case.
- The precise normalization of this VMD sample is uncertain to much more than the possible correction.

We must also ask if there is any shape difference between the distributions from the generators, particularly in x_{true}. The Q^2 distributions are compared in figures 5.2(a) and (b). As the data have been split into two Q^2 regions (see section 6.2) the generators have also been compared in these two Q^2bands. The x_{true} histograms comparing Vermaseren and F2GEN(P^2 dependent QPM) in the two Q^2 regions are shown in figure 5.3. The agreement between the histograms in terms of χ^2 are given in table 5.3. Similarly the x_{true} histograms for F2GEN(P^2 dependent QPM) and F2GEN(P^2 independent QPM) are shown, with the antitag cut (f) described above applied, in figure 5.4, with the relevant χ^2 again given in table 5.3.

In both Q^2 ranges, and for both the Vermaseren/F2GEN(P^2 dependent QPM) and the F2GEN(P^2 dependent)/F2GEN(P^2 independent) comparisons, the χ^2 are acceptable. The precise agreement between Vermaseren and F2GEN(P^2 de-

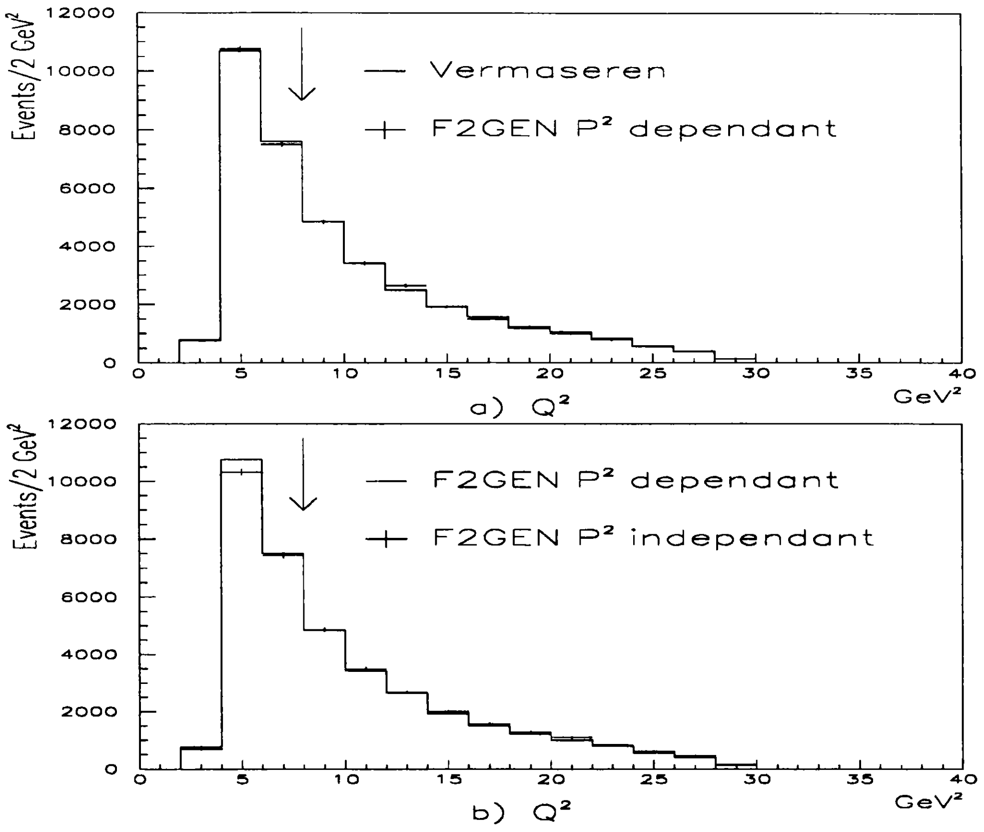

Figure 5.2: The Q^2 distributions from the generators a) Vermaseren and F2GEN(P^2 dependent QPM), and b) F2GEN(P^2 dependent QPM) and F2GEN(P^2 independent QPM).

Q^2band	$Q^2 < 8$ (GeV/c)^2		$Q^2 \geq 8$ (GeV/c)^2	
Figure	5.3(a)	5.4(a)	5.3(b)	5.4(b)
χ^2/dof	10.6 / 6	6.9 / 6	12.2 / 8	3.4 / 8
Corrected χ^2/dof	-	1.7 / 4	-	1.3 / 6

Table 5.3: The χ^2 for various figures. The corrected χ^2 is achieved by applying a linear correction to the Monte Carlo generated with F2GEN using a P^2 dependent F$_2$.

pendent) is not critical since the process of unfolding the data should give a result independent of the exact input Monte Carlo shape. However as a correction is applied to the QCD events, based on the difference between the P^2 dependent and independent versions of the F2GEN QPM generated events, any x dependent variation must also be included. The difference between the two F2GEN QPM histograms divided by the $F_2(x, Q^2, P^2)_{QPM}$ histogram is plotted in figure 5.5. A straight line is fitted, and the resulting linear correction is applied to the $F_2(x, Q^2)_{QPM}$ histogram. A corrected χ^2 is calculated and given in table 5.3. As can be seen the correction is small but it is applied to the final unfolded $F_2(x, Q^2)$.

In conclusion Vermaseren and F2GEN are consistent to within the estimated error of 1.5%. A correction to the QCD events has to be applied to take account of the P^2 dependence of F_2. This is mainly a normalization correction, but does have a small x dependence.

5.5 Initial State Radiation

Neither the Vermaseren or F2GEN generators includes initial state radiation diagrams in their calculations. The effect of this has been estimated in [13] using the FERMISV [41] generator. The effect is estimated to reduce the cross section of the multiperipheral diagram in 5.1 by 2.7 ± 1.8%. This correction is applied and the 1.8% assigned as a systematic error in the final unfolding.

5.6 Monte Carlo Samples Generated

Details of the various Monte Carlo samples generated for use in this comparison, and in the unfolding (see chapter 7) are given in table 5.4. There are several points to note concerning this table:

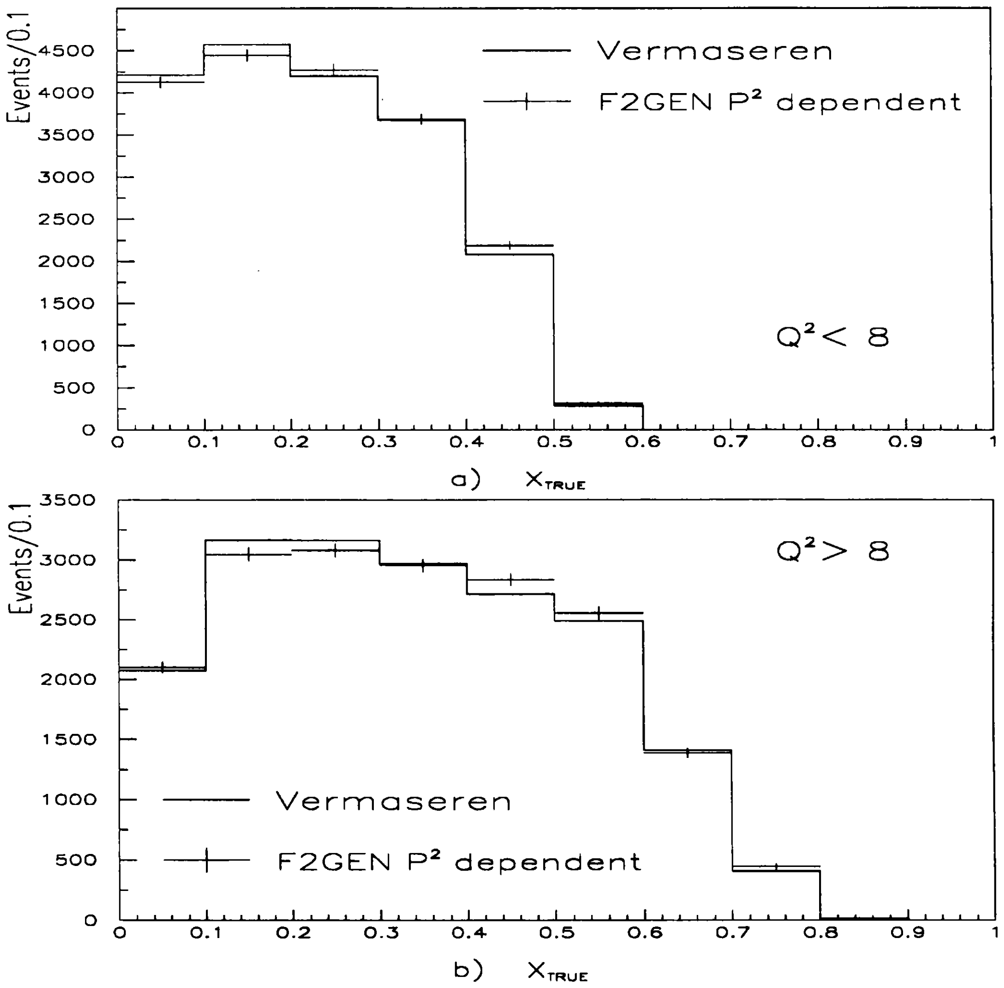

Figure 5.3: The x_{true} distributions from the generators a) Vermaseren and F2GEN(P^2 dependent QPM) compared in the Q^2 ranges a) $4 < Q^2 < 8$ GeV^2 and b) $8 < Q^2 < 30$ GeV^2.

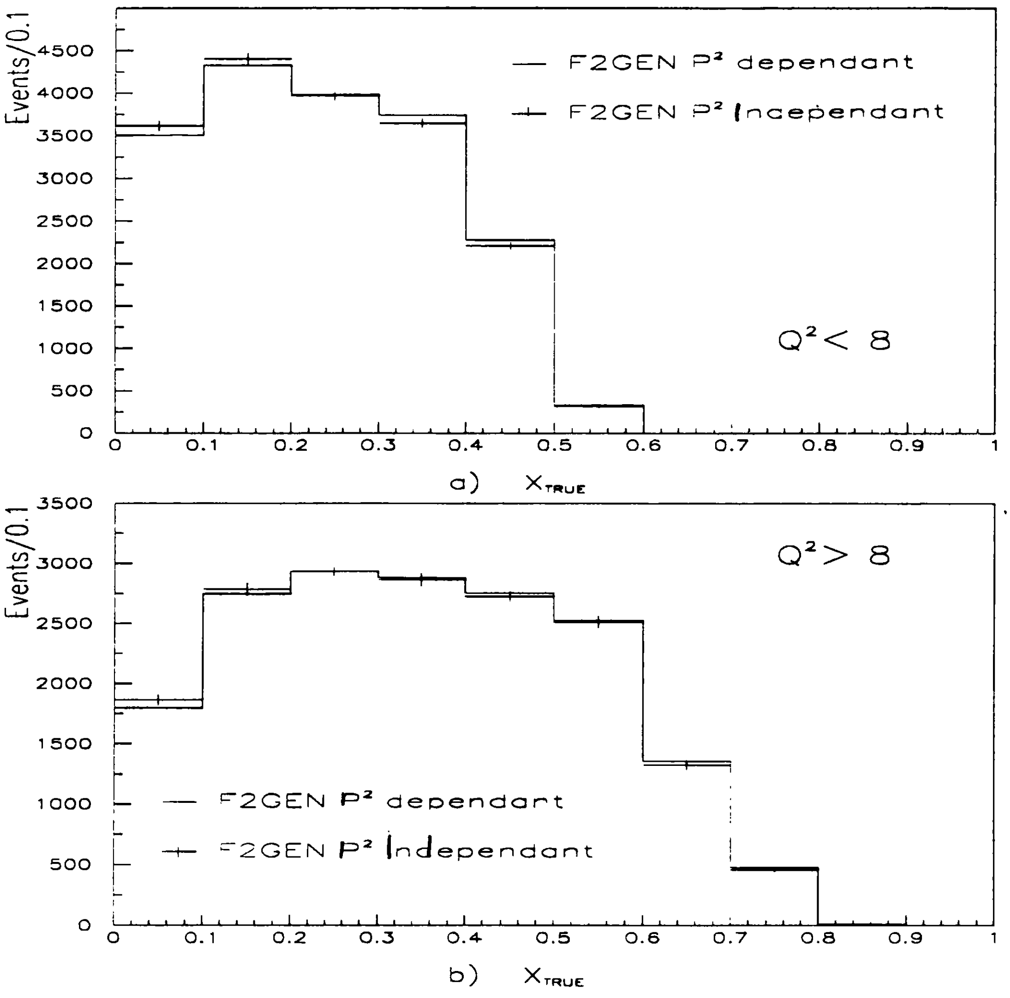

Figure 5.4: The x_{true} distributions from the F2GEN generator with P^2 dependent and independent QPM parameterizations compared in the Q^2 range a) $4 < Q^2 < 8$ GeV^2 and b) $8 < Q^2 < 30$ GeV^2.

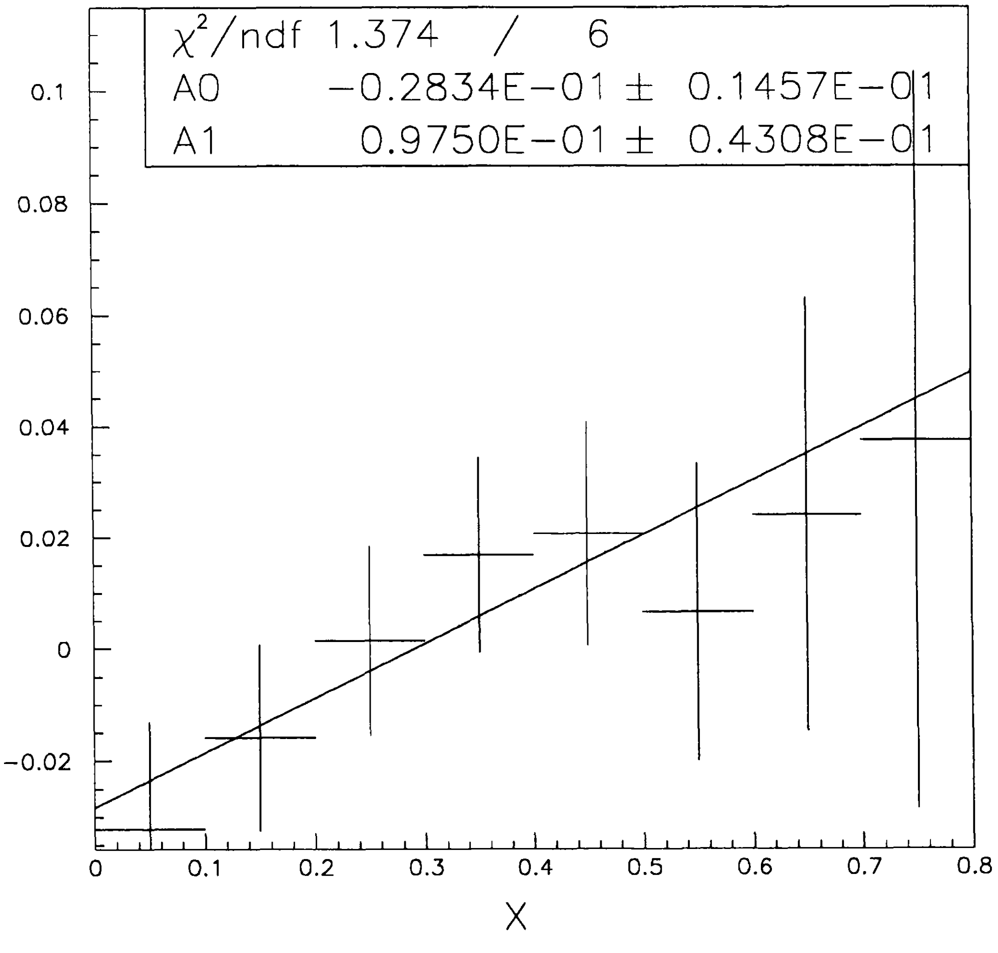

Figure 5.5: x dependent shape of the P^2 correction. This is the difference between the F2GEN P^2 dependent and P^2 independent histograms (after the 5% normalization correction has been applied) divided by the F2GEN P^2 dependent one.

- The number of generated events corresponds to the number that pass the loose generator cuts described in section 5.5 above.
- All the events have been passed though GOPAL. The number of events passing the full selection described in chapter 4 are given in table 5.5 (596 data events passed these cuts).
- The $0.2(1-x)$ row under the VMD heading was generated with peripheral distribution described in section 5.4 above.
- The VMD pointlike and peripheral cross sections should be exactly the same. The difference of 0.3% is purely due to F2GEN systematics and is within the assigned systematic error of 1.3%.
- The event weight is just the data integrated luminosity (18.43pb^{-1}) divided by the integrated luminosity for the relevant Monte Carlo.
- The cross sections have not been corrected for P^2 dependence or initial state radiation. The numbers given in the corrected weight column include both these corrections and are used to produce the normalized numbers of events given in table 5.5.

The data is compared with the Monte Carlo sum
QCD $+f_{point}$(VMD pointlike) $+(1-f_{point})$(VMD peripheral) $+c\bar{c}+\tau^+\tau^-$
in the next chapter.

Sample	Generated No. Events	σ_{Gen} (pb)	Integrated Lumi (pb^{-1})	Event weight	Corrected weight
F2GEN					
QCD					
$p_t^0 = 0.2$	20,000	150.96	132.49	0.139	0.128
$p_t^0 = 0.3$	10,000	141.84	70.50	0.261	0.240
$p_t^0 = 0.5$	10,000	125.06	79.96	0.230	0.212
VMD					
peripheral	10,000	103.15	96.95	0.190	0.185
pointlike	4,000	102.84	38.90	0.474	0.462
$0.2(1-x)$	10,000	125.63	79.60	0.232	0.226
Vermaseren					
$c\bar{c}$	3,000	158.07	165.06	0.112	0.109
$\tau^+\tau^-$	4,000	272.99	135.41	0.136	0.132

Table 5.4: Generated samples of Monte Carlo. See notes in the text for further discussion.

Sample	Events passing final cuts	Normalized to 18.43pb^{-1}
QCD $p_t^0 = 0.2$	3058	391.4
QCD $p_t^0 = 0.3$	1539	369.4
QCD $p_t^0 = 0.5$	1546	327.8
VMD peripheral	767	141.9
VMD pointlike	608	280.9
VMD $0.2(1-x)$	711	160.7
$c\bar{c}$	762	83.1
$\tau^+\tau^-$	218	28.8

Table 5.5: Monte Carlo events passing the full analysis cuts

Chapter 6

Comparing the Data with the Monte Carlo

The free parameters f_{point} and p_t^0 discussed in chapter 5, are estimated from the data. The data is compared in two Q^2 bands with the Monte Carlo sum of

$$\mathrm{QCD} + \mathrm{VMD} + c\bar{c} + \tau^+\tau^-$$

6.1 Estimating p_t^0 and f_{point}

The method used is that of χ^2 minimization in which there are two free parameters; f_{point} and p_t^0. Varying the weights of the QCD events (W_{qcd}) given in table 5.4 is similar to varying p_t^0 in that a change in p_t^0 changes mostly the normalization and does not have a large effect on the shape of most distributions - see figure 6.1 where the samples have been normalized to the same number of events. W_{qcd} (or p_t^0) is a less important parameter to extract from the data at this stage as the unfolding process (see chapter 7) should be insensitive to the precise p_t^0 used in the QCD Monte Carlo generation. However as both the VMD samples (peripheral and pointlike) are generated with the same $\mathrm{F}_2(x)$ the unfolding must

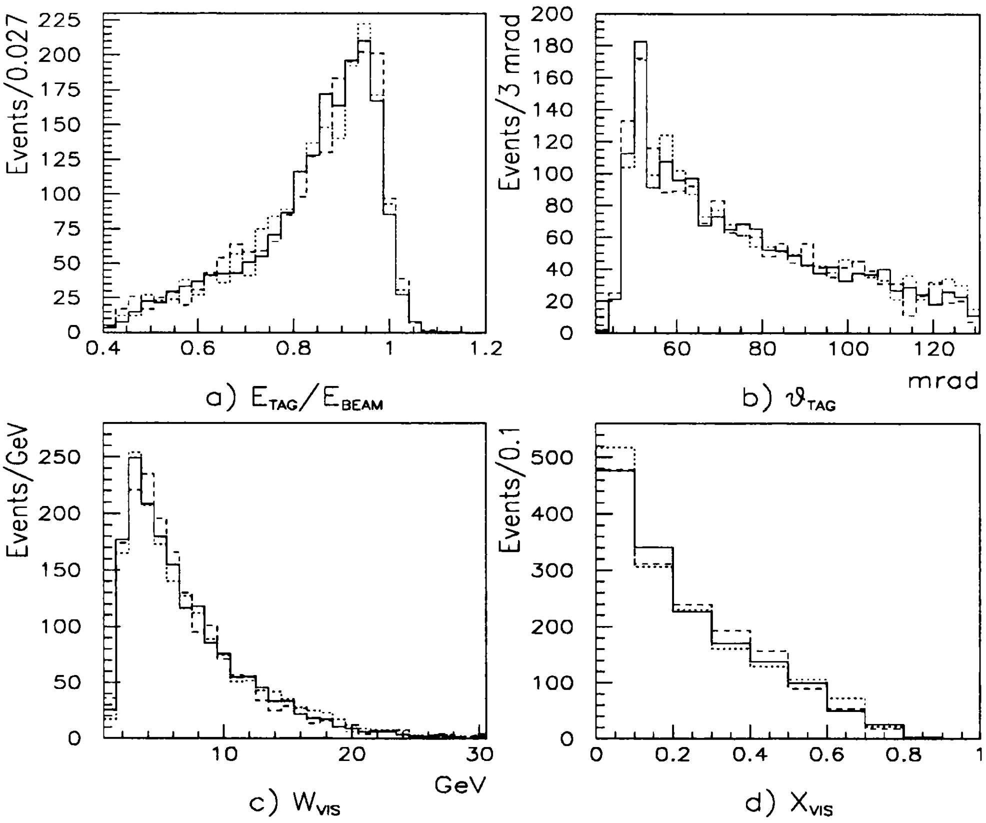

Figure 6.1: Comparison of QCD Monte Carlos generated with different values of p_t^0. The solid line was generated with $p_t^0 = 0.2$, the dashed with $p_t^0 = 0.3$ and the dotted with $p_t^0 = 0.5$

take f_{point} as an input parameter.

This technique is described and then the fits are performed.

6.1.1 χ^2 Minimization

If we are fitting a distribution which has $d_i, q_i, V_i^{prf}, V_i^{pnt}, c_i, t_i$ events in the ith bin of the data (with background subtracted), the Monte Carlo QCD, the normalized Monte Carlo VMD peripheral, VMD pointlike, $c\bar{c}$ and $\tau^+\tau^-$ distributions respectively then the quantity that is minimized is

$$\chi^2 = \sum_i \left(\frac{d_i - c_i - t_i - f_{point} V_i^{dif} - V_i^{prf} - W_{qcd} q_i}{\sigma_{d_i}} \right)^2 \tag{6.1}$$

where W_{qcd} is the QCD monte carlo weight. If we wish to fit to p_t^0 then W_{qcd} becomes a function of i and p_t^0 $W_i^{qcd}(p_t^0)$. Now we minimize χ^2 with respect to f_{point} and W_{qcd}:

$$\frac{\partial \chi^2}{\partial f_{point}} = \sum_i \frac{-V_i^{dif}(D_i - f_{point} V_i^{dif} - W_{qcd} q_i)}{\sigma_{d_i}^2} = 0 \tag{6.2}$$

$$\frac{\partial \chi^2}{\partial W_{qcd}} = \sum_i \frac{-q_i(D_i - f_{point} V_i^{dif} - W_{qcd} q_i)}{\sigma_{d_i}^2} = 0 \tag{6.3}$$

where $V_i^{dif} = V_i^{pnt} - V_i^{prf}$ and $D_i = d_i - c_i - t_i - V_i^{prf}$. From these two equations we get the matrix equation:

$$\sum_i \frac{1}{\sigma_i^2} \begin{pmatrix} (V_i^{dif})^2 & q_i V_i^{dif} \\ q_i V_i^{dif} & q_i^2 \end{pmatrix} \begin{pmatrix} f_{point} \\ W_{qcd} \end{pmatrix} = \sum_i \frac{1}{\sigma_i^2} \begin{pmatrix} V_i^{dif} D_i \\ q_i D_i \end{pmatrix} \tag{6.4}$$

For the error on our results we evaluate $\frac{1}{2}\frac{\partial^2 \chi^2}{\partial p_i \partial p_j}$ where p_i are the parameters we are fitting to. In this case:

$$\frac{1}{2}\frac{\partial^2 \chi^2}{\partial {f_{point}}^2} = \sum_i \frac{(V_i^{dif})^2}{\sigma_{d_i}^2} \tag{6.5}$$

$$\frac{1}{2}\frac{\partial^2 \chi^2}{\partial W_{qcd}^2} = \sum_i \frac{q_i^2}{\sigma_{d_i}^2} \tag{6.6}$$

$$\frac{1}{2}\frac{\partial^2 \chi^2}{\partial f_{point} \partial W_{qcd}} = \sum_i \frac{V_i^{dif} q_i}{\sigma_{d_i}^2} \tag{6.7}$$

The inverse error matrix is then:

$$\begin{pmatrix} \sum_i \frac{(V^{dif})_i^2}{\sigma_{d_i}^2} & \sum_i \frac{V_i^{dif} q_i}{\sigma_{d_i}^2} \\ \sum_i \frac{V_i^{dif} q_i}{\sigma_{d_i}^2} & \sum_i \frac{q_i^2}{\sigma_{d_i}^2} \end{pmatrix} \tag{6.8}$$

If this matrix is inverted, then the leading diagonal contains the square of the errors on f_{point} and W_{qcd}. The correlations are contained in the off diagonal elements and will certainly not be negligible. If f_{point} is increased towards 1 then W_{qcd} will decrease in order to preserve the overall normalization.

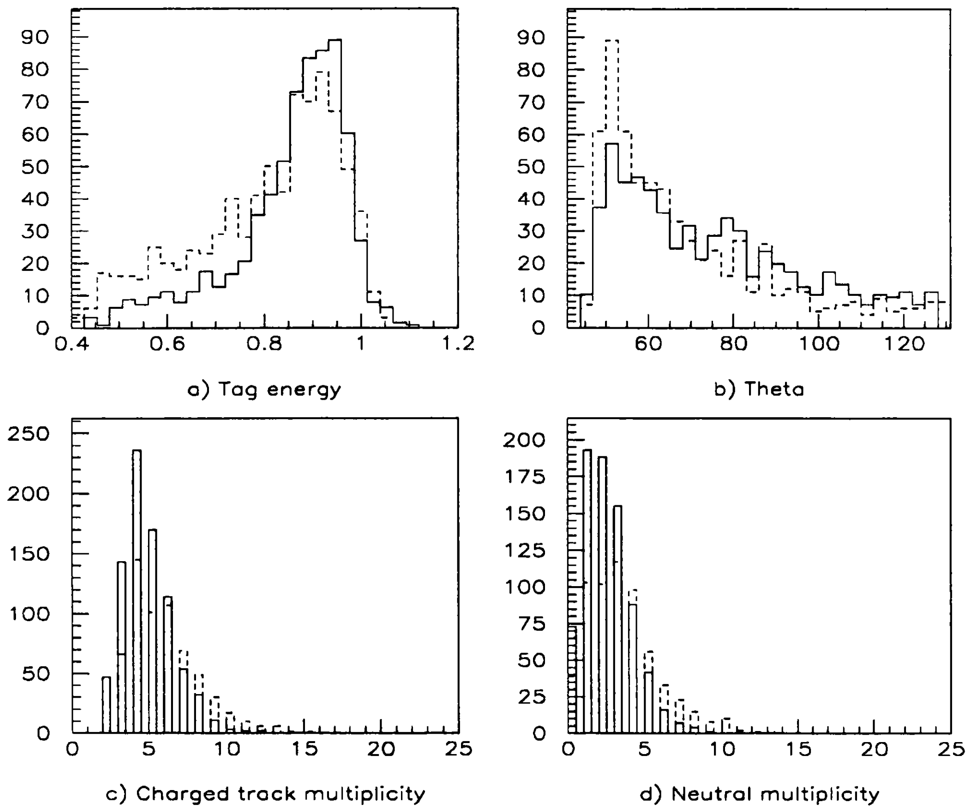

Figure 6.2: Comparison of some raw VMD distributions for peripheral (solid histogram) and pointlike (dashed histogram) scattering of the quarks in the $\gamma\gamma$ centre of mass.

6.1.2 Estimating f_{point} from the Data.

For this fit we would ideally like to use a distribution in which there is a large difference in shape between the VMD peripheral and VMD pointlike distributions. Several such potential distributions are shown in figures 6.2 and 6.3 and it can be seen that the most sensitive are probably the x_{vis} and x_{track} distributions. If however we fit to these distributions then we virtually guarantee that our unfolding result will be close to the $F_2(x, Q^2)$ used to generate the Monte Carlos. We would thus prefer to fit to another distribution less directly connected with $F_2(x, Q^2)$.

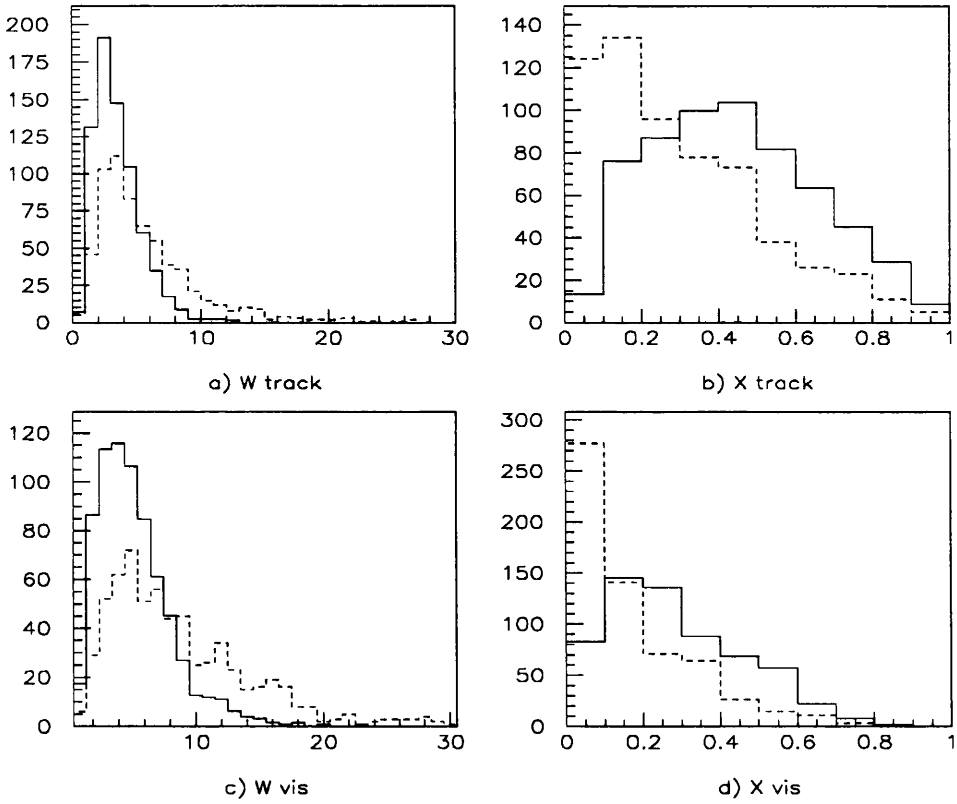

Figure 6.3: Comparison of some physics VMD distributions for peripheral (solid histogram) and pointlike (dashed histogram) scattering of the quarks in the $\gamma\gamma$ centre of mass.

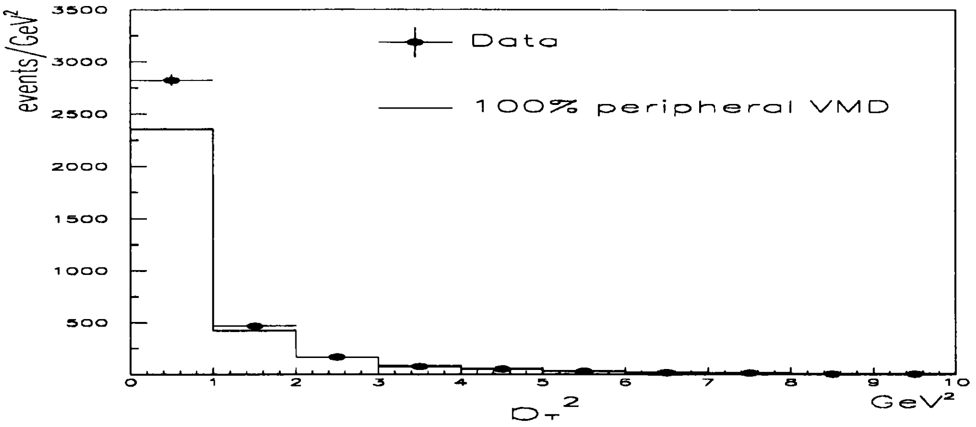

Figure 6.4: p_T^2 of all the good quality tracks for the Monte Carlo (solid histogram) and data (crosses). ($f_{point} = 0.0$ and $p_t^0 = 0.4$)

In previous experiments [5] this fit has been to a distribution where the p_T^2 of every track is put into a histogram, shown for our data in figure 6.4. The Monte Carlo is a sum of normalized QCD($p_t^0 = 0.4$) , VMD peripheral, $c\bar{c}$ and $\tau^+\tau^-$ and thus $f_{point} = 0$. However when we fit to this distribution we get an unphysical value for f_{point} (f_{point} should be between 0 and 1),

$$f_{point} = -1.1 \pm 0.31,$$

(over 8 bins) and it can be seen that it is mainly the first bin that is difficult to fit. A further possibility is to fit using only the track with the maximum momentum in each event which hopefully is closely related to the initial quark direction. A histogram of p_T^{lead} is shown in figure 6.5, where p_T^{lead} is the p_T^2 out of the tag plane of the highest momentum track. The result of the fit is (again over 8 bins),

$$f_{point} = -0.21 \pm 0.18,$$

which is consistent with $f_{point} = 0$.

The fragmentation scheme used (LUND) has not been optimized for low W_{vis} and it might be hoped that if the W_{vis} cut were increased then the Monte Carlo

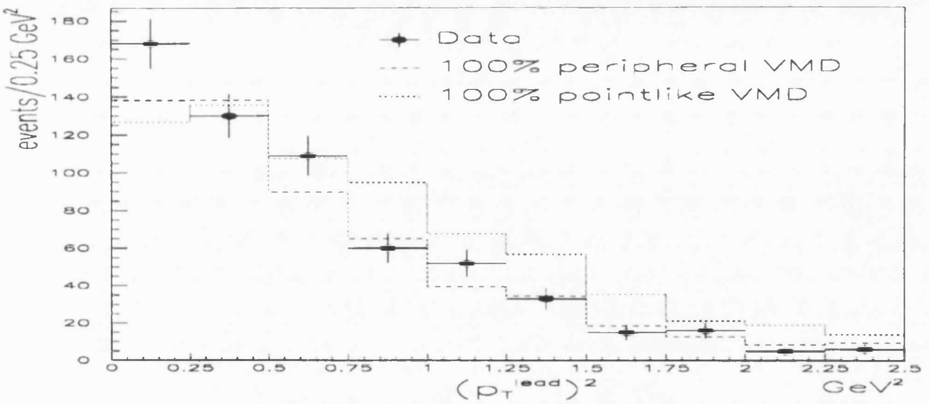

Figure 6.5: p_T^2 (out of the plane of the tag and the beam) of the highest momentum good quality track for the Monte Carlo (solid histogram) and data (crosses). ($f_{point} = 0.0$ and $p_t^0 = 0.4$)

might better represent the data. The result of increasing the W_{vis} cut on the above measurements of f_{point} is presented in table 6.1. It can be seen that increasing the W_{vis} cut to 10 GeV makes both measurements of f_{point} consistent with each other and with $f_{point} = 0$.

We now turn to fit some of the distributions shown in figure 6.2 and 6.3. The results of the various fits are shown in table 6.2. The QCD weight W_{qcd} was also allowed to vary to avoid the overall normalization forcing a particular value of f_{point} to be favoured. All of the stable measurements (ie ones that do not vary more than 1 s.d. when the region which is fitted is changed) of f_{point} in this table are consistent with $f_{point} = 0$. This is the value which we use in our unfolding and data/Monte Carlo comparison. In some sense it is difficult to square the use of a pointlike VMD part with the essentially soft nature of the model, and it is reassuring to see that it is not required by our data.

W_{vis} cut	f_{point}	
	All tracks	Highest p track
> 2.5 GeV	-1.1 ± 0.31	-0.21 ± 0.18
> 5.0 GeV	-1.2 ± 0.31	-0.30 ± 0.21
> 10.0 GeV	-0.34 ± 0.49	0.14 ± 0.41
> 15.0 GeV	0.12 ± 0.58	0.07 ± 0.75

Table 6.1: f_{point} from the tracking information as a function of W_{vis}.

Variable	Bin Range	f_{point}	Stable?	W_{qcd}
Tag Energy	12-23	0.32 ± 0.37	N	0.097 ± 0.019
Q^2	2-12	0.20 ± 0.27	Y	0.104 ± 0.015
Tag Theta	3-22	0.20 ± 0.27	Y	0.101 ± 0.016
W_{vis}	3-13	-0.14 ± 0.23		0.122 ± 0.012
x_{vis}	1-8	0.01 ± 0.15		0.113 ± 0.011
N_{tracks}	3-9 tracks	0.92 ± 0.34	N	0.059 ± 0.016
$N_{neutrals}$	0-9 clusters	0.13 ± 0.32	Y	0.106 ± 0.016

Table 6.2: f_{point} from various measured distributions. The bin range is given from the first to the last bin that is involved in the fit. It is a stable answer if it does not change more than 1 s.d. when the bin limits are varied.

6.1.3 Fit to the QCD Cutoff Parameter p_t^0.

The value of transverse momentum cutoff p_t^0 in the QCD model for $F_2(x, Q^2)$ [33] can be extracted from the unfolded structure function. It would however be affected by the large errors introduced by the unfolding procedure and the reduced information available (ie number of bins over which to fit). We can also obtain p_t^0 by fitting the Monte Carlo x_{vis} distribution to the data (see figures 6.8 and 6.9) with the fixed f_{point} established in section 6.1.2.

If we wish to fit directly to p_t^0 rather than just to the normalization then we need to calculate $W_i^{qcd}(p_t^0)$ and minimize:

$$\chi^2 = \sum_i \left(\frac{d_i - c_i - t_i - V_i^{prf} - W_i^{qcd}(p_t^0) q_i}{\sigma_{d_i}} \right)^2 \tag{6.9}$$

with respect to p_t^0. This is the same as equation 6.1 with $f_{point} = 0$ and $W_{qcd} \rightarrow W_i^{qcd}(p_t^0)$. The data is background subtracted and trigger efficiency corrected; all the Monte Carlo samples are individually normalized to the integrated data luminosity with the weights given in table 5.4, leaving only p_t^0 to be varied.

The method of estimating $W_i^{qcd}(p_t^0)$ on a bin by bin basis is:-

- calculate the average x_{true}, $\overline{x}_{true}$, for each bin of x_{vis} using the QCD Monte Carlo. A plot of x_{true} vs. x_{vis} is given in figure 6.6 and the average x_{true} for each x_{vis} bin is given in table 6.3.
- see how $F_2(\overline{x})$ is affected by a change of p_t^0. A plot of how $F_2(\overline{x})$ at $\overline{x}_{true} = 0.28$ is affected by varying p_t^0 over the range 0.1 to 1 is given in figure 6.7.
- Fit this variation over the region $0.2 < p_t^0 < 0.5$ with a straight line.

This process gives

$$W_i^{qcd}(p_t^0) = \frac{a_i - b_i p_t^0}{a_i - b_i p_t^{0GEN}} W_{qcd} \tag{6.10}$$

where p_t^{0GEN} is the p_t^0 with which the QCD Monte Carlo was generated (see section 5.7), and W_{qcd} is the corrected weight given in table 5.4.

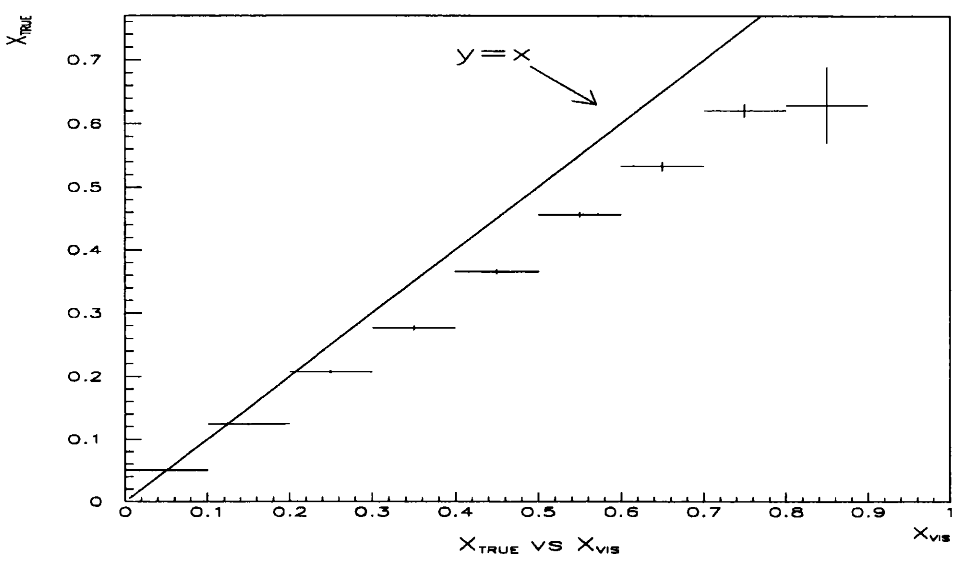

Figure 6.6: x_{true} vs x_{vis} for the QCD Monte Carlo.

x_{vis}		Line fit
range	$\overline{x}_{true}$	$a_i - b_i p_t^0$
0.0-0.1	0.05	$0.17 - 0.07p_t^0$
0.1-0.2	0.12	$0.24 - 0.11p_t^0$
0.2-0.3	0.21	$0.28 - 0.14p_t^0$
0.3-0.4	0.28	$0.30 - 0.16p_t^0$
0.4-0.5	0.37	$0.33 - 0.18p_t^0$
0.5-0.6	0.46	$0.36 - 0.21p_t^0$
0.6-0.7	0.53	$0.38 - 0.23p_t^0$
0.7-0.8	0.62	$0.40 - 0.26p_t^0$
0.8-0.9	0.63	$0.40 - 0.26p_t^0$

Table 6.3: Mean x_{true} per bin of x_{vis}, and variation of $F_2(\overline{x})$ with p_t^0.

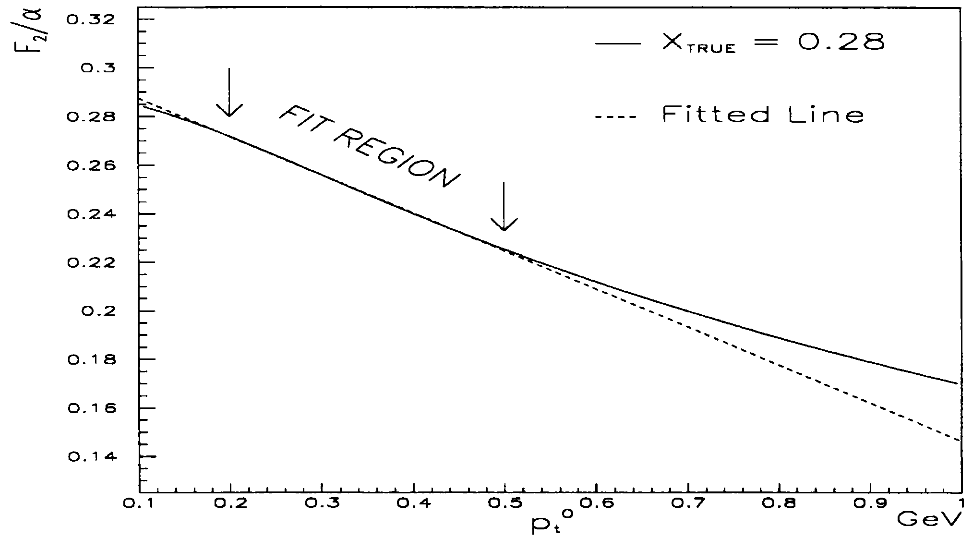

Figure 6.7: The variation of $F_2(x)$ with p_t^0 for $x_{true} = 0.28$ (corresponding to the $0.3 < x_{vis} < 0.4$ bin).

The best-fit p_t^0 values from the direct fit to the x_{vis} distributions (the whole Q^2 range, $Q^2 < 8$ GeV^2, and $Q^2 > 8$ GeV^2) are given in table 6.4. The error given is statistical only. The results are consistent with each other, and consistent with p_t^0 being independent of Q^2. The statement in [20] that p_t^0 should fall with increasing Q^2 cannot be ruled out. The x_{vis} distributions for $Q^2 < 8$ GeV^2 and $Q^2 > 8$ GeV^2 are shown in figures 6.8 and 6.9 respectively.

Q^2 range (GeV^2)	Fit range	p_t^0 (GeV)	χ^2/dof
$4 < Q^2 < 31$	0.0-0.8	0.44 ± 0.12	7.0/7
$4 < Q^2 < 8$	0.0-0.5	0.38 ± 0.19	7.9/7
$8 < Q^2 < 31$	0.0-0.8	0.47 ± 0.16	2.7/4

Table 6.4: p_t^0 results from the fit to the x_{vis} distribution.

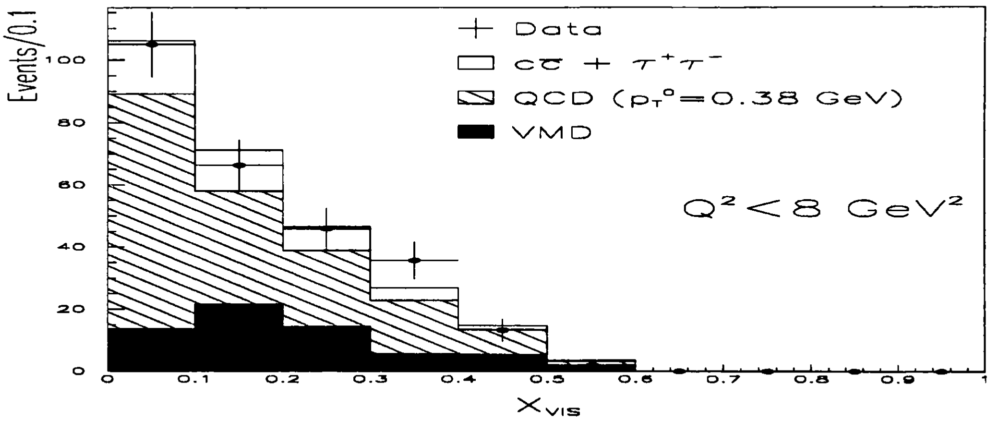

Figure 6.8: x_{vis} for $Q^2 < 8$ GeV^2. The unshaded part of the histogram represents $\tau^+\tau^-$ and $c\bar{c}$ events.

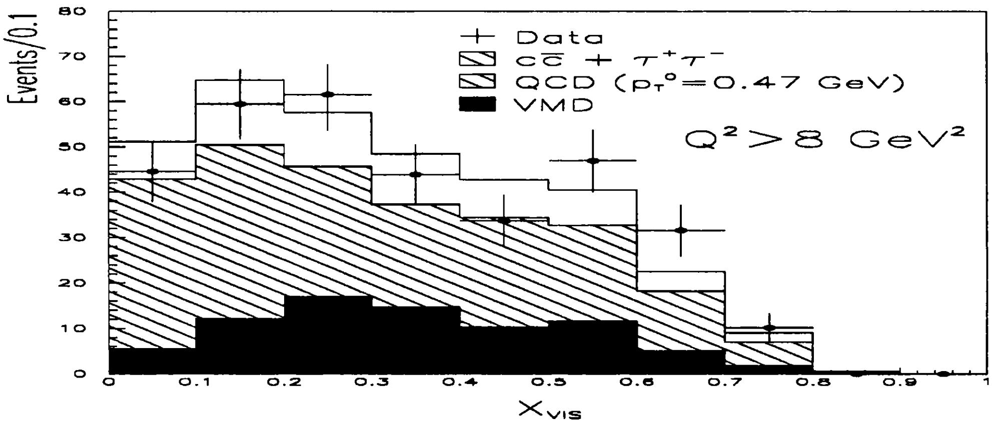

Figure 6.9: x_{vis} for $Q^2 > 8$ GeV^2. The unshaded part of the histogram represents $\tau^+\tau^-$ and $c\bar{c}$ events.

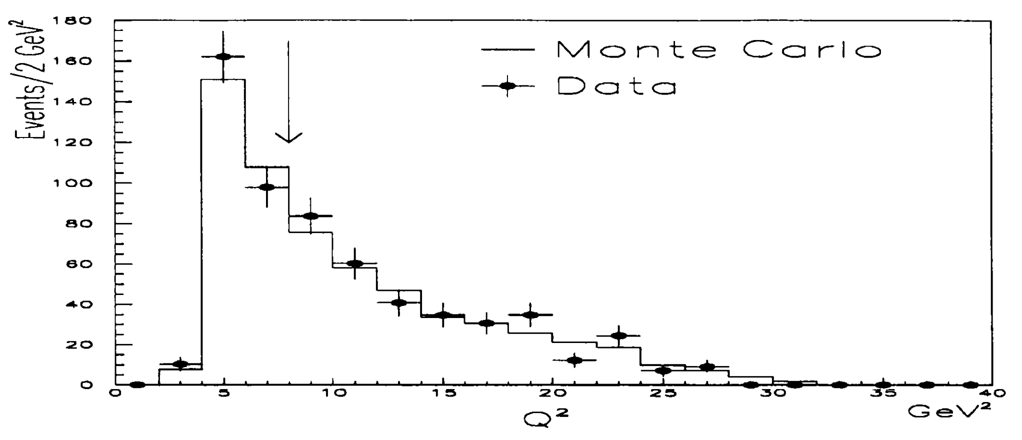

Figure 6.10: Q^2 for the Monte Carlo (solid histogram) and data (crosses). The arrow represents where the data is divided into two Q^2 regions.

6.2 Comparison of data and Monte Carlo.

In this section the trigger efficiency corrected data is compared with the Monte Carlo sum,

$$\mathrm{QCD} + \mathrm{VMD} + c\bar{c} + \tau^+\tau^-$$

where each contribution is individually normalized to the experimental integrated luminosity. The values of the free parameters are $f_{point} = 0.0$ and $p_t^0 = 0.44$, as derived in sections 6.1.2 and 6.1.3. The data are split into two regions of Q^2 - $Q^2 < 8$ and $Q^2 > 8$ (see figure 6.10) and the comparison is made separately in each region. Each distribution is plotted with all the analysis cuts applied both to the data and the Monte Carlo, except for cuts made on the quantity being plotted. Those cuts are represented by the arrows on the plots.

The comparison of data and Monte Carlo for various distributions with $4 < Q^2 < 8$ GeV^2 are given in figures 6.11, 6.12 and 6.13. Similar distributions for $8 < Q^2 < 31$ GeV^2 are shown in figures 6.14, 6.15 and 6.16.

The event distributions in E_{TAG}/E_{BEAM}, θ_{TAG} and $E_{antitag}/E_{BEAM}$ shown in figures 6.11(a), (b), (d) and 6.14(a), (b), (d) demonstrate that the tagged leptons are reasonably well described by the Monte Carlo, and that the antitagging cut is safe. The disagreements between the data and the simulation at low tag energies in figures 6.11(a) and 6.14(a) are principally caused by the classes of background discussed in section 4.1 above. It is more prominent in the low Q^2 region because $Q^2 \propto E_{TAG}$ (see equation 1.3). Figures 6.11(c) and 6.14(c) show that the Monte Carlo and data have a similar forward calorimeter calibration.

Figures 6.12 and 6.15 show variables which depend upon the simulation of the hadronic final state. The agreement is good except perhaps for figures 6.12 and 6.15 where the data shows signs of having more tracks per event. This need not be so surprising since the Lund fragmentation routine is not expected to be very reliable for hadron systems with low invariant mass W as already discussed in section 6.1.2 above. ${p_T}^{IN}$ is the component of the total transverse momentum of the event (tag and tracks only) in the plane defined by the tag and the beam, and ${p_T}^{OUT}$ is the p_T out of this plane (tracks only by definition).

The x_{vis} distributions were shown in figures 6.8 and 6.9 and the Q^2 distribution in 6.10. Figures 6.13 and 6.16 show some other physics distributions. The x_{track}, the counterpart to x_{vis} which only uses tracking information, distributions are shown in figures 6.16(b) and 6.16(b) along with the W_{track} distributions (figure 6.13(a) and 6.16(a)) from which they are derived (see equation 1.4).

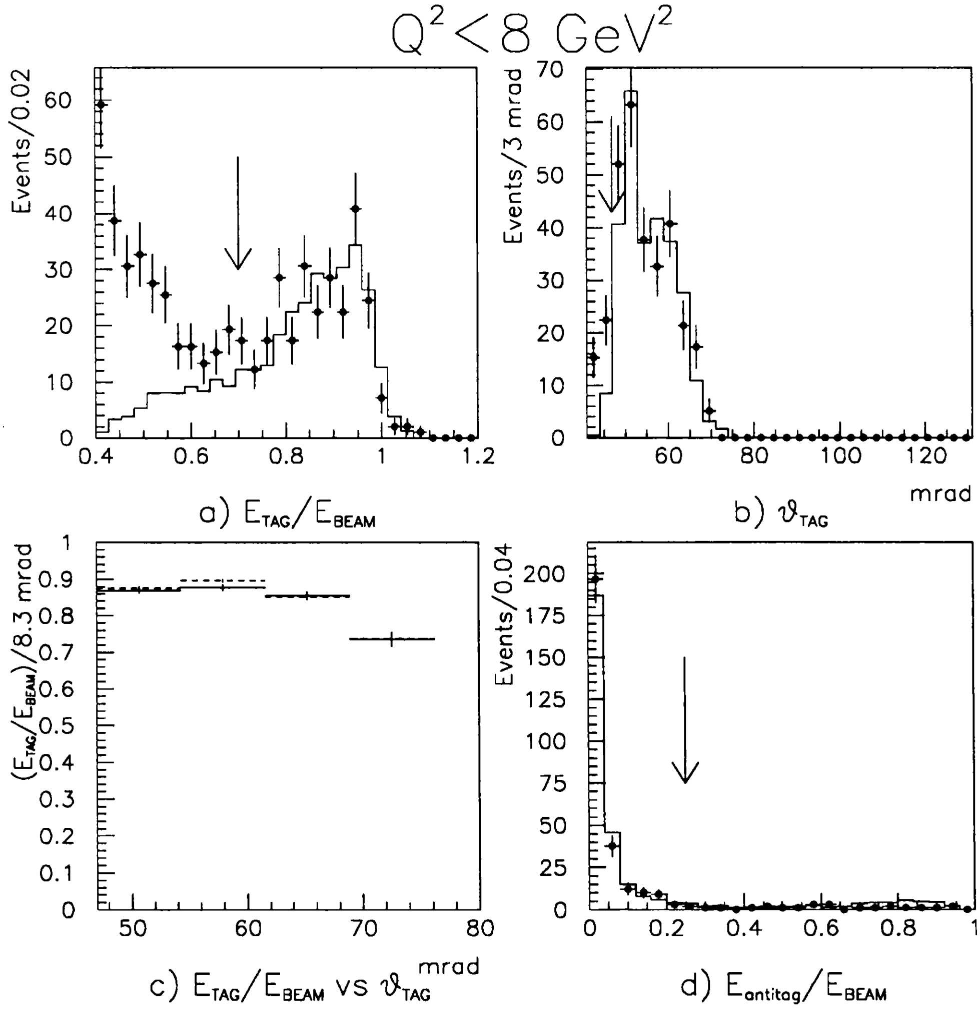

Figure 6.11: Tag distributions. The Monte Carlo is the solid histogram and the data are the points. In c) the Monte Carlo is the dashed histogram.

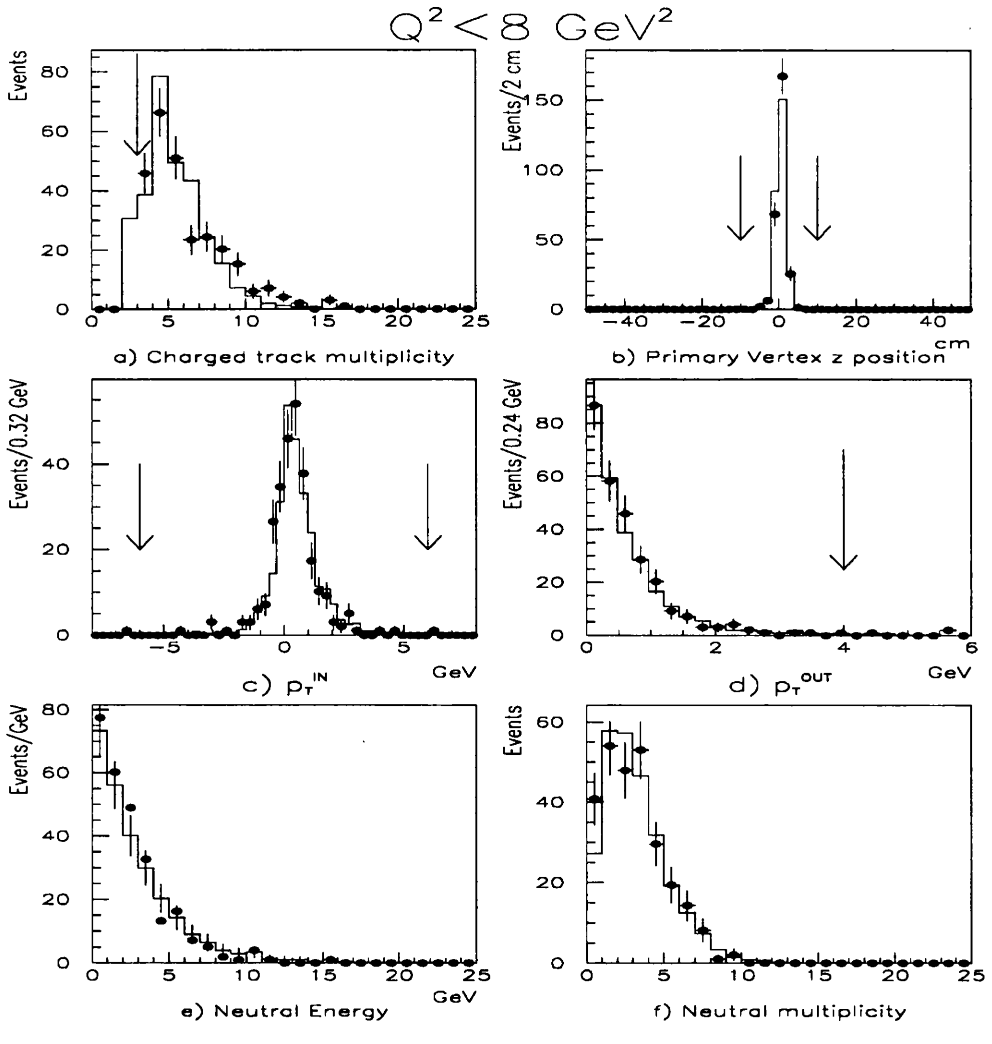

Figure 6.12: Some cut distributions. The Monte Carlo is the solid histogram and the data are the points.

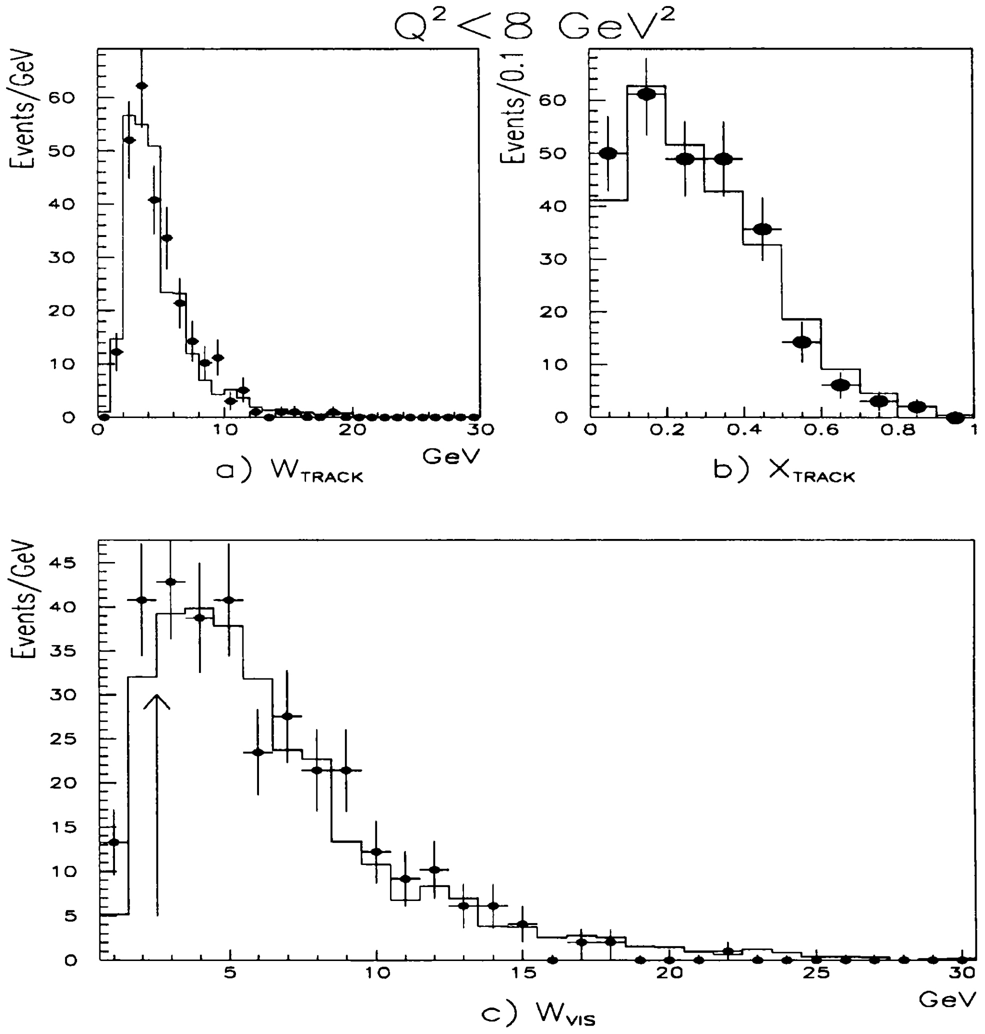

Figure 6.13: Some physics distributions. The Monte Carlo is the solid histogram and the data are the points. The x_{vis} distribution is shown in figure 6.8.

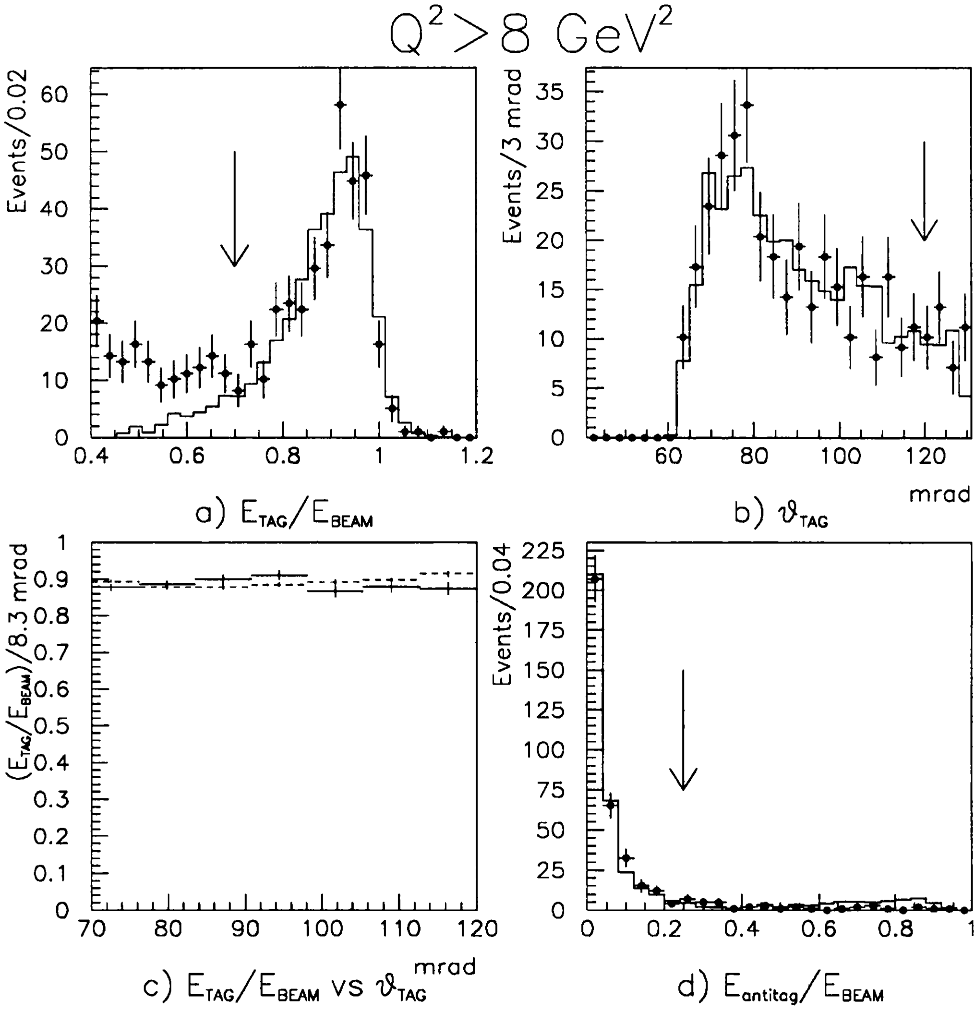

Figure 6.14: Tag distributions. The Monte Carlo is the solid histogram and the data are the points. In c) the Monte Carlo is the dashed histogram.

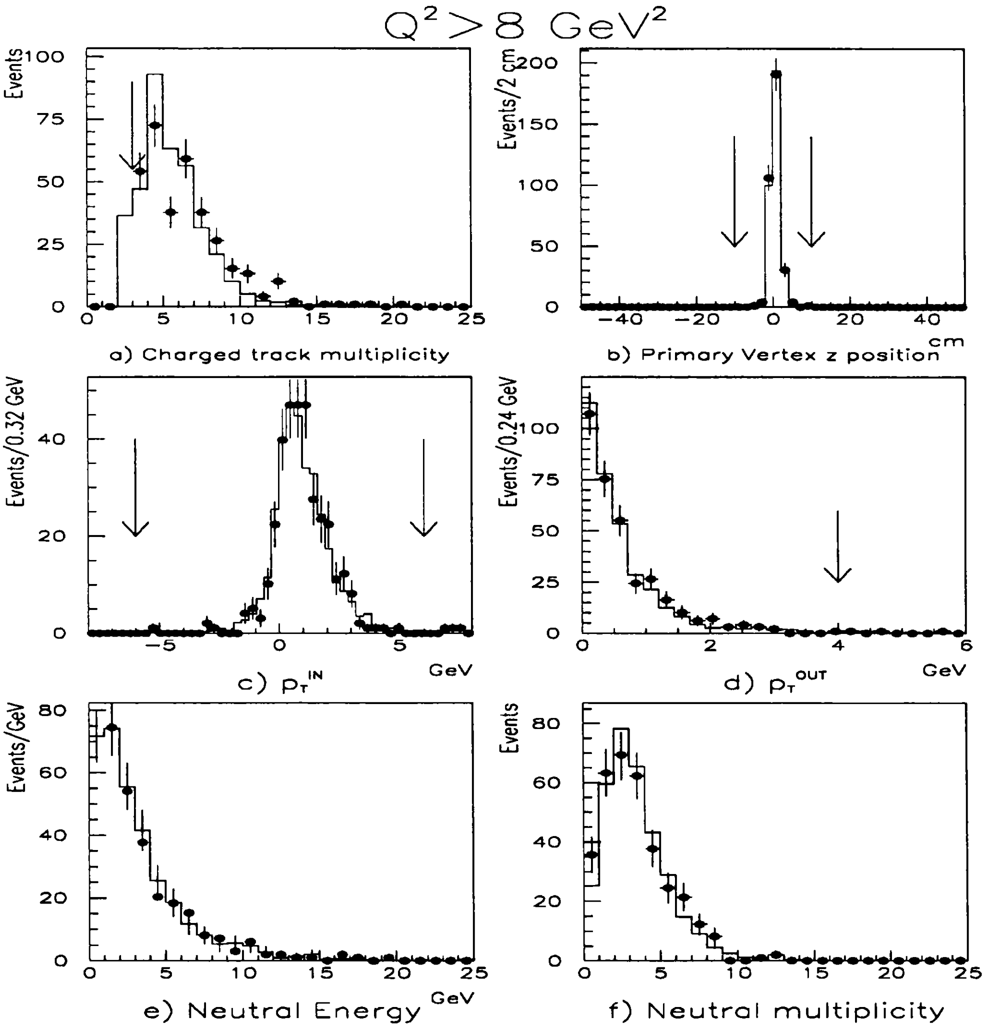

Figure 6.15: Some cut distributions. The Monte Carlo is the solid histogram and the data are the points.

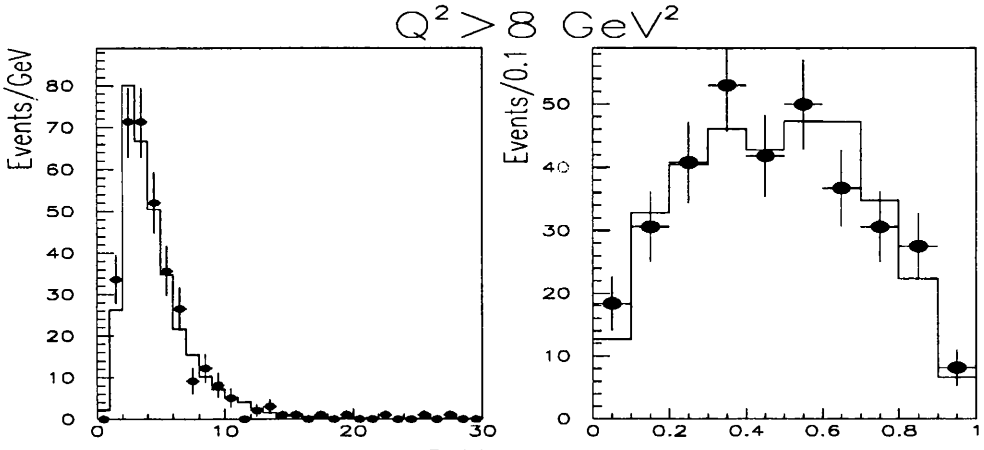

a) W_{TRACK} b) X_{TRACK}

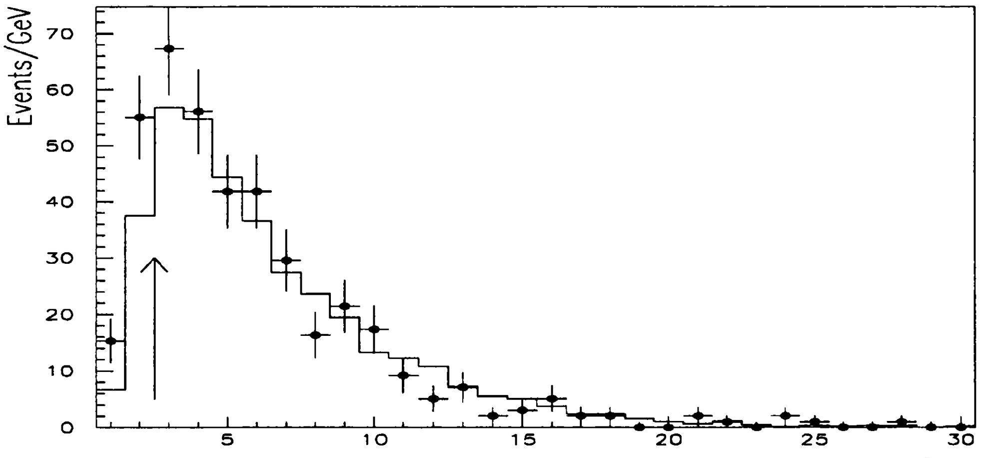

c) W_{VIS}

Figure 6.16: Some physics distributions. The Monte Carlo is the solid histogram and the data are the points. The x_{vis} distribution is shown in figure 6.9.

Chapter 7

Unfolding

Our objective is to measure $F_2(x, Q^2)$, the 'true' distribution behind our observables x and Q^2. With an ideal detector we could just obtain $F_2(x)$ from a simple histogram of x but with our real detector this determination is complicated by three effects:

1) Limited acceptance

   The probability of observing a given event is less than one.

2) Transformation

   Instead of measuring x one measures some related quantity x'. In our case this is caused by losing some of the hadronic particles for one of various reasons; the particles travel down the beam pipe and are not detected at all, the particles are of low energy/angle and do not pass the quality cuts imposed on tracks and electromagnetic clusters, or the particles would only be detected in the hadron calorimeter (which is not used in this analysis). This loss causes the measured invariant mass of the hadronic system to be less than the true invariant mass which means that the measured x' is, in general, greater than the true x (equation 1.4).

3) Resolution

   The measured quantities are smeared out due to the finite resolution of the detector.

The reconstruction of our $F_2(x)$ from our measured $\hat{g}(x')$ distribution is called unfolding.

7.1 Theory of Unfolding

The reader is directed to Blobel's paper on unfolding [57] for a more detailed description of the theory.

As indicated above, the problem is to relate the true $F_2(x)$ to the actual measured $\hat{g}(x')$ distribution. For a given true distribution $f(x)$ defined over the range $a \leq x \leq b$, the expected distribution, $g(x')$ in the measured variable x' can be written as a convolution:

$$g(x') = \int_a^b A(x', x) f(x) dx + b(x') \tag{7.1}$$

where $A(x', x)$ describes the response of the detector and $b(x')$ represents the (known) background. The measured distribution $\hat{g}(x')$ will differ from $g(x')$ by statistical errors $\epsilon(x)$. To obtain the true $f(x)$ for the data, equation (7.1) must be discretized resulting in an equation of the form

$$g = Aa + b \tag{7.2}$$

where g, a and b are vectors, and A is a matrix representing the response function $A(x', x)$.

The discretization of (7.1) is done in two steps. Firstly the function $f(x)$ is parameterized by a sum

$$f(x) = \sum_{j=1}^{m} a_j p_j(x) \tag{7.3}$$

using a set of basis functions, $p_j(x)$. From this follows

$$\int_a^b A(x', x) f(x) dx = \sum_{j=1}^{m} a_j \left(\int_a^b A(x', x) p_j(x) dx \right) = \sum_{j=1}^{m} a_j A_j(x') \tag{7.4}$$

with $A_j(x') = \int_a^b A(x',x)p_j(x)dx$.

Now (7.1) can be written

$$g(x') = \sum_{j=1}^{m} a_j A_j(x') + b(x') \tag{7.5}$$

The expected distribution $g(x')$ is now expressed as a superposition of the functions $A_j(x')$, each representing the response to one term $p_j(x)$ in the representation (7.3).

The second discretization step is just to bin all the x'-dependent functions using bin limits $x'_0, x'_1, ..., x'_n$:

$$g_i = \int_{x'_{i-1}}^{x'_i} g(x')dx' \quad A_{ij} = \int_{x'_{i-1}}^{x'_i} A_j(x')dx' \quad b_j = \int_{x'_{i-1}}^{x'_i} b(x')dx' \tag{7.6}$$

Now equation (7.1) can be represented in the form (7.2). g and b are n-vectors, representing histograms of the measured quantity x'. a is an m-vector of coefficients a_j, and A is an n-by-m matrix, the elements of which are defined by the Monte Carlo events. In the matrix A_{ij} the column A_j represents the histogram in x' for $f(x) = p_j(x)$.

The basis functions $p_j(x)$ should satisfy,

$$p_j(x) \geq 0 \qquad \sum_{j=1}^{m} p_j(x) \equiv 1 \tag{7.7}$$

in order to avoid negative weights and to simplify normalization. The simplest choice of basis functions compatible with 7.7:

$$p_j(x) = \begin{cases} 1 & \text{for } t_{j-1} \leq x < t_j \\ 0 & \text{otherwise} \end{cases} \tag{7.8}$$

with knots (or in this case also bin limits) $t_0, t_1 \ldots t_m$. This has the disadvantages that $f(x)$ has discontinuities and that the approximation of the integrand in 7.4 is inaccurate. Another choice for the functions p_j are cubic B-splines. The solution $f(x)$ is then a smooth curve and the result is presented in bins by integration over this curve,

$$f_k x = \left(\int_{x_{k-1}}^{x_k} f(x)\, dx \right) /((x_k - x_{k-1}).$$

The unfolding can now proceed through a fit of the linear expression $g = Aa + b$ to the data $\hat{g}$. The matrix inversion method (for the case n=m),

$$a = A^{-1}(\hat{g} - b),$$

can show oscillating behaviour, with fluctuations much larger than any physically motivated expectations [57]. This actually arises because insignificant components of the solution often end up with a large weight factor and thus any statistical fluctuations tend to produce oscillations in the unfolded result.

The maximum likelihood method can be used fit for the a_i. The negative log likelihood function $S(a)$ can be written,

$$S(a) = -\sum_{i=1}^{n} \ln P(\hat{g}_i | g_i)$$

where $P(\hat{g}_i | g_i)$ is the probability of observing $\hat{g}_i$ events if g_i are expected. A search for the minimum of the function $S(a)$, gives the best fit values for the a_i. Assuming Poisson statistics and ignoring constant terms,

$$S(a) = \sum_{i=1}^{n} (g_i - \hat{g}_i \ln g_i).$$

If a quadratic approximation is used, an initial solution $\tilde{a}$ can be improved as follows

$$S(a) = S(\tilde{a}) - (a - \tilde{a})^T h + \frac{1}{2}(a - \tilde{a})^T H (a - \tilde{a}),$$

where h and H are

$$h_j = -\frac{\partial S}{\partial a_j} \qquad H_{jk} = -\frac{\partial^2 S}{\partial a_j \partial a_k}.$$

From the minimum condition $\nabla S = 0$,

$$a = \tilde{a} + H^{-1} h.$$

This process is iterated until both the expected change in $S(a)$

$$\nabla S_{exp} = -\frac{1}{2}(a - \tilde{a}) h$$

and the actual change in $S(a)$ are small.

This method of finding the solution does not remove the inherent instability. We can however make a change of basis. H is symmetric, so it can be transformed to a diagonal matrix D,

$$D = U_1^T H U_1.$$

The matrix D contains the real (positive) eigenvalues of H on the diagonal. These eigenvalues can be arranged such that $D_{11} \geq D_{22} \geq \ldots d_{mm}$ and in typical applications they decrease by several orders of magnitude. If $D^{1/2}$ contains the positive square roots of these eigenvalues, a can be transformed

$$a = U_1 D^{-1/2} a_1. \tag{7.9}$$

The importance of this transformation is that the covariance matrix $V(a_1)$ is equal to the unit matrix I. This means the $(a_1)_j$ are all independent and have variance 1. As these components are independent we can test the significance of every component independently. If all $(a_1)_j$ with $j > m_0$ are consistent with zero, they can be ignored, and the result can be expressed as a combination of the first m_0 eigenvectors. In fact it is these insignificant components which cause the fluctuations in the full solution. Equation 7.9 can be rewritten as

$$a_i = \sum_{j=1}^{m} \left(\frac{1}{D_{jj}} \right)^{1/2} (a_1)_j u_{ij}$$

Because of the $1/D_{jj}^{-1/2}$ the insignificant components get a large weight factor in the full solution. Merely setting all $(a_1)_j = 0$ where $j > m_0$ introduces fluctuations known as "Gibbs phenomenon", so a regularization technique is used. This technique introduces a smooth cut off in the $(a_1)_j$ whilst introducing a bias much less than the statistical error. The basis functions $p_j(x)$ can also be transformed to $p_j'(x)$ such that

$$f(x) = \sum_{j=1}^{m} \overline{(a_1)}_j p_j'(x),$$

where $\overline{(a_1)}_j$ includes the regularization weight.

Finally one has to choose m_0 data points by integrating over regions of $f(x)$. These should be chosen to minimize the correlations between the points. Since the function p'_{m_0+1} has m_0 zeros, it seems optimal to define the integration regions of $f(x)$ around these m_0 zeros [57]. This further reduces the contribution of the $\overline{(a_1)}_{m_0+1}p'_{m_0+1}$ term, which is attenuated by a factor of roughly $\frac{1}{2}$.

In his paper Blobel gives a numerical example which uses his code. This example has been reproduced and the results are presented in appendix A.

7.2 The Unfolded Structure Functions

The data have been split into two Q^2 bands ($4 < Q^2 \leq 8$ GeV^2 and $8 < Q^2 < 32$ GeV^2) and each set is unfolded to give an $F_2(x)$ averaged over Q^2 for that region. The value of f_{point} estimated in chapter 6 ($f_{point} = 0.0$) is used to present the results.

The unfolding program was presented with the data and QCD, VMD peripheral, $c\bar{c}$ and $\tau^+\tau^-$ Monte Carlo samples. All the events presented passed the selection cuts described in chapter 4 and the Monte Carlos were given the weights shown in table 5.4. Corrections to take account of the measured trigger inefficiency (section 4.3.2) and the x dependence of the P^2 correction shown in figure 5.5 were made by scaling weights within the unfolding program. The contributions from $e^+e^-\rightarrow e^+e^- + \tau^+\tau^-$ and $e^+e^-\rightarrow e^+e^- + c\bar{c}$ were treated as background and were subtracted from the data by the program. Thus the results represent our measured F_2 for u,d and s quarks. The outputs from the unfolding program are shown in figures 7.1 ($Q^2 < 8$ GeV^2) and 7.2 ($Q^2 > 8$ GeV^2). The final results, given in tables 7.1 and 7.2, are corrected for the backgrounds discussed in section 4.2.

The curves shown in figures 7.1 and 7.2 are output curves from the Blobel unfolding program. The points represent the average of these curves over the horizontal bar and the error on each point is that output by the Blobel program. The binning is chosen internally to minimize the contribution of the functions shown in figures 7.3 and 7.4 as discussed at the end of section 7.1.

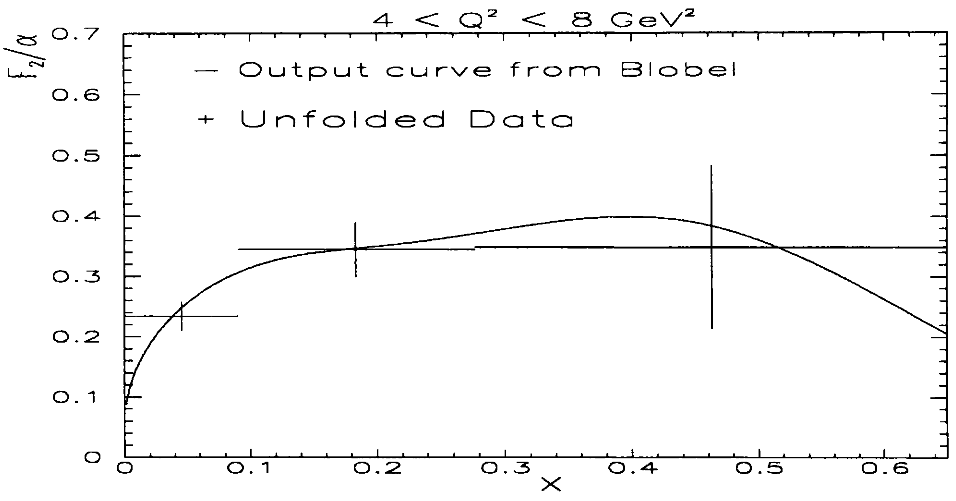

Figure 7.1: The output points from Blobel for $Q^2 < 8$ GeV^2, along with the curve over which the points are averaged.

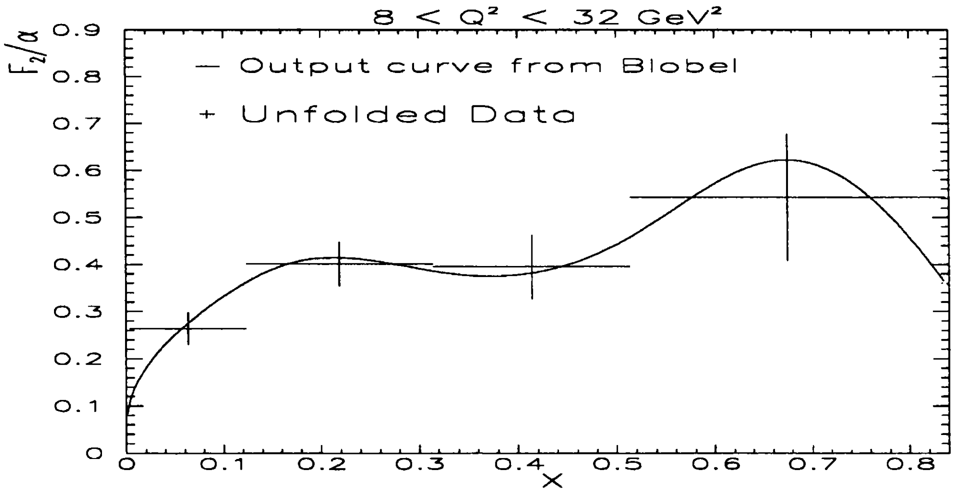

Figure 7.2: The output points from Blobel for $Q^2 > 8$ GeV^2, along with the curve over which the points are averaged.

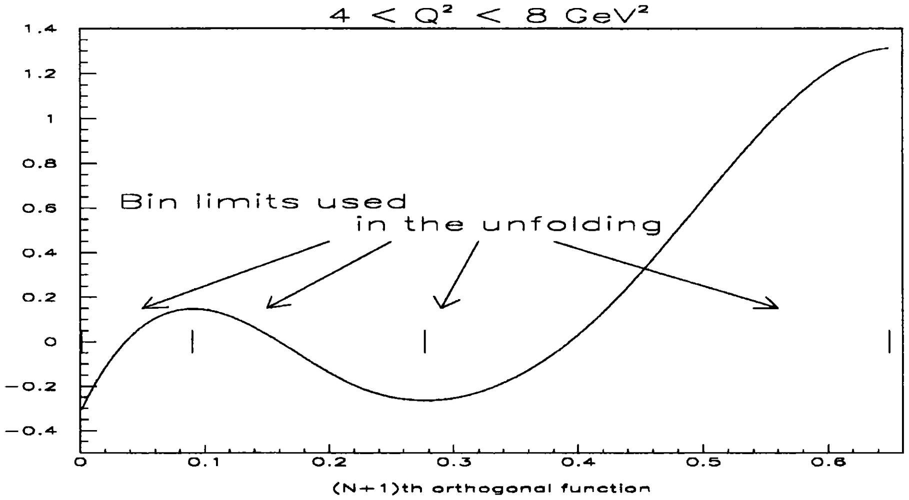

Figure 7.3: The (m_0+1)th function for the $Q^2 < 8\ \mathrm{GeV}^2$ region.

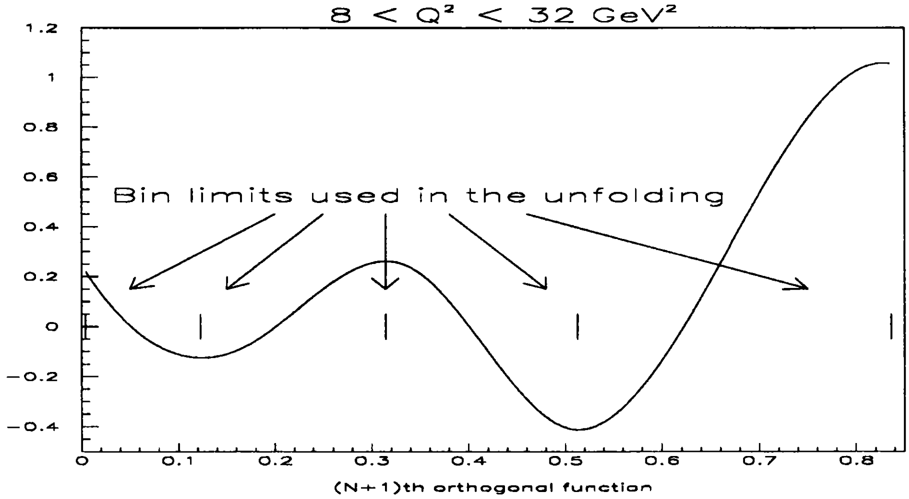

Figure 7.4: The (m_0+1)th function for the $Q^2 > 8\ \mathrm{GeV}^2$ region.

7.2.1 Systematic Errors

The results presented above are shown with only the statistical errors coming from the unfolding itself. Several sources of systematic error have been considered, as follows. They are summarized in tables 7.1 and 7.2.

(a) Variation of Blobel internal parameters.
The systematic error under the heading of unfolding in tables 7.1 and 7.2 came from the RMS of the unfolded results produced by varying various Blobel parameters. The unfolding procedure handles the data internally in the form of binned histograms. The number of bins in these histograms and the sizes of the bins were varied (from having all the bins the same size to having all the bins with roughly equal contents). A different number of final unfolded points was also demanded.

The number of bins was varied from 6 to 30. The precise number used for the final result was chosen to lie close to the average produced by this variation and also chosen to be in the region of 20 events per bin (14 bins for $Q^2 < 8$ GeV^2 and 22 bins for $Q^2 > 8$ GeV^2).

When the program was run to produce a different number of final unfolded points the resultant output curve (similar to the one shown in figure 7.2) was averaged over the bin ranges given in tables 7.1 and 7.2 to produce unfolded points comparable with those of the final result. The high Q^2 region was run to produce 3 and 5 points, the low Q^2 to produce 4 (the program does not allow the production of a final result in 2 points). Demanding a different number of points in the unfolded result tells the program where to cut off the higher order orthogonal functions (see section 7.1) which is what leads to the different curves produced.

(b) Variation of cuts.
The unfolding was repeated with the E_{TAG} cut varying in steps of $0.02E_{BEAM}$ from $0.66E_{BEAM}$ to $0.74E_{BEAM}$ inclusive. This represents changing the central value ($0.7E_{BEAM}$) by ±1 and ±2 times the energy resolution of the forward calorimeter. The RMS of the scatter was assigned as a systematic on a point by point basis and is given in tables 7.1 and 7.2 under the heading E_{TAG}. Most

of the backgrounds discussed in section 4.2 are sensitive to the tag energy cut, so any variation due to a change in this cut is an indication of how well those backgrounds are described.

The W_{vis} cut was varied from 2.0 to 3.0 GeV, inclusive, in steps of 0.25 GeV and the cut on the minimum number of good charged tracks was increased from > 2 to > 3. The analysis was also repeated using tracks only, with the cuts on W_{vis} being replaced by similar cuts on W_{track}. The RMS of the resulting scatter of points is assigned as a systematic under the heading hadronic in tables 7.1 and 7.2. Any variation resulting for changing these cuts is taken as an indicator of the the systematic effects of the Monte Carlo (fragmentation of the $q\overline{q}$ system and representation of the OPAL detector).

All the other cuts described in chapter 4 have only a small or negligible effect on the unfolded results.

(c) Monte Carlo normalization.

As mentioned in section 5.5 we estimate a systematic error of 1.3% on the overall normalization of the F2GEN Monte Carlo. The correction made to the normalization to account for initial state radiation (see section 5.6) has an error of 1.8%.

(d) Backgrounds.

The Z^0 background was assumed to have only affected the lowest x unfolded point in each Q^2 band. The systematic error from subtracting this background came from counting the number of normalized Monte Carlo events in the x range of this point. The fractional error is then calculated from this number and the errors given in section 4.2. The errors due to the other background corrections are small and have been neglected.

(e) Other errors.

The error on the integrated data luminosity is 0.7% (see section 4.4). The error on the trigger efficiency is 0.7% as calculated in section 4.3.2.

x range	0.001-0.090	0.090-0.277	0.277-0.649
F_2/α	0.230	0.345	0.349
Statistical err	0.025	0.045	0.135
Unfolding err	0.003	0.010	0.061
Variation of cuts			
E_{TAG}	0.009	0.008	0.022
Hadronic	0.008	0.019	0.113
Total cut error	0.012	0.020	0.115
Z^0 background	0.002	0.000	0.000
Overall syst. err	0.013	0.022	0.130
Total error	0.028	0.050	0.187

Table 7.1: Summary of unfolded $F_2(x)$ measurement at $\overline{Q^2} = 5.9$ GeV^2. There is an additional uncertainty of 2.4% on the overall normalization of $F_2(x)$, arising from the Monte Carlo normalization, the luminosity measurement, the ISR correction and the trigger efficiency correction.

x range	0.006-0.123	0.123-0.314	0.314-0.513	0.513-0.836
F_2/α	0.250	0.401	0.395	0.543
Statistical err	0.034	0.047	0.068	0.135
Unfolding err	0.006	0.009	0.023	0.038
Variation of cuts				
E_{TAG}	0.021	0.011	0.005	0.009
Hadronic	0.007	0.035	0.034	0.111
Total cut error	0.022	0.037	0.034	0.111
Z^0 background	0.006	0.000	0.000	0.000
Overall syst. err	0.024	0.038	0.041	0.118
Total error	0.042	0.060	0.079	0.179

Table 7.2: Summary of unfolded $F_2(x)$ measurement at $\overline{Q^2} = 14.7$ GeV^2. There is an additional uncertainty of 2.4% on the overall normalization of $F_2(x)$, arising from the Monte Carlo normalization, the luminosity measurement, the ISR correction and the trigger efficiency correction.

7.2.2 Comparison with Previous Measurements

The unfolded results are compared with previous results at similar average Q^2 in figures 7.5 (for $Q^2 < 8$ GeV^2 with $\overline{Q^2} = 5.9$ GeV^2) and 7.6 (for $Q^2 > 8$ GeV^2 with $\overline{Q^2} = 14.7$ GeV^2). The curves shown are $\mathrm{F}_2(x)^{VMD}$, $\mathrm{F}_2(x, \overline{Q^2})^{QCD}$ (calculated using the values of p_t^0 fitted in section 6.1.3) and the sum of the two.

In the low Q^2 region the unfolded result agrees well with both the TPC/2γ and PLUTO results. The TPC/2γ results come from [5] and it can be seen that they are much more competitive at higher x, with a much lower error. This mainly comes from the fact that our low W_{vis} cut is placed at 2.5 GeV, whereas theirs is at 1 GeV, thus giving them much more data at higher x. The PLUTO results come from [7] and with their W_{vis} cut at 1 GeV they are again more competitive at high x. At low x however both the PLUTO and TPC/2γ results are systematics limited, whereas the results presented here still have the statistical error as the major component.

In the high Q^2 region the result again agrees well with the PLUTO result taken from [7]. Again we are less competitive at high x, but one important feature of our data is that it goes to much lower x. This is a consequence of running with higher energy beams which means that the $\gamma\gamma$ system can more easily reach higher invariant masses.

Figure 7.7 shows the variation in the mean value of $\mathrm{F}_2(x, Q^2)/\alpha$ for $0.3 < x < 0.8$, as a function of Q^2. The lower integration limit ensures that the effect of the VMD contribution is small, while the upper limit is required because the statistical errors increase rapidly in most experiments as $x \to 1$. The results from this thesis are shown as solid circles and the other results come from [6, 8, 9, 10, 12, 58]. The lines show the predictions of the QCD + VMD model as parametrised in equations 5.2 and 5.9 for several values of the cutoff parameter p_t^0. The errors in the plot are statistical only and our results fit in well with previous measurements. The points shown are consistent with a linear rise of $\mathrm{F}_2(x; Q^2)$ with $\ln Q^2$.

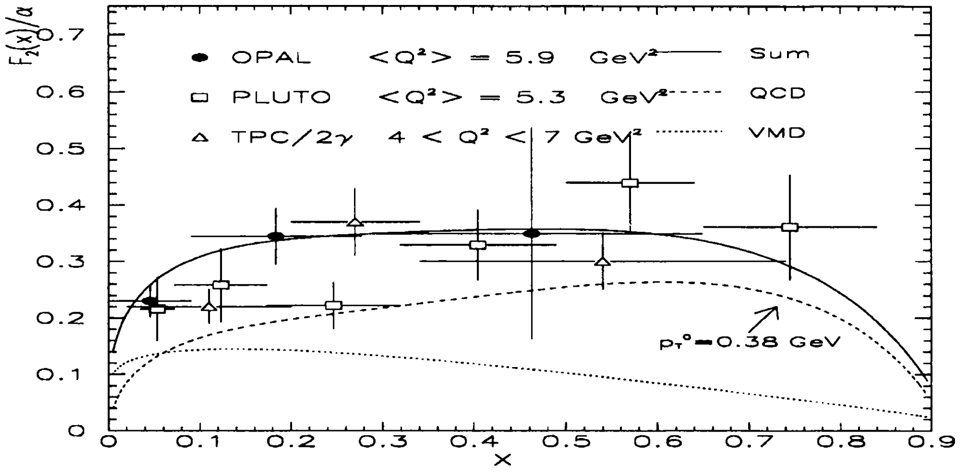

Figure 7.5: Unfolded $F_2(x)$ at $\overline{Q^2}$ = 5.9 GeV^2 compared with previous measurements at similar mean Q^2.

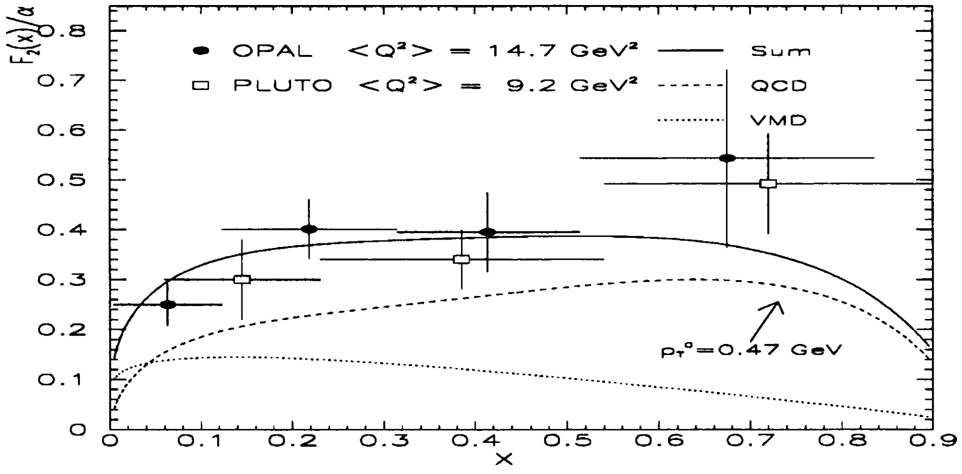

Figure 7.6: Unfolded $F_2(x)$ at $\overline{Q^2}$ = 14.7 GeV^2 compared with previous measurements at similar mean Q^2.

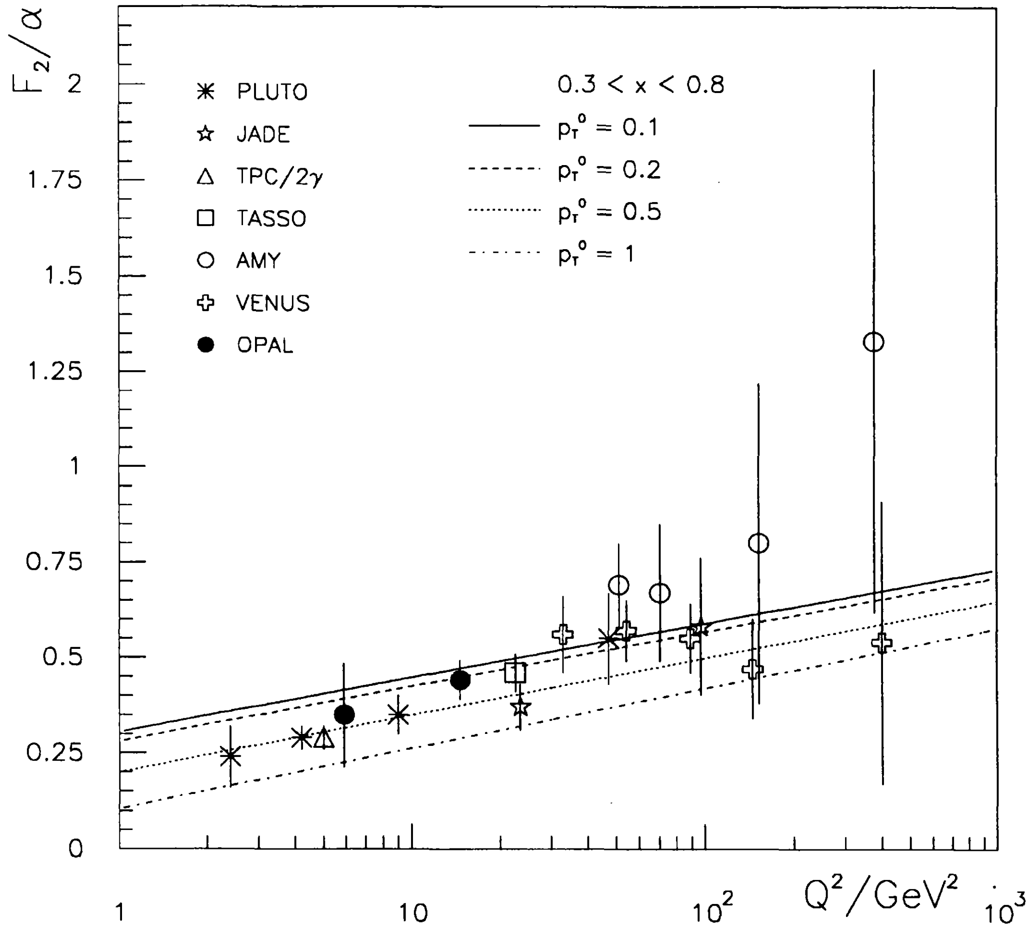

Figure 7.7: Variation of $\overline{F_2(x)}$ $(0.3 < x < 0.8)$ with Q^2 (taken from [59]).

7.2.3 Comparison with Theory

The unfolded results are compared with theoretical predictions in figures 7.8(for $Q^2 < 8$ with $\overline{Q^2} = 5.9$) and 7.9 (for $Q^2 > 8$ with $\overline{Q^2} = 14.7$). Four curves are shown in each graph:

- the sum of $\mathrm{F}_2(x)^{VMD}$ and $\mathrm{F}_2(x, \overline{Q^2})^{QCD}$ is shown as a dotted line. The particular parameterizations used are given in equations 5.9 and 5.2 respectively, and the values of p_t^0 are in table 6.4. The curve is in good agreement with the data in both Q^2 regions.
- the naive sum of $\mathrm{F}_2(x)^{VMD}$ and $\mathrm{F}_2(x)^{QPM}$ is shown as the dashed line. The parameterizations are given in equations 5.9 and 5.11 respectively. This naive sum certainly involves some double counting of diagrams, but the fact that the data cannot rule it out shows the lack of sensitivity to the QCD scale parameter $\Lambda_{\overline{MS}}$. Alternatively it has been suggested [59] that the similarity in value between $\Lambda_{\overline{MS}}$ and the current mass of light quarks ($\sim$ 300 MeV) is no coincidence. They are, in fact, roughly the same thing.
- the LAC II parameterization [60] is shown as the solid curve. This calculation is based on a fit to previous data on $\mathrm{F}_2(x)$ which allows the contributions from the individual quark distributions ($q_i(x, Q^2)$ - see chapter 3) to vary. These distributions are then evolved with Q^2 to give a prediction at any Q^2. In the low Q^2 region it somewhat underpredicts the data. In the high Q^2 region it is low in the region $x > 0.12$. There is no sign of the spike below $x \simeq 0.1$ in the data.
- The GRV parameterization [61] is shown as the dot-dash line. This evolves the $q_i(x, Q^2)$ distributions as LAC does, but fixes them by assuming they are the same as those of the pion at $Q^2 = 0.3$ GeV^2. The spike at low x occurs at much lower x than the LAC II spike, and is too low for our data to have any sensitivity to.

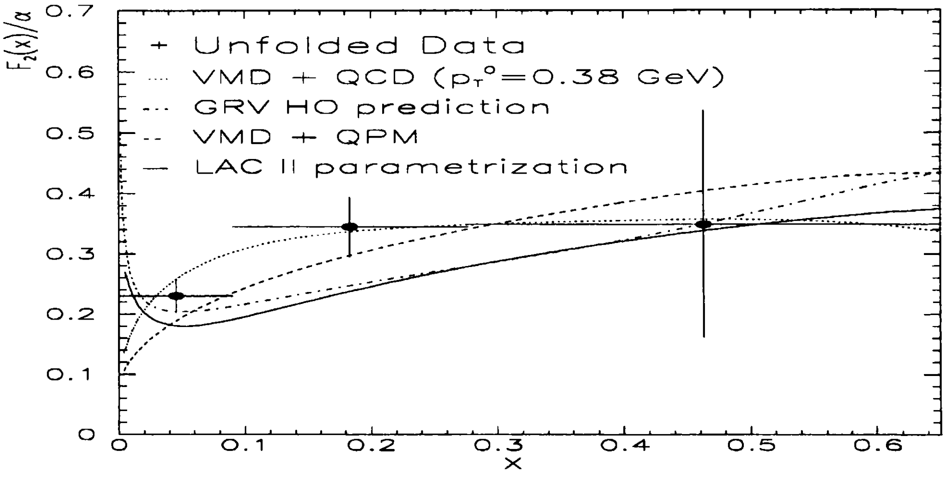

Figure 7.8: Unfolded $F_2(x)$ at $\overline{Q^2}$ = 5.9 GeV^2 compared with various theoretical predictions.

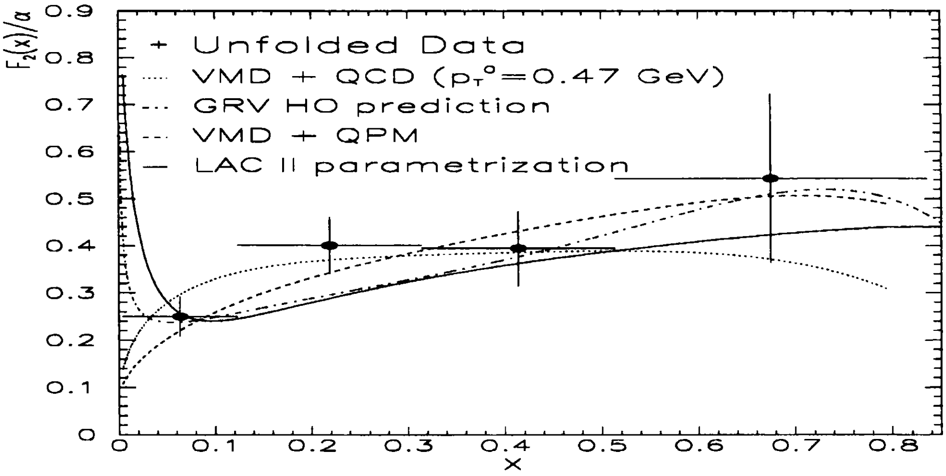

Figure 7.9: Unfolded $F_2(x)$ at $\overline{Q^2}$ = 14.7 GeV^2 compared with various theoretical predictions.

7.3 Conclusions

The data are well represented by a Monte Carlo based on the sum of

$$\mathrm{QCD} + \mathrm{VMD} + c\bar{c} + \tau^+\tau^-.$$

No VMD pointlike component is required by our data. The values of p_t^0, within the parameterization of the all order QCD calculation given in 5.2, preferred by the data are,

$$\begin{array}{ccc} & Q^2 < 8\ \mathrm{GeV}^2 & Q^2 > 8\ \mathrm{GeV}^2 \end{array} \tag{7.10}$$

$$\begin{array}{ccc} p_t^0 & 0.38 \pm 0.19 & 0.47 \pm 0.16 \end{array} \tag{7.11}$$

These values are considerably smaller than the 1.5 GeV mentioned in [20] but are consistent with those of recent experiments (see figure 7.7).

Our unfolded measurements are consistent in shape and normalization with previous experiments at similar $\overline{Q^2}$. They are also consistent with the predictions of a QCD + VMD phenomenological model. The soft hadronic VMD component and the perturbative QCD calculable part come from distinct regions of an integration over p_T of the quarks, and the boundary lies when the quarks in the target photon have transverse momentum of approximately 440 MeV. We confirm a significant pointlike component of the photon is present in our data.

Our measurements extend to lower values of x than previous experiments have achieved, particularly in the higher Q^2 range.

Appendix A

Unfolding using Blobel's Code

This appendix confirms that Blobel's code gives reasonable results when used to unfold for detector effects. First the numerical example given in [57] is repeated, and then we use the generated Monte Carlos samples (as described in chapter 5) to test the unfolding procedure.

A.1 Numerical Example

In this example the measurement of a true $f(x)$ is simulated with $0 \leq x \leq 2$. The Monte Carlo technique is used to simulate limited acceptance and resolution with the following properties:

- The probability of acceptance is assumed to be
  $P_{acc} = 1 - \frac{1}{2}(x-1)^2$
- The true values x are transformed to a variable y_{tr} by the function
  $y_{tr} = x(1 - 0.05x)$
- The variable y_{tr} is assumed to be measured with a gaussian resolution, $\sigma = 0.1$

- The assumed true function is (see table A.1 for parameters used)

$$f(x) = \sum_{k=1}^{3} b_k \frac{g_k^2}{(x - x_k)^2 + g_k^2}$$

k	b_k	x_k	g_k
1	1.0	0.4	2.0
2	10.0	0.8	0.2
3	5.0	1.5	0.2

Table A.1: Parameters of assumed true function.

A samples of 5,000 "data" events were generated according to $f(x)$. A histogram of the sample is shown in figure A.1(a) along with the (scaled-up) generating function. After acceptance, transformation and smearing (see above) 4,443 y-values remain (figure A.1(b)). The transformation restricts y_{tr} to $0 \leq Y_{tr} \leq 1.8$ and narrows the peaks. The resolution function then broadens the peaks and (to some extent) fills the valley between the peaks.

The result of the unfolding (with regularization) can be seen in Fig (A.2) along with the original function. It can be seen that the unfolded result has correctly represented both the peaks and the valley between them. The bin limits in this result were chosen to limit the contribution of the first basis function to which the regularization procedure gave a weight of less than 0.5. In this case that function had twelve zeros and the bins were chosen to put each zero in the centre of a bin.

A.2 Unfolding between Monte Carlos

Firstly the unfolding program was presented with a sample of Monte Carlo (the QCD sample with $p_t^0 = 0.5$). The program used this sample both as the input

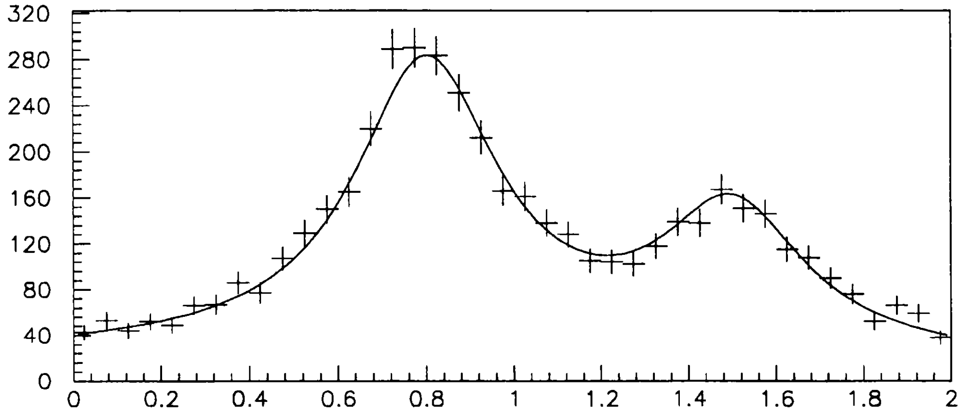

a) True distribution

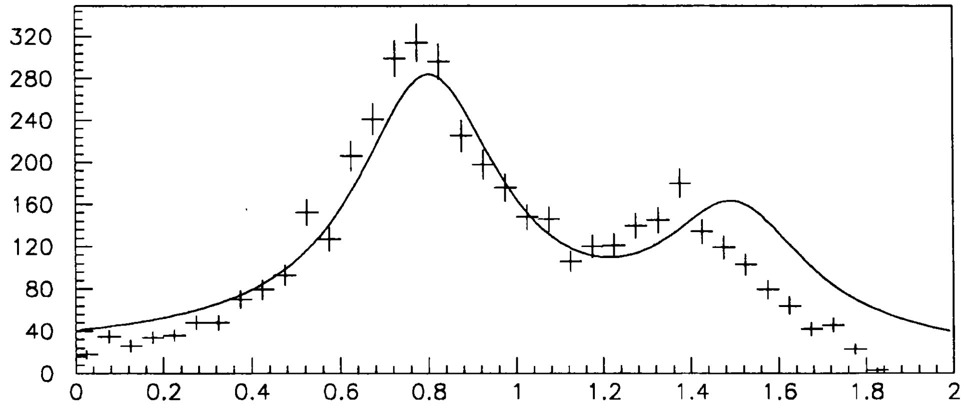

b) Measured distribution

Figure A.1: Histogram of generated data a) before and b) after simulation of acceptance,transformation and resolution. The (scaled) original function is shown as a curve.

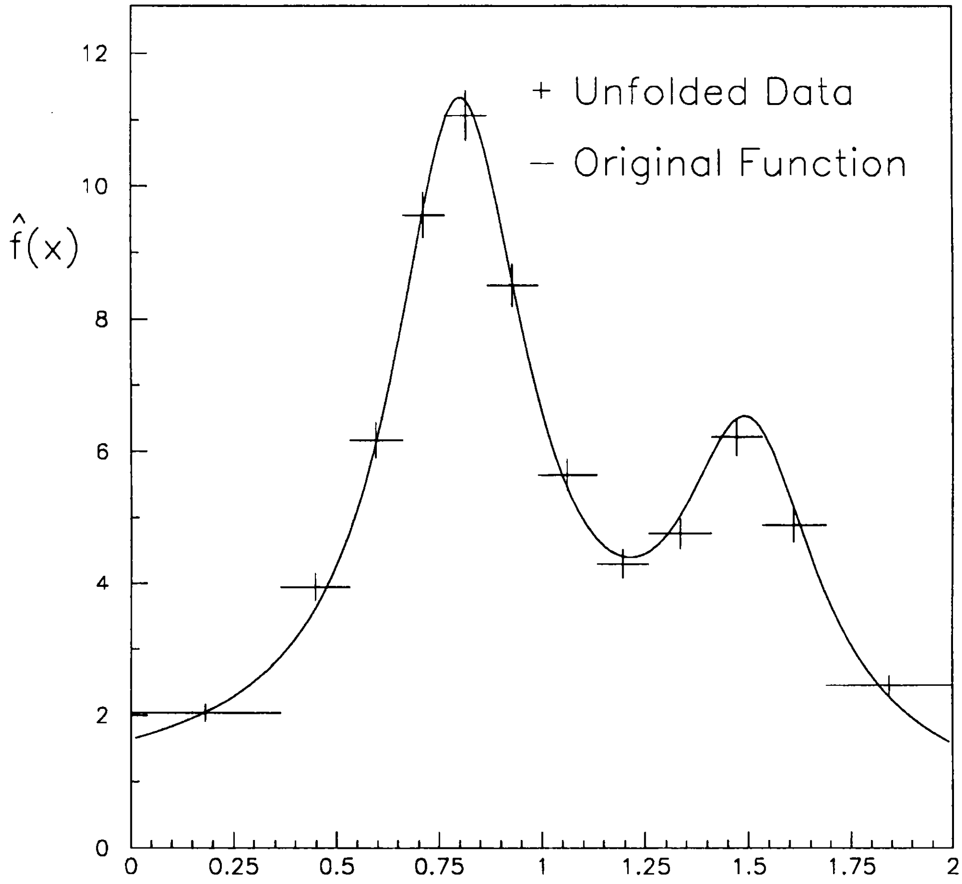

Figure A.2: Result from unfolding program - the horizontal bar gives the range over which the data points represent the average.

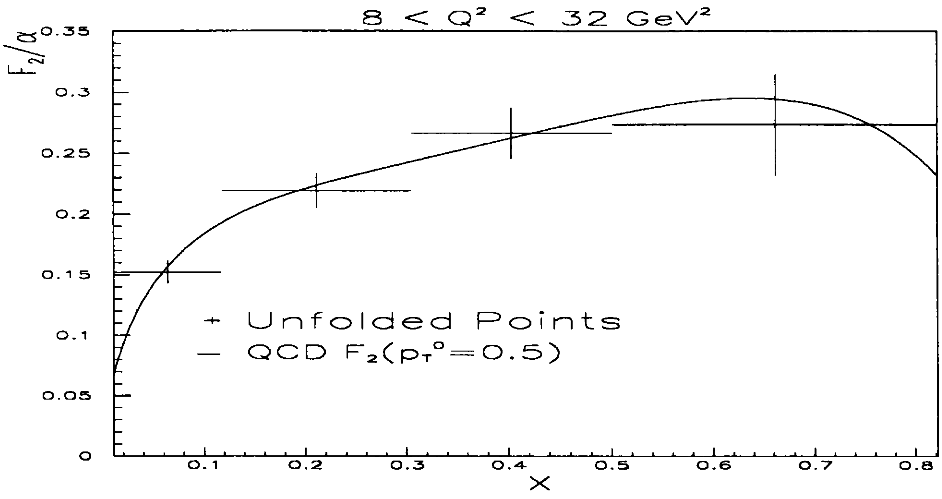

Figure A.3: Unfolding result using the QCD Monte Carlo with $p_t^0 = 0.5$ GeV as both the input data and Monte Carlo. The line represents the expected result.

"data" and the input "Monte Carlo" and should therefore output a curve very similar to the input theory. The output from this test is shown in figure A.3 and it can be seen that the points are a good representation of the curve.

The program was then presented with two samples of VMD pointlike events. The "data" was the sample generated using the F_2 of equation 5.9 and the "Monte Carlo" was generated using

$$F_2(x)/\alpha = 0.2(1 - x).$$

As can be seen in figure A.4 the unfolding procedure recovers the shape of the "data" structure function of equation 5.9 and specifically reproduces the turnover at low x.

In conclusion the above examples show that Blobel's code is reliable when used for unfolding. It successfully reproduces the structure behind the input data both in shape and normalization.

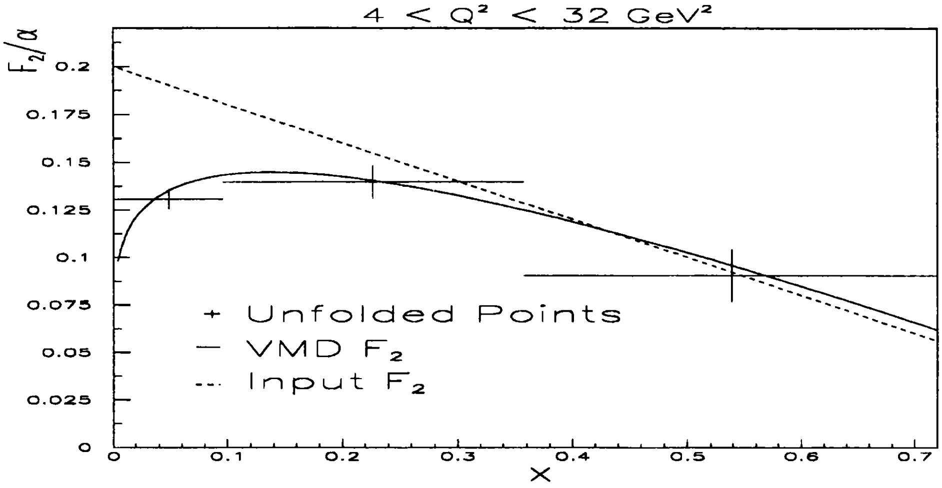

Figure A.4: Unfolding between two VMD Monte Carlo samples. The structure function for the input "data" is shown as the solid line, and for the input "Monte Carlo" as the dashed line.

Appendix B

The OPAL Paper on measuring $\mathbf{F}_2(x)$

The following appendix contains the recent OPAL paper on $F_2(x)$ [13] which has been submitted to Zeitschrift fur Physics C.

EUROPEAN ORGANISATION FOR NUCLEAR RESEARCH

CERN-PPE/93-156
24 August 1993

Measurement of the Photon Structure Function F_2^γ in the Reaction $e^+e^- \rightarrow e^+e^- +$ hadrons at LEP

Abstract

We present measurements of the hadronic photon structure function $F_2^\gamma(x)$, in two Q^2 ranges with mean values of 5.9 GeV^2 and 14.7 GeV^2. The data were taken by the OPAL experiment at LEP, with $\sqrt{s}$ close to the Z^0 mass and correspond to an integrated e^+e^- luminosity of 44.8 pb^{-1}. In the context of a QCD-based model we find the quark transverse momentum cutoff separating the vector meson dominance (VMD) and perturbative QCD regions to be 0.27 ± 0.10 GeV. We confirm that there is a significant pointlike component of the photon when the probe photon has $Q^2 > 4$ GeV^2. Our measurements extend to lower values of x than any previous experiment, and no increase of $F_2^\gamma(x)$ is observed.

The OPAL Collaboration

R. Akers[16], G. Alexander[23], J. Allison[16], K.J. Anderson[9], S. Arcelli[2], A. Astbury[28], D. Axen[29], G. Azuelos[18,a], J.T.M. Baines[16], A.H. Ball[17], J. Banks[16], R.J. Barlow[16], S. Barnett[16], R. Bartoldus[3], J.R. Batley[5], G. Beaudoin[18], A. Beck[23], G.A. Beck[13], J. Becker[10], C. Beeston[16], T. Behnke[27], K.W. Bell[20], G. Bella[23], P. Bentkowski[18], P. Berlich[10], S. Bethke[11], O. Biebel[3], I.J. Bloodworth[1], P. Bock[11], B. Boden[3], H.M. Bosch[11], M. Boutemeur[18], H. Breuker[8,b], P. Bright-Thomas[25], R.M. Brown[20], A. Buijs[8], H.J. Burckhart[8], C. Burgard[27], P. Capiluppi[2], R.K. Carnegie[6], A.A. Carter[13], J.R. Carter[5], C.Y. Chang[17], D.G. Charlton[8], S.L. Chu[4], P.E.L. Clarke[15], J.C. Clayton[1], I. Cohen[23], J.E. Conboy[15], M. Cooper[22], M. Coupland[14], M. Cuffiani[2], S. Dado[22], G.M. Dallavalle[2], S. De Jong[13], L.A. del Pozo[5], H. Deng[17], A. Dieckmann[11], M. Dittmar[4], M.S. Dixit[7], E. do Couto e Silva[12], J.E. Duboscq[8], E. Duchovni[26], G. Duckeck[11], I.P. Duerdoth[16], D.J.P. Dumas[6], P.A. Elcombe[5], P.G. Estabrooks[6], E. Etzion[23], H.G. Evans[9], F. Fabbri[2], B. Fabbro[21], M. Fierro[2], M. Fincke-Keeler[28], H.M. Fischer[3], D.G. Fong[17], M. Foucher[17], A. Gaidot[21], J.W. Gary[4], J. Gascon[18], N.I. Geddes[20], C. Geich-Gimbel[3], S.W. Gensler[9], F.X. Gentit[21], G. Giacomelli[2], R. Giacomelli[2], V. Gibson[5], W.R. Gibson[13], J.D. Gillies[20], J. Goldberg[22], D.M. Gingrich[30,a], M.J. Goodrick[5], W. Gorn[4], C. Grandi[2], F.C. Grant[5], J. Hagemann[27], G.G. Hanson[12], M. Hansroul[8], C.K. Hargrove[7], P.F. Harrison[13], J. Hart[8], P.M. Hattersley[1], M. Hauschild[8], C.M. Hawkes[8], E. Heflin[4], R.J. Hemingway[6], G. Herten[10], R.D. Heuer[8], J.C. Hill[5], S.J. Hillier[8], T. Hilse[10], D.A. Hinshaw[18], J.D. Hobbs[8], P.R. Hobson[25], D. Hochman[26], R.J. Homer[1], A.K. Honma[28,a], R.E. Hughes-Jones[16], R. Humbert[10], P. Igo-Kemenes[11], H. Ihssen[11], D.C. Imrie[25], A.C. Janissen[6], A. Jawahery[17], P.W. Jeffreys[20], H. Jeremie[18], M. Jimack[1], M. Jones[29], R.W.L. Jones[8], P. Jovanovic[1], C. Jui[4], D. Karlen[6], K. Kawagoe[24], T. Kawamoto[24], R.K. Keeler[28], R.G. Kellogg[17], B.W. Kennedy[15], J. King[13], S. Kluth[5], T. Kobayashi[24], D.S. Koetke[8], T.P. Kokott[3], S. Komamiya[24], J.F. Kral[8], R. Kowalewski[8], J. von Krogh[11], J. Kroll[9], P. Kyberd[13], G.D. Lafferty[16], H. Lafoux[21], R. Lahmann[17], J. Lauber[8], J.G. Layter[4], P. Leblanc[18], A.M. Lee[31], E. Lefebvre[18], M.H. Lehto[15], D. Lellouch[26], C. Leroy[18], J. Letts[4], L. Levinson[26], S.L. Lloyd[13], F.K. Loebinger[16], J.M. Lorah[17], B. Lorazo[18], M.J. Losty[7], X.C. Lou[12], J. Ludwig[10], A. Luig[10], M. Mannelli[8], S. Marcellini[2], C. Markus[3], A.J. Martin[13], J.P. Martin[18], T. Mashimo[24], P. Mättig[3], U. Maur[3], J. McKenna[29], T.J. McMahon[1], J.R. McNutt[25], F. Meijers[8], D. Menszner[11], F.S. Merritt[9], H. Mes[7], A. Michelini[8], R.P. Middleton[20], G. Mikenberg[26], J. Mildenberger[6], D.J. Miller[15], R. Mir[12], W. Mohr[10], C. Moisan[18], A. Montanari[2], T. Mori[24], M. Morii[24], U. Müller[3], B. Nellen[3], H.H. Nguyen[9], S.W. O'Neale[1], F.G. Oakham[7], F. Odorici[2], H.O. Ogren[12], C.J. Oram[28,a], M.J. Oreglia[9], S. Orito[24], J.P. Pansart[21], B. Panzer-Steindel[8], P. Paschievici[26], G.N. Patrick[20], N. Paz-Jaoshvili[23], M.J. Pearce[1], P. Pfister[10], J.E. Pilcher[9], J. Pinfold[30], D. Pitman[28], D.E. Plane[8], P. Poffenberger[28], B. Poli[2], T.W. Pritchard[13], H. Przysiezniak[18], G. Quast[27], M.W. Redmond[8], D.L. Rees[8], G.E. Richards[16], M. Rison[5], S.A. Robins[5], D. Robinson[8], A. Rollnik[3], J.M. Roney[28], E. Ros[8], S. Rossberg[10], A.M. Rossi[2], M. Rosvick[28], P. Routenburg[30], K. Runge[10], O. Runolfsson[8], D.R. Rust[12], M. Sasaki[24], C. Sbarra[2], A.D. Schaile[26], O. Schaile[10], W. Schappert[6], F. Scharf[3], P. Scharff-Hansen[8], P. Schenk[4], B. Schmitt[3], H. von der Schmitt[11], M. Schröder[12], C. Schwick[27], J. Schwiening[3], W.G. Scott[20], M. Settles[12], T.G. Shears[5], B.C. Shen[4], C.H. Shepherd-Themistocleous[7], P. Sherwood[15], G.P. Siroli[2], A. Skillman[16], A. Skuja[17], A.M. Smith[8], T.J. Smith[28], G.A. Snow[17], R. Sobie[28], R.W. Springer[17], M. Sproston[20], A. Stahl[3], C. Stegmann[10], K. Stephens[16], J. Steuerer[28], R. Ströhmer[11], D. Strom[19], H. Takeda[24], T. Takeshita[24,c], S. Tarem[26], M. Tecchio[9], P. Teixeira-Dias[11], N. Tesch[3], M.A. Thomson[15], E. Torrente-Lujan[22], S. Towers[28], G. Transtromer[25], N.J. Tresilian[16], T. Tsukamoto[24], M.F. Turner[8], D. Van den plas[18], R. Van Kooten[27], G.J. VanDalen[4], G. Vasseur[21], A. Wagner[27], D.L. Wagner[9], C. Wahl[10], C.P. Ward[5], D.R. Ward[5], J.J. Ward[15], P.M. Watkins[1], A.T. Watson[1], N.K. Watson[8], M. Weber[11], P. Weber[6], P.S. Wells[8], N. Wermes[3], M.A. Whalley[1], B. Wilkens[10], G.W. Wilson[4], J.A. Wilson[1], V-H. Winterer[10], T. Wlodek[26], G. Wolf[26], S. Wotton[11], T.R. Wyatt[16], R. Yaari[26], A. Yeaman[13], G. Yekutieli[26], M. Yurko[18], W. Zeuner[8], G.T. Zorn[17].

[1]School of Physics and Space Research, University of Birmingham, Birmingham, B15 2TT, UK
[2]Dipartimento di Fisica dell' Università di Bologna and INFN, Bologna, 40126, Italy
[3]Physikalisches Institut, Universität Bonn, D-5300 Bonn 1, Germany
[4]Department of Physics, University of California, Riverside, CA 92521 USA
[5]Cavendish Laboratory, Cambridge, CB3 0HE, UK
[6]Carleton University, Dept of Physics, Colonel By Drive, Ottawa, Ontario K1S 5B6, Canada
[7]Centre for Research in Particle Physics, Carleton University, Ottawa, Ontario K1S 5B6, Canada
[8]CERN, European Organisation for Particle Physics, 1211 Geneva 23, Switzerland
[9]Enrico Fermi Institute and Dept of Physics, University of Chicago, Chicago Illinois 60637, USA
[10]Fakultät für Physik, Albert Ludwigs Universität, D-7800 Freiburg, Germany
[11]Physikalisches Institut, Universität Heidelberg, Heidelberg, Germany
[12]Indiana University, Dept of Physics, Swain Hall West 117, Bloomington, Indiana 47405, USA
[13]Queen Mary and Westfield College, University of London, London, E1 4NS, UK
[14]Birkbeck College, London, WC1E 7HV, UK
[15]University College London, London, WC1E 6BT, UK
[16]Department of Physics, Schuster Laboratory, The University, Manchester, M13 9PL, UK

[17]Department of Physics, University of Maryland, College Park, Maryland 20742, USA
[18]Laboratoire de Physique Nucléaire, Université de Montréal, Montréal, Quebec, H3C 3J7, Canada
[19]University of Oregon, Dept of Physics, Eugene, Oregon 97403, USA
[20]Rutherford Appleton Laboratory, Chilton, Didcot, Oxfordshire, OX11 0QX, UK
[21]DAPNIA/SPP, Saclay, F-91191 Gif-sur-Yvette, France
[22]Department of Physics, Technion-Israel Institute of Technology, Haifa 32000, Israel
[23]Department of Physics and Astronomy, Tel Aviv University, Tel Aviv 69978, Israel
[24]International Centre for Elementary Particle Physics and Dept of Physics, University of Tokyo, Tokyo 113, and Kobe University, Kobe 657, Japan
[25]Brunel University, Uxbridge, Middlesex, UB8 3PH UK
[26]Nuclear Physics Department, Weizmann Institute of Science, Rehovot, 76100, Israel
[27]Universität Hamburg/DESY, II Inst für Experimental Physik, Notkestrasse 85, 22607 Hamburg, Germany
[28]University of Victoria, Dept of Physics, P O Box 3055, Victoria BC V8W 3P6, Canada
[29]University of British Columbia, Dept of Physics, Vancouver BC V6T 1Z1, Canada
[30]University of Alberta, Dept of Physics, Edmonton AB T6G 2N5, Canada
[31]Duke University, Dept of Physics, Durham, North Carolina 27708-0305, USA

[a]Also at TRIUMF, Vancouver, Canada V6T 2A3
[b]Now at MPI, München, Germany
[c]Also at Shinshu University, Matsumoto 390, Japan

1 Introduction

This paper reports measurements of the F_2^γ hadronic structure function of the photon at intermediate Q^2 ($4 < Q^2 < 30$ GeV^2) using data taken by the OPAL experiment at LEP in the period 1990-1992. The data sample corresponds to an integrated e^+e^- luminosity of 44.8 pb^{-1}. The analysis uses singly-tagged events, with the tagged $e^\pm$ detected at angles between 47 and 120 mrad to the beam direction.

Witten's original proposal [1] that F_2^γ would evolve with Q^2 according to perturbative QCD has been confirmed by experiments at lower energy e^+e^- colliders which [2-9] have measured $F_2^\gamma(x)$ with $<Q^2>$ ranging from 0.1 GeV^2 to 500 GeV^2. However, the use of that evolution to extract an unambiguous value for the scale parameter $\Lambda_{\overline{MS}}$ has been plagued with theoretical uncertainties [10-14].

The TPC/2γ experiment [2] demonstrated that at low Q^2 (< 1.5 GeV^2) the target photon behaves like a vector meson, with the x dependence of F_2^γ agreeing well with the pion structure function as studied in Drell Yan processes [15]; as an S-wave state, the π is expected to be a good model for the ρ structure function [16].

A number of experiments with data at a mean Q^2 of $\sim$ 5 GeV^2 [3, 4] show that $F_2^\gamma(x)$ begins to grow for $x > 0.3$, as predicted by QCD, but the transformation from $Q^2 \sim 1$ GeV^2 to $Q^2 \sim 5$ GeV^2 is so abrupt that it has been difficult to devise a model which fits both regions [17-20]. The OPAL data reported here confirm previous results on the upper side of this abrupt transformation.

2 The Opal Detector

The OPAL detector, described in detail elsewhere [21], has a uniform solenoidal magnetic field of 0.4 T throughout the central tracking region, with electromagnetic and hadronic calorimetry outside the coil. For this analysis the most important sub-detectors are the Forward Detectors, the Central Jet and Vertex Chambers which trigger on and measure charged tracks, and the lead-glass Electromagnetic Barrel and Endcap Calorimeters.

The Forward Detectors are used to tag leptons which have made deep-inelastic scatters with nearly-real photons radiated by particles in the opposing beam (see discussion in Section 3). These detectors, which cover the small-angle region at each end of OPAL, consist of cylindrical lead-scintillator calorimeters with a depth of 24 radiation lengths (X_0) divided azimuthally into 16 segments. The energy resolution is $18\%/\sqrt{E}$, where E is in GeV. Positional information is derived from the energy sharing between adjacent segments, and by the sharing of light between the inner and outer edges of each segment. An array of three planes of proportional tubes buried in the calorimeter at a depth of $4X_0$ provides a better shower position measurement, with a typical resolution of 3-4 mm, corresponding to 2.5 mrad in the polar angle ϑ, and less than 3.5 mrad in the azimuthal angle ϕ. The clear acceptance of the Forward Detectors covers the angular range from 47 to 120 mrad from the beam direction.

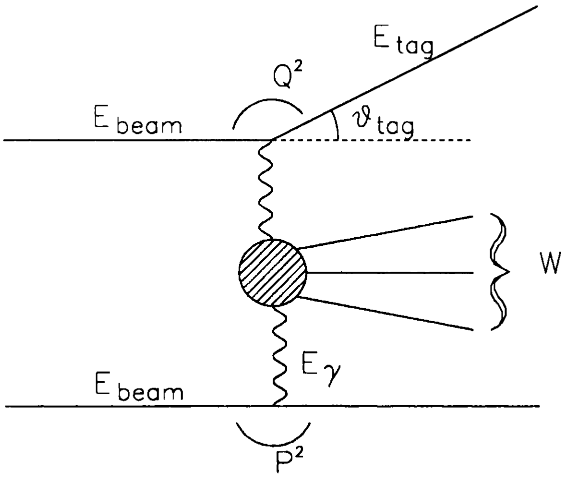

Figure 1: The multiperipheral two-photon process.

3 Kinematics

The cross section for deep inelastic scattering of an $e^{\pm}$ from a nearly real virtual photon associated with the opposing $e^{\mp}$ can be written in terms of the structure functions $F_1^{\gamma}(x, Q^2)$ and $F_2^{\gamma}(x, Q^2)$ as [22]

$$\frac{d^2\sigma}{dxdy} = \frac{16\pi\alpha^2 E_{beam} E_{\gamma}}{Q^4}[(1-y)F_2^{\gamma}(x,Q^2) + xy^2 F_1^{\gamma}(x,Q^2)] \tag{1}$$

where the kinematic variables are defined with reference to Figure 1. E_{beam} is the incoming beam energy and E_{γ} the energy of the target photon. Q^2, x, and y are given by

$$\begin{aligned} Q^2 &= 2E_{beam}E_{tag}(1-\cos\vartheta_{tag}), & (2)\\ x &= \frac{Q^2}{Q^2+W^2}, & (3)\\ y &= 1-\frac{E_{tag}}{E_{beam}}\cos^2(\vartheta_{tag}/2), & (4)\end{aligned}$$

where E_{tag} is the energy of the tagged $e^{\pm}$ and ϑ_{tag} is its angle to the beam direction. W is the invariant mass of the two-photon system which gives rise to the final-state hadrons in this analysis. Because of the loss of particles near the beam pipe, W is not directly measurable. We define W_{trk} to be the invariant mass of the charged tracks, while W_{vis} is the mass of all of the hadrons seen in the detector. The quantities x_{trk} and x_{vis} are defined by adding the appropriate subscripts to (3). In testing the Monte Carlo program (see Section 5 below), we also use the variable P^2, the four-momentum transfer squared to the untagged lepton, defined analogously to Q^2. In the kinematic region considered here, $y \ll 1$, so that the second term in (1) is much smaller than the first and the measured cross section is effectively proportional to $F_2^\gamma(x, Q^2)$.

4 Event Selection Criteria

The event selection cuts require a high-energy cluster (the tag) in the Forward Detector, in association with charged tracks detected in the Central Detectors. The selection cuts are summarised in Table 1, and are discussed in more detail in this section.

The measured energy must be at least $0.775 \times E_{beam}$, to exclude backgrounds arising from multihadronic Z^0 decays, and from untagged two-photon events coincidentally associated with fake tags caused by off-momentum beam particles. Figure 2 shows the distribution of events in E_{tag}/E_{beam} and the normalised transverse momentum k_T, defined by

$$k_T = ({p_T}^{tag} + {p_T}^{vis})/{p_T}^{tag}.$$

Here ${p_T}^{tag}$ is the transverse momentum of the tagged lepton with respect to the beam axis, and ${p_T}^{vis}$ is the component of the total transverse momentum of the other observed particles in the plane defined by the beam and the tagged lepton (the "tag plane"). In this plane, ${p_T}^{tag}$ defines the positive direction, while ${p_T}^{vis}$ can have either sign. The events plotted pass all of our selection cuts, except that no tag energy or transverse momentum cuts have been applied. The tagged two-photon signal is represented by the cluster of events centred close to $k_T = 0$ which is visible at high E_{tag}/E_{beam}; the background events appear at lower E_{tag}/E_{beam}, and have a much flatter distribution in k_T.

In addition to the tag energy cut,we restrict the measured angle of the tag cluster to ensure that the shower is completely contained in the Forward Detector. Events where both leptons are detected at large angles are rejected, to ensure that the target photon is close to the mass shell.

Only events having at least three reconstructed charged tracks are accepted. We demand that W_{vis} be greater than 2.5 GeV, so that the accepted events are well above the hadronic resonance region, and make cuts on the transverse momentum of the charged tracks, both in and out of the tag plane.

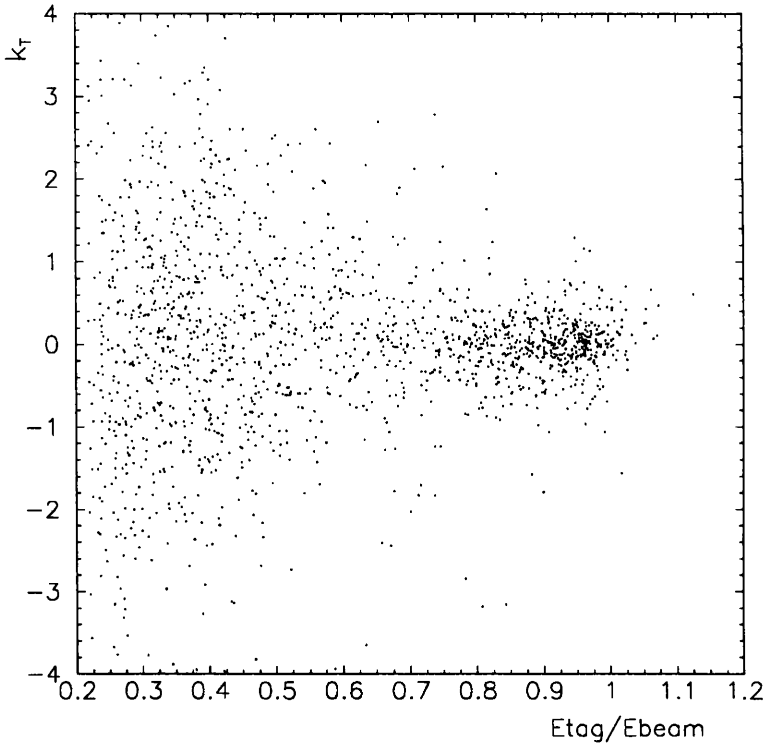

Figure 2: Distribution of events in scaled transverse momentum k_T and E_{tag}/E_{beam}.

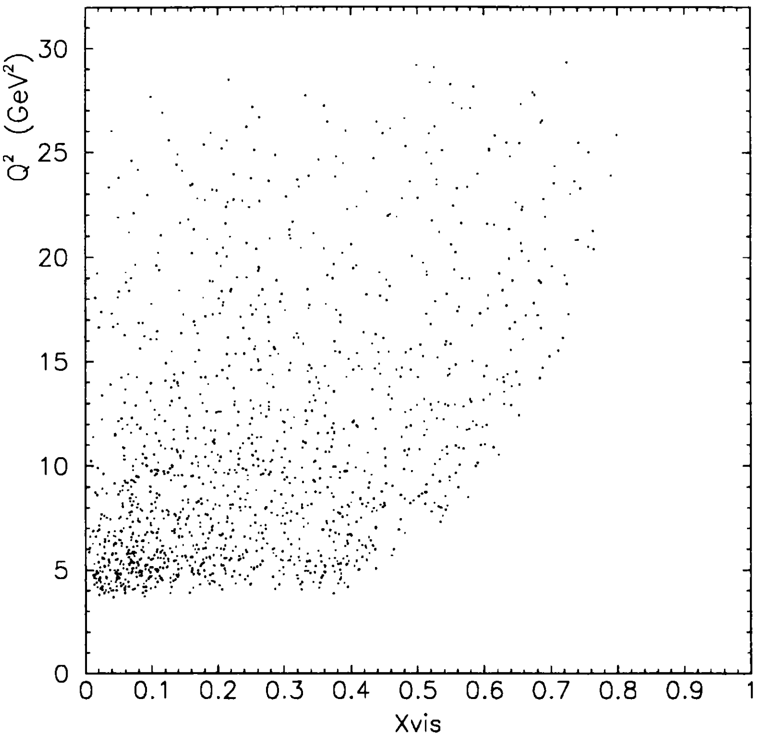

Figure 3: Distribution of selected events in x_{vis} and Q^2.

A total of 1350 events pass all of the cuts, of which 555 have $Q^2 < 8$ GeV^2, and 795 have $Q^2 > 8$ GeV^2. The distribution of these events in the $x_{vis} - Q^2$ plane is shown in Figure 3.

Several independent calorimetric and track-based triggers contribute to the final event sample. The resulting redundancy enables us to determine the overall trigger efficiency to be $99.0 \pm 0.2\%$.

5 Monte Carlo Simulation

Many of the hadrons in tagged two-photon events are produced at small angles to the incoming e$^+$e$^-$ beam axis, and remain undetected in the beam pipe. Consequently, it is important that the Monte Carlo model accurately represents the data and the detector, to permit the effects of finite detector acceptance and resolution to be unfolded (see Section 8.1). The OPAL detector simulation program is described in detail elsewhere [23]. This section describes the event generators used in this analysis.

We use a new Monte Carlo program TWOGEN [24] to generate events according to chosen formulae for $F_2^\gamma(x, Q^2, P^2)$ or $F_2^\gamma(x, Q^2)$. TWOGEN is based on the transverse-transverse two-photon luminosity generator developed by Langeveld [25] for analysis of two-photon data from the TPC/2γ experiment. A quark-antiquark state is generated with mass W and a quark-parton model (QPM) angular distribution in the two-photon centre of mass, and is allowed to fragment by using the Lund string model [26, 27].

As a check, TWOGEN has been compared with the predictions of the QED matrix-element Monte Carlo program of Vermaseren [28, 29, 30], with quark masses, charges and colours set to reproduce QPM. For the purposes of this comparison, we used the QPM formula for $F_2^\gamma(x, Q^2, P^2)$ [31]. The two programs agree to within 1.4% in overall normalization, which is assigned as a systematic error in the normalization of the unfolded structure function.

In generating samples for comparison with the data a number of contributions must be combined.

a) QCD. There are numerous formulae which could be used in TWOGEN. We have chosen the "all order QCD" approach of Kapusta et al. [12, 13, 32], as parametrized in [9], with the QCD scale parameter Λ taken to be 200 MeV. The change in the behaviour of the structure function at Q^2 close to 1 GeV^2 is built into this model by setting a cutoff in p_t, the transverse momentum of the virtual quark with respect to the photon axis in the two-photon centre-of-mass frame. The pointlike behaviour of the QCD formula is assumed to apply to all $p_t > p_t^0$, but a separate part must be added to the cross section to allow for the hadron-like behaviour of the target photon for $p_t < p_t^0$. This extra contribution is parametrized by the Vector Meson Dominance model.

b) VMD. The Vector Meson Dominance contribution is calculated using the TWOGEN Monte Carlo with a structure function formula which has been shown to fit data at $Q^2 < 1$ GeV^2 [2, 3]. We have verified that our results do not change significantly if we use the simpler expression $F_2^\gamma(x)/\alpha = 0.2(1 - x)$ [22] instead. Following [2, 3], we consider two VMD models, with different angular distributions of the quark-antiquark axis in the two-photon centre-of-mass frame. The weight given to each model in our final Monte Carlo sample is adjusted to achieve the best fit to the data (cf. Section 7.1). In model A (VMD "peripheral"), we generate the angular distribution according to an exponential distribution of quark transverse momentum with a mean of 300 MeV with respect to the photon axis. Model B produces the angular distribution of QED fermion pair production by real photons. We generated this sample using the same VMD structure function as in model A, followed by a sampling from the same "fermion pair" quark angular distribution as was used for the QCD events.

c) Charmed quark and tau lepton production. Events in both of these channels are generated with the Vermaseren Monte Carlo, i.e. assuming that the heavy quark behaves according to QPM at these modest Q^2 values, and that the tau lepton behaves according to QED.

Events from all five Monte Carlo samples (QCD, VMD model A, VMD model B, charm-anticharm and tau-antitau) are passed through the OPAL simulation program [23] and reconstructed in the same way as real data. They are then analysed with the same selection criteria as the real sample. The number of events in each category passing all of the two-photon selection cuts is given in Table 2. The total sample generated corresponded to approximately five times our actual integrated e^+e^- luminosity; the figures in the table have been normalized to 44.8 pb^{-1}.

We have corrected for the finite range of target-photon masses allowed by our antitagging cut by comparing a sample of Monte Carlo events from the TWOGEN program using the P^2-dependent version of the QPM formula for F_2^γ [31] with a sample generated using a P^2-independent QPM formula [1]. The cross section within our acceptance is 5% smaller when integrated over the accepted range of P^2, as compared to the calculation with $P^2 = 0$. There is also a small change in the shape of the x distribution. These corrections are only applied to the QCD component of the Monte Carlo as it is not obvious that this comparison, calculated from the quark parton model, should apply to the VMD component of our data. The $c\bar{c}$ and $\tau^+\tau^-$ components generated with the Vermaseren program already include a P^2 dependence.

6 Estimation of Backgrounds

In addition to the $e^+e^-\tau^+\tau^-$ final state mentioned above, the following processes give rise to background events.

6.1 $e^+e^- \to$ hadrons

There is a small probability that a hadronic Z^0 decay could satisfy the two-photon selection criteria. The resonant enhancement at the Z^0 peak makes this problem potentially more serious at LEP than at previous e^+e^- colliders. We have investigated this using Monte Carlo events simulated with the Jetset73 package [33]. Our selection cuts reject these events very effectively, giving the background estimates shown in Table 3.

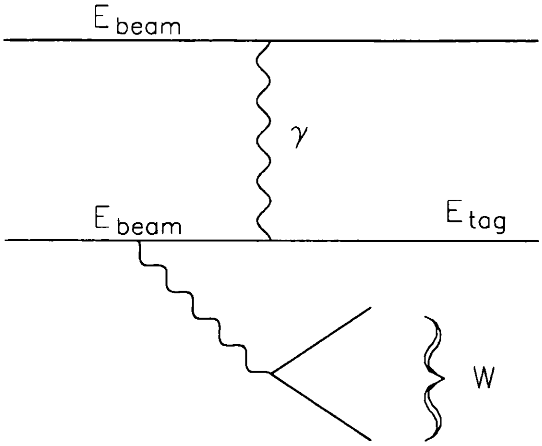

Figure 4: The bremsstrahlung background process.

6.2 $e^+e^- \rightarrow \tau^+\tau^-$

As in the hadronic case, tau pairs produced in Z^0 decay can in principle fake tagged two-photon events. An analysis of 72000 such events produced with the KORALZ generator [34] found no events satisfying our selection cuts. Since this Monte Carlo sample corresponds to an integrated luminosity of approximately 1.2 times that used in this analysis, the background from $Z^0 \rightarrow \tau^+\tau^-$ events is expected to be negligible.

6.3 Non-multiperipheral $e^+e^- \rightarrow e^+e^-$ + hadrons

There are several processes other than the multiperipheral diagram of Figure 1 which can give rise to the same final state. These processes have been studied using the Monte Carlo generator FERMISV [35], which incorporates both Z^0 and γ exchange diagrams and interference terms. By far the largest contribution arises from the bremsstrahlung, or "inelastic Compton", process shown in Figure 4. The resulting background is estimated as $(0.4 \pm 0.2)\%$ of the multiperipheral cross section, or 5.4 ± 2.7 events, the error being the Monte Carlo statistical uncertainty.

The Q^2 distribution of these events follows that of the multiperipheral sample; they are uniformly distributed in x between the values of 0.2 and 0.7. The effect of interference between the multiperipheral and bremsstrahlung diagrams is found to be much less than the bremsstrahlung cross section and can safely be neglected.

6.4 Beam-gas events

Background events arising from interactions with residual gas in the beam pipe would have their vertex position uniformly distributed along the beam axis. By studying events originating outside our ±10 cm cut, we estimate that our final sample contains 3.0 ± 0.9 such events. Events in which an off-momentum electron simulates a Forward Detector tag have been studied as part of the OPAL luminosity determination [36, 37]; such events are clustered at low "tag" energies, as shown in Figure 2, and can be neglected at $E_{tag} > 0.775 \times E_{beam}$.

7 Results of the Analysis

7.1 Fit for the QCD cutoff parameter p_t^0.

The transverse momentum cutoff p_t^0 in the QCD model for F_2^γ [12, 13, 32] has been determined by fitting the Monte Carlo x_{vis} distribution to the data (Figures 5 and 6). The Monte Carlo samples from QCD, VMD model A, charm and tau pairs were individually normalized to the observed luminosity, then added together and the backgrounds subtracted, leaving only p_t^0 to be varied.

The results of the fits are given in Table 4. The central values of p_t^0 in the two Q^2 ranges are consistent with the value of 0.27 ± 0.10 obtained by fitting over the whole data set.

In order to test whether a model B component is needed in the VMD Monte Carlo sample, as discussed in Section 5, we examined the event distributions in Q^2, ϑ_{tag}, and $(p_T^{lead})^2$, where p_T^{lead} is the momentum component perpendicular to the tag plane of the hadron with the highest momentum. In each case, the data is best represented when the VMD event sample is 100% model A.

7.2 Comparison of data and Monte Carlo distributions

The event distributions in Q^2, E_{tag}, and ϑ_{tag} (Figure 7) demonstrate that the tagged leptons are reasonably well described by the Monte Carlo with p_t^0 determined as described above. The disagreement between the data and the simulation

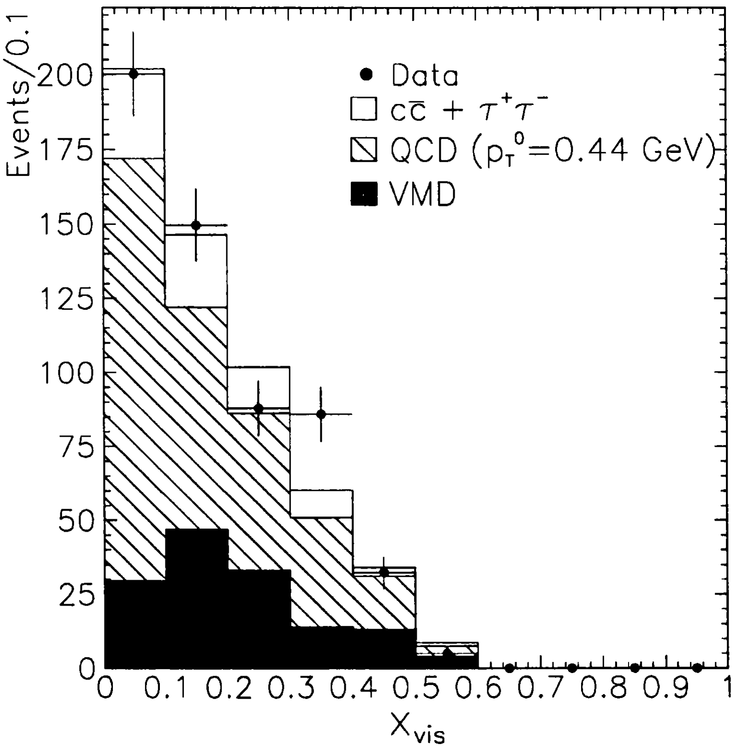

Figure 5: Comparison of data and Monte Carlo x_{vis} distributions, for $4 < Q^2 < 8$ GeV^2. The unshaded part of the histogram represents $\tau^+\tau^-$ and $c\bar{c}$ events.

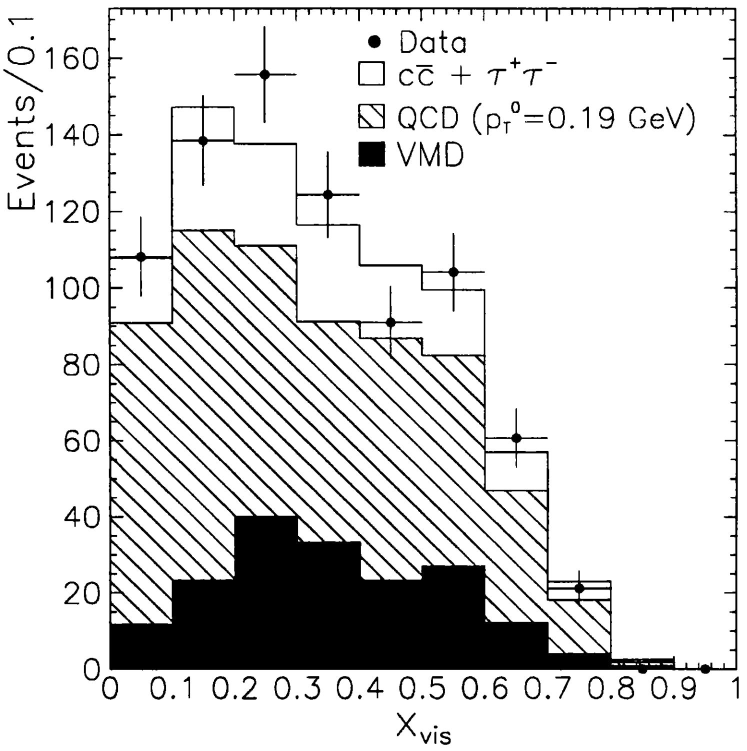

Figure 6: Comparison of data and Monte Carlo x_{vis} distributions, for $8 < Q^2 < 30$ GeV^2. The unshaded part of the histogram represents $\tau^+\tau^-$ and $c\bar{c}$ events.

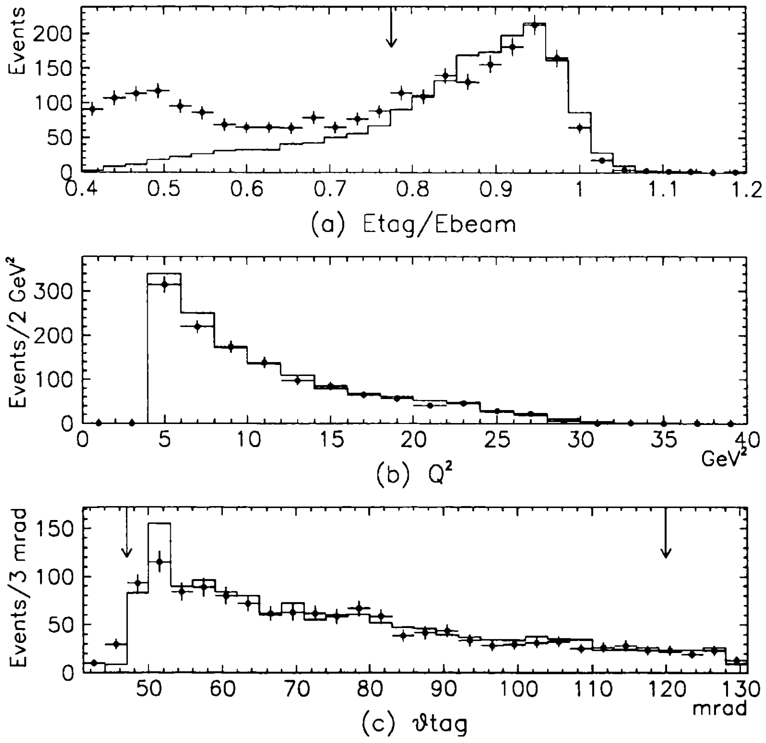

Figure 7: Comparison of data and Monte Carlo tag distributions. The points are the data, and the lines show the Monte Carlo prediction. The arrows represent the selection cuts, detailed in Table 1.

at low tag energies is principally caused by the classes of background discussed in Section 4 above. The discrepancy at $\vartheta_{tag} \sim 52$ mrad in Figure 7(c) occurs at the edge of the acceptance of the proportional tube counters. This effect is not perfectly modelled by the detector simulation, leading to the depletion of Monte Carlo events at low ϑ_{tag}, compensating for the excess in the 52 mrad bin. In variables of physical interest, in particular x_{vis}, this local imperfection is not significant. Figure 8 shows variables which depend upon the simulation of the hadronic final state. The agreement is acceptable for our purposes. However, there are significant discrepancies in regions of the plots sensitive to the fact that the Lund fragmentation scheme is known not to be reliable for hadron systems with mass W close to the lower cut at 2.5 GeV. The resulting systematic errors are discussed below.

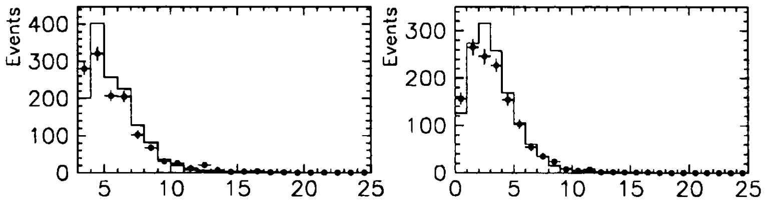

(a) Charged multiplicity (b) Neutral multiplicity

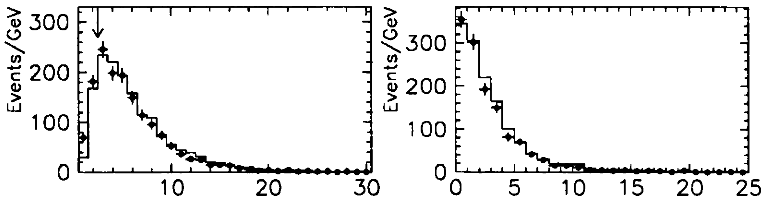

(c) Wvis (d) Neutral Energy

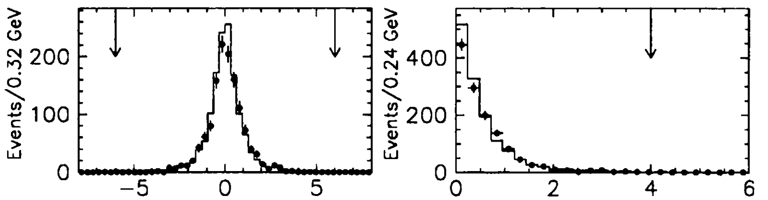

(e) Total p_T in tag plane (f) Total p_T out of tag plane

Figure 8: Comparison of data and Monte Carlo hadronic distributions. The points are the data, and the lines show the Monte Carlo prediction. The arrows represent the selection cuts, detailed in Table 1.

8 Measurement of the F_2^γ structure function

8.1 Unfolding the detector effects

In order to obtain a measurement of F_2^γ which can be compared with theoretical calculations and results from other experiments, we correct for the finite detector acceptance and resolution effects using the unfolding program of Blobel [38] to transform the measured x_{vis} distribution into the estimated $F_2^\gamma(x)$ in true x space. This program avoids the statistical instabilities inherent in the naïve "matrix inversion" technique which can give rise to bin-to-bin correlations and unphysical fluctuations in the unfolded result (see [38] for details). The systematic errors arising from the unfolding procedure are discussed below.

Our unfolded measurements of $F_2^\gamma(x)$ are shown in Figure 9 for the Q^2 region $4 < Q^2 < 8$ GeV^2, and in Figure 10 for $8 < Q^2 < 30$ GeV^2. Also shown for comparison are earlier results obtained by the PLUTO [4] and TPC/2γ [2] collaborations at comparable $<Q^2>$. The curves show the prediction of the QCD model of [12, 13, 32] including the VMD contribution, evaluated for the Q^2 range covered by the OPAL data. Our results are consistent with the other experiments in the respective Q^2 regions and agree well with the model.

The unfolded measurements and associated errors are summarised in Tables 5 and 6. The systematic errors shown in the tables are discussed below.

Figure 11 shows the variation in the mean value of F_2^γ/α for $0.3 < x < 0.8$, as a function of Q^2. The lower integration limit ensures that the effect of the VMD contribution is small, while the upper limit is required because the statistical errors increase rapidly in most experiments as $x \to 1$. The present OPAL data points are shown as solid circles. The lines show the predictions of the QCD model of refs [12, 13, 32] for several values of the cutoff parameter p_t^0.

8.2 Systematic errors

Several sources of systematic error have been considered, as follows.

(a) Variation of cuts. We have repeated the analysis with the tag energy cut altered by $\pm 0.025 \times E_{beam}$ and $\pm 0.050 \times E_{beam}$ from its standard value; this represents 1× and 2× the energy resolution of the Forward Detector. Similarly, we have varied the cut on W_{vis} between 2 GeV and 3 GeV in steps of 0.25 GeV, and analysed the data using only charged track information. From the RMS variation of unfolded results a point by point systematic error was assigned as given in Tables 5 and 6. The errors from this source are less than the statistical errors on all points, except for the lowest x point in the upper range of Q^2.

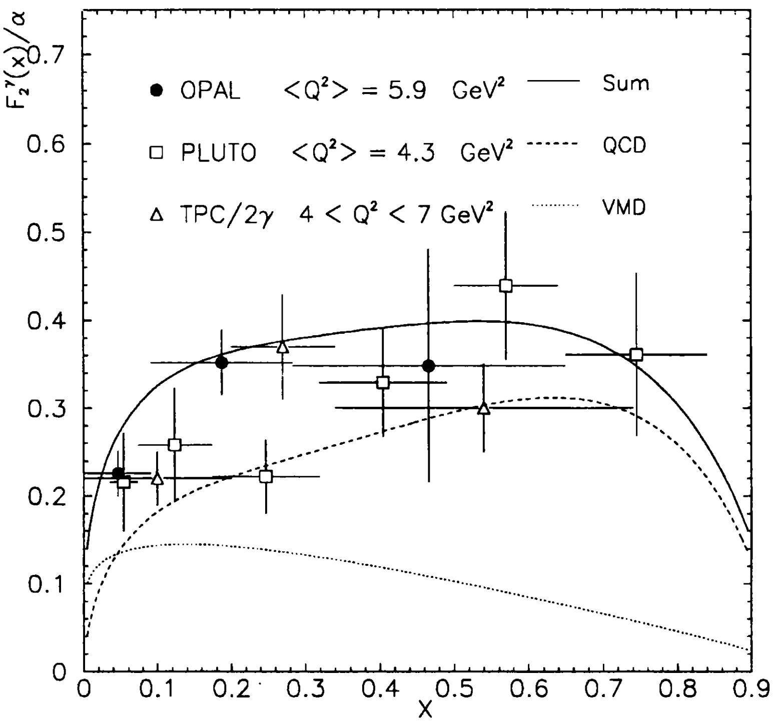

Figure 9: Unfolded $F_2^\gamma(x)$at $<Q^2> = 5.9\,\mathrm{GeV}^2$, with previous measurements at similar mean Q^2 shown for comparison. The curves show the predictions of a QCD-based model (see text). The error bars give the statistical and systematic errors added in quadrature.

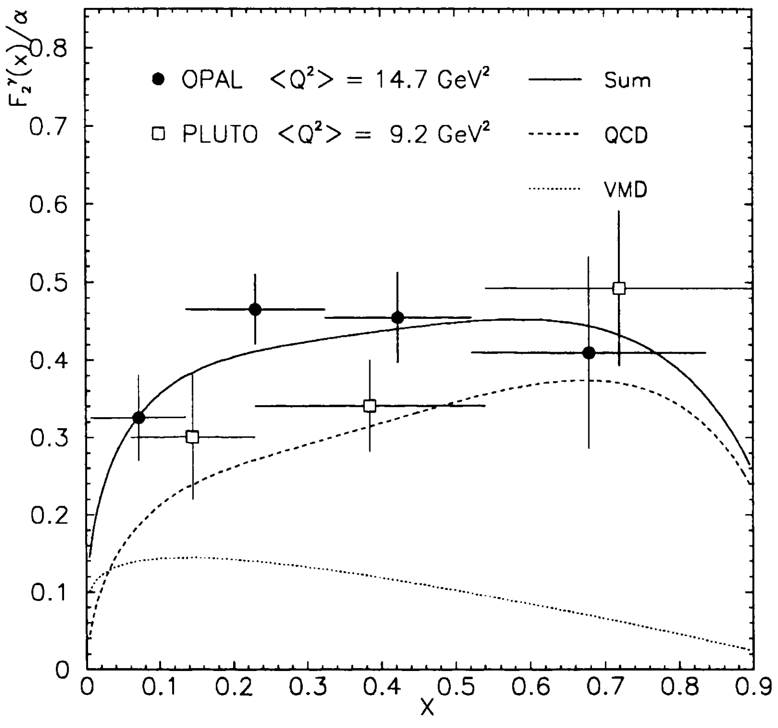

Figure 10: Unfolded $F_2^\gamma(x)$at $<Q^2> = 14.7$ GeV^2, with a previous measurement at similar mean Q^2 shown for comparison. The curves show the predictions of a QCD-based model (see text). The error bars give the statistical and systematic errors added in quadrature.

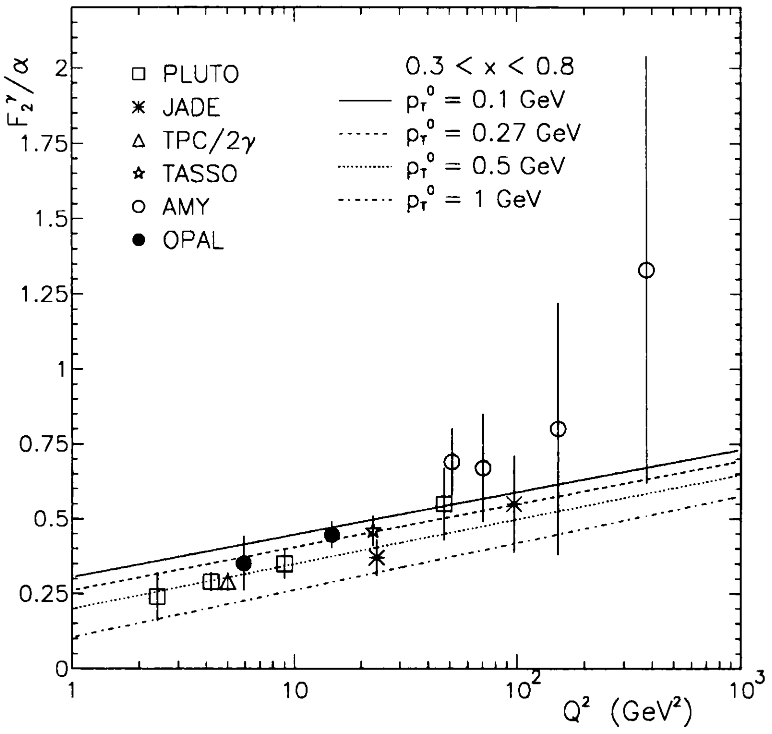

Figure 11: Variation of $<F_2^\gamma(x)>$ with Q^2 (adapted from [9]).

The discrepancy between the charged multiplicity distribution in the data and the prediction of our Monte Carlo model, seen in Figure 8(a), means that the normalization of F_2^γ is sensitive to the cut on the number of charged tracks. We have studied the variation in the mean value of the unfolded $F_2^\gamma(x)$ as the minimum charged multiplicity varies from 3 to 5 tracks. The RMS variation is 5.4%, which we assign as a systematic error common to all x points.

The measurements of $F_2^\gamma(x)$ are insensitive to variations of the other cuts.

(b) Variation of unfolding parameters. The unfolding procedure handles the data internally in the form of binned histograms. For our main analysis, we chose a bin size giving a mean of approximately 20 events per bin; this required roughly 30 bins in each Q^2 range. The systematic error under the heading of "unfolding" in Tables 5 and 6 has been estimated by repeating the analysis with the number of bins varying between 10 and 60 and calculating the RMS variation of each point of the unfolded structure function. None of the unfolded points is sensitive to such variations, except the high-x point in the low Q^2 region. Even in this case the systematic change is within the statistical error.

(c) Radiative corrections. The TWOGEN Monte Carlo program makes no provision for initial state radiation. Calculations using the FERMISV generator [35] suggest that initial state radiation decreases the cross section for the multi-peripheral two-photon process by $(2.7 \pm 1.8)\%$ in comparison to the lowest-order diagram. We therefore decrease the normalization of our measured F_2^γ by this amount, and assign 1.8% as a systematic error.

(d) Monte Carlo systematics. As mentioned above, we estimate a systematic error of 1.4% on the overall normalization of F_2^γ by comparing the TWOGEN Monte Carlo generator with the Vermaseren program. This incorporates the error on the correction for P^2 being non-zero.

(e) Other errors. The precision of the luminosity measurement has been steadily improved, from 0.85% in 1990 to 0.5% in 1992; these errors include theoretical uncertainties in the Bhabha scattering cross section. As most of our data were taken in 1991 and 1992, we assign a systematic error of 0.6% from this source. The 0.2% error on the trigger efficiency is negligible. The effect of backgrounds has been shown to be small; the associated systematic errors have been neglected.

9 Conclusions

We have measured the hadronic photon structure function $F_2^\gamma(x)$ in two ranges of Q^2 with means of 5.9 GeV^2 and 14.7 GeV^2. Our measurements are consistent in shape and absolute normalization with those obtained in previous experiments with similar mean Q^2, and with the predictions of a QCD-based phenomenological model in which a soft hadronic component is added to account for collisions in which the quarks in the target photon have transverse momentum less than approximately 270 MeV. We confirm that a significant pointlike component of the photon is present when the probing photon has $Q^2 > 4$ GeV^2.

Our measurements extend to lower values of x than previous experiments have achieved, particularly in the higher Q^2 range, where we have data below $x = 0.01$. There is no indication that $F_2^\gamma(x)$ increases in this region.

Acknowledgements:

It is a pleasure to thank the SL Division for the efficient operation of the LEP accelerator, the precise information on the absolute energy, and their continuing close cooperation with our experimental group. In addition to the support staff at our own institutions we are pleased to acknowledge the
Department of Energy, USA,
National Science Foundation, USA,
Texas National Research Laboratory Commission, USA,
Science and Engineering Research Council, UK,
Natural Sciences and Engineering Research Council, Canada,
Fussefeld Foundation,
Israeli Ministry of Energy and Ministry of Science,
Minerva Gesellschaft,
Japanese Ministry of Education, Science and Culture (the Monbusho) and a grant under the Monbusho International Science Research Program,
German Israeli Bi-national Science Foundation (GIF),
Direction des Sciences de la Matière du Commissariat à l'Energie Atomique, France,
Bundesministerium für Forschung und Technologie, Germany,
National Research Council of Canada,
A.P. Sloan Foundation, and Junta Nacional de Investigação Científica e Tecnológica, Portugal.

References

[1] E. Witten, Nucl. Phys. B120, (1977) 189.

[2] H. Aihara et al., TPC/2γ Collaboration, Z. Phys. C 34, (1987) 1.

[3] H. Aihara et al., TPC/2γ Collaboration, Phys. Rev. Lett. 58, (1987) 97.

[4] Ch. Berger et al., PLUTO Collaboration, Phys. Lett. 142, (1984) 111.

[5] Ch. Berger et al., PLUTO Collaboration, Nucl. Phys. B281, (1987) 365.

[6] M. Althoff et al., TASSO Collaboration, Z. Phys. C, 31, (1986) 527.

[7] W. Bartel et al., JADE Collaboration, Z. Phys. C, 24, (1984) 231.

[8] H.-J. Behrend et al., CELLO Collaboration, Phys. Lett. 126B, (1983) 391.

[9] T. Sasaki et al., AMY Collaboration, Phys. Lett. B252, (1990) 491.

[10] W. A. Bardeen and A. J. Buras, Phys. Rev. D20, (1979) 166.

[11] D. W. Duke and J. F. Owens, Phys. Rev. D22, (1980) 2280.

[12] J. H. Field, F. Kapusta and L. Poggioli, Phys. Lett. 181B, (1986) 362.

[13] J. H. Field, F. Kapusta and L. Poggioli, Z. Phys. C 36, (1987) 121.

[14] W. R. Frazer, Phys. Lett. B194, (1987) 287.

[15] J. Badier et al., NA3 Collaboration, Z. Phys. C. 18, (1983) 281.

[16] C. Peterson et al., Nucl Phys B174, (1980) 424.

[17] J. H. da Luz Viera and J. K. Storrow, Phys. Lett. B205,(1988) 367.

[18] J. H. da Luz Viera and J. K. Storrow, Phys. Lett. B219, (1989) 529.

[19] J. H. da Luz Viera and J. K. Storrow, Z. Phys. C 51 (1991) 241.

[20] J. Field, P349; Proceedings of VIII International Workshop on Photon-Photon Collisions, Shoresh, Jerusalem Hills, 24-28 April 1988; ed. U. Karshon, World Scientific, Singapore.

[21] K. Ahmet et al., The OPAL Collaboration, Nucl. Inst. Meth. A305, (1991) 275.

[22] H. Kolanoski: "Two Photon Physics at e^+e^-Storage Rings", Springer Verlag (Berlin) 1984.

[23] J. Allison et al., Nucl. Inst. Meth. A317, (1992) 47.

[24] "TWOGEN, a Monte Carlo Generator for Two-Photon Reactions", A. Buijs et al., to be published.

[25] W. G. J. Langeveld, "Pion and Kaon Pair-Production in Photon-Photon Collisions." PhD. thesis, University of Utrecht (1985).

[26] T. Sjöstrand, Comp. Phys. Comm. 47, (1987) 347.

[27] T. Sjöstrand and M. Bengtsson, Comp. Phys. Comm. 43, (1987) 357.

[28] R. Battacharya, G. Grammer Jr., J. Smith, and J.A.M. Vermaseren, Phys. Rev. D15, (1977) 3267.

[29] R. Battacharya, G. Grammer Jr., J. Smith, and J.A.M. Vermaseren, Phys. Rev. D15, (1977) 3280.

[30] R. Battacharya, G. Grammer Jr., J. Smith, and J.A.M. Vermaseren, Phys. Rev. D19, (1979) 137.

[31] C. J. Hill and G. G. Ross, Nucl. Phys. B148, (1979) 373.

[32] F. Kapusta, Z. Phys. C 42, (1989) 225.

[33] T. Sjöstrand, JETSET7.3 Manual, CERN-TH 6488/92.

[34] S. Jadach et al., in Z Physics at LEP, CERN 89-08 Vol 1, eds. G. Altarelli et al. (1989).

[35] J. Hilgart, R. Kleiss, and F. Le Diberder, CERN-PPE/92-115 (1992).

[36] G. Alexander et al., The OPAL Collaboration, Z. Phys. C52 (1991) 175-207.

[37] P. Acton et al., The OPAL Collaboration, Z. Phys. C58 (1993) 219-237.

[38] V. Blobel, in Proceedings of the CERN School of Computing, Aiguablanca, Spain, September 1984, CERN 85-09, ed. C. Verkerk, (1985).

Charged Track Quality	Closest approach in $(x,y) < 2.5$ cm from beam Closest approach in $z < 10$ cm from interaction point At least 20 hits in Jet chamber Radius of first hit < 75 cm $\lvert\cos\vartheta\rvert < 0.97$ $p_T > 0.1$GeV
Electromagnetic Cluster Quality	$E_{raw} > 0.17$ GeV Cluster is not associated with a track (association half-angle $\eta = 0.1$ rad)
Track Multiplicity	≥ 3 charged tracks *of which* ≥ 1 with $p_T > 1$ GeV *and* ≥ 1 other with $p_T > 0.5$ GeV
Tag	$E_{tag} > 0.775 \times E_{beam}$ $47 < \vartheta_{tag} < 120$ mrad
Antitag	No electromagnetic cluster with energy $E_{clus} > 0.25 \times E_{beam}$ in hemisphere opposite tag
p_T balance	$\lvert {p_T}^{vis}_{in} + {p_T}^{tag} \rvert < 6$ GeV (in tag plane) $\lvert {p_T}^{vis}_{out} \rvert < 4$ GeV (out of tag plane)
Hadronic mass	2.5 GeV $< W_{vis} <$ 40 GeV

Table 1: Event selection requirements

Generator	QCD	VMD	$c\bar{c}$	$\tau^+\tau^-$
Normalized number of events	808	325	178	64

Table 2: Monte Carlo events by Category. The QCD events were simulated with $p_t^0 = 0.27$ GeV.

x bin	Background $4 < Q^2 < 8$ GeV^2	Background $8 < Q^2 < 30$ GeV^2
0.0-0.1	2.0 ± 2.0	5.9 ± 3.4
0.1-0.2	–	2.0 ± 2.0
0.2-0.3	–	2.0 ± 2.0

Table 3: Monte Carlo estimate of multihadronic background.

Q^2range (GeV^2)	x range	p_t^0 (GeV)	χ^2/DOF
$4 - 8$	$0.001 - 0.649$	0.44 ± 0.20	12.6/5
$8 - 30$	$0.006 - 0.836$	0.19 ± 0.12	6.2/7
$4 - 30$	$0.001 - 0.836$	0.27 ± 0.10	8.2/7

Table 4: Values of p_t^0 measured from the x_{vis} distribution.

x range	0.001-0.091	0.091-0.283	0.283-0.649
F_2^γ/α	0.224	0.352	0.348
Statistical error	0.018	0.030	0.090
Variation of cuts	0.018	0.018	0.080
Unfolding error	0.006	0.011	0.053
Overall syst. error	0.019	0.021	0.096
Total error	0.026	0.037	0.132

Table 5: Summary of unfolded $F_2^\gamma(x)$ measurement at $<Q^2> = 5.9$ GeV^2. The x bin limits are chosen by the unfolding package to minimize bin-to-bin correlations. The tabulated errors are not correlated between bins; there is an additional uncertainty of 5.9% on the overall normalization of $F_2^\gamma(x)$ arising from the charged multiplicity cut, the Monte Carlo normalization, and the ISR correction, and the luminosity measurement.

x range	0.006-0.137	0.137-0.324	0.324-0.522	0.522-0.836
F_2^γ/α	0.325	0.465	0.446	0.409
Statistical error	0.029	0.038	0.051	0.102
Variation of cuts	0.048	0.023	0.023	0.065
Unfolding error	0.005	0.009	0.016	0.029
Overall syst. error	0.048	0.025	0.028	0.071
Total error	0.056	0.045	0.058	0.124

Table 6: Summary of unfolded $F_2^\gamma(x)$ measurement at $<Q^2> = 14.7$ GeV^2. The x bin limits are chosen by the unfolding package to minimize bin-to-bin correlations. The tabulated errors are not correlated between bins; there is an additional uncertainty of 5.9% on the overall normalization of $F_2^\gamma(x)$ arising from the charged multiplicity cut, the Monte Carlo normalization, and the ISR correction, and the luminosity measurement.

Bibliography

[1] T. H. Baur *et al*, Rev. Mod. Phys. **50**, (1978) 261.

[2] G. A. Schuler and T. Sjöstrand, CERN-TH 6796/93.

[3] M. Drees and R. M. Godbole, Phys. Rev. Lett. **67**, (1991) 1189.

[4] K. Ahmet *et al*, OPAL collaboration, Nucl. Inst. Meth. **A305**, (1991) 275.

[5] H. Aihara *et al*, TPC/2γ collaboration, Z. Phys. **C34**, (1987) 1.

[6] H. Aihara *et al*, TPC/2γ collaboration, Phys. Rev. Lett. **58**, (1987) 97.

[7] Ch. Berger *et al*, PLUTO Collaboration, Phys. Lett. 142, (1984) 111.

[8] Ch. Berger *et al*, PLUTO collaboration, Nucl. Phys. **B281**, (1987) 365.

[9] M. Althoff *et al*, TASSO collaboration, Z. Phys. **C31**, (1986) 527.

[10] W. Bartel *et al*, JADE collaboration, Z. Phys. **C24**, (1984) 231.

[11] H.-J.Behrend *et al*, CELLO collaboration, Phys. Lett. **B126**, (1983) 391.

[12] T.Sasaki *et al*, AMY collaboration, Phys. Lett. **B252**, (1990) 491.

[13] R. Akres *et al*, OPAL Collaboration, CERN-PPE 156/93.

[14] H. Kolanoski: Two Photon Physics at e^+e^-Storage Rings, Berlin: Springer Verlag 1984.

[15] E. Witten, Nucl. Phys. **B120**, (1977) 189.

[16] Ch. Berger and W. Wagner, Phys. Rep. **146**, (1987) 1.

[17] R. J. DeWitt *et al*, Phys. Rev. **D19**, (1979) 2046.

[18] W. A. Bardeen and A. J. Buras, Phys. Rev. **D20**, (1979) 166.

[19] D. W. Duke and J. F. Owens, Phys. Rev. **D22**, (1980) 2280.

[20] J. H. Field, F. Kapusta and L. Poggioli, Phys. Lett. **B181**, (1986) 362.

[21] W. R. Frazer, Phys. Lett. **B194**, (1987) 287.

[22] J. Field, P349; Proceedings of VIII International Workshop on Photon-Photon Collisions, Shoresh, Jerusalem Hills 1988.

[23] J. Badier *et al*, NA3 collaboration, Z Phys C **18**, (1983) 281.

[24] R. Akres *et al*, OPAL Collaboration, CERN-PPE/93-145.

[25] H.-J.Behrend *et al*, CELLO collaboration, Phys. Lett. **B126**, (1983) 384.

[26] "The OPAL Trigger System"; OPAL Collaboration, to be submitted to Nucl. Instr. and Meth..

[27] S. Weisz et al, “ROPE Users' Guide”,OPAL internal publication.

[28] V. M. Budnev *et al*, Phys. Rep. **C15**, (1975) 185.

[29] C. B. Newman, Phys. Rev. Lett, **42**, (1979) 951.

[30] J. Badier *et al*, Z. Phys. **C18**, (1983) 281.

[31] D. W. Duke, P251; Proceedings of V Internation Workshop on Photon-Photon Collisions, Aachen 1983.

[32] G. Altarelli and G. parisi, Nucl. Phys. **B126** (1977) 298.

[33] F. Kapusta, Z. Phys. **C42**, (1989) 225.

[34] D. Griffiths: Introduction to Elementary Particles, Wiley 1987.

[35] G. Hanson et al, "OPAL User's guide for the SHIFT project",OPAL internal publication.

[36] A. Buijs, "Management of Analysis on Workstations",OPAL internal publication.

[37] A. M. Lee (iv), "Anatomy of a Mawsel",OPAL internal publication.

[38] T. Sjöstrand, JETSET7.3 Manual, CERN-TH 6488/92

[39] P. Acton *et al*, OPAL Collaboration, Z. Phys. **C58**, (1993) 219.

[40] S. Jadach *et al*, in Z Physics at LEP, CERN 89-08 Vol 1, eds G. Altarelli *et al* (1989).

[41] J. Hilgart, R. Kleiss, & F Le Diberder, CERN-PPE/92-115 (1992).

[42] B. W. Kennedy, "Radiative backgrounds to the tagged two photon process $e^+e^- \to e^+e^-$ + hadrons",OPAL internal publication.

[43] J. Allison *et al*, Nucl. Inst. Meth. **A317**, (1992) 47.

[44] G. Alexander *et al*, OPAL Collaboration, Z. Phys. **C52**, (1991) 175.

[45] R. Battacharya, G. Grammer Jr., J. Smith, and J.A.M. Vermaseren, Phys. Rev. **D15**, (1977) 3267.

[46] R. Battacharya, G. Grammer Jr., J. Smith, and J.A.M. Vermaseren, Phys. Rev. **D15**, (1977) 3280.

[47] R. Battacharya, G. Grammer Jr., J. Smith, and J.A.M. Vermaseren, Phys. Rev. **D19**, (1979) 137.

[48] "TWOGEN, a Monte Carlo generator for Two-Photon Reactions", to be published.

[49] T. Sjöstrand, Comp Phys Comm **47**, (1987) 347.

[50] T. Sjöstrand and M. Bengtsson, Comp Phys Comm **43**, (1987) 357.

[51] W.G.J.Langeveld, "Pion and Kaon pair-production in photon-photon collisions." PhD. thesis, University of Utrecht (1985).

[52] J.H. da Luz Viera and J.K. Storrow, Phys. Lett. **B205**, (1988) 367.

[53] J.H. da Luz Viera and J.K. Storrow, Phys. Lett. **B219**, (1989) 529.

[54] J.H. da Luz Viera and J.K. Storrow, Z. Phys. **C51** (1991) 241.

[55] J. H. Field, F. Kapusta and L. Poggioli, Z. Phys. **C36**, (1987) 121.

[56] C.J. Hill and G.G. Ross, Nucl. Phys. **B148**, (1979) 373.

[57] V. Blobel, in Proceedings of the CERN School of Computing, Aiguablanca, Spain, September 1984, CERN 85-09, ed C. Verkerk, (1985).

[58] Venus preliminary data shown at Cornell Lepton Photon Symposium, August 1993.

[59] D. J. Miller, talk at the Cornell Lepton Photon Symposium, August 1993.

[60] H. Abramowicz, K. Charchula and A. Levy, Phys. Lett. **B269**, (1991) 458.

[61] M. Glück, E. Reya and A. Vogt, Phys. Rev. **D46**, (1992) 1973.

[62] European Committee for Future Accelerators. 'General Meeting on LEP', CERN Publications group, 1981.